Alma Mater Studiorum · Università di Bologna

SCUOLA DI SCIENZE

Dipartimento di Fisica e Astronomia

Corso di Laurea Magistrale in Astrofisica e Cosmologia

Constraints on the duty cycle of the remnant radio galaxy NGC 6086 in the galaxy group Abell 2162

Candidato:
Simone Candini

Relatore:
Prof.ssa Annalisa Bonafede

Correlatore:
Dott.ssa Marisa Brienza

Appello IV

Anno Accademico 2021/2022

"Diconsi stelle di XVI grandezza e tanto più
lontane sono che la luce loro solo dopo
XXIV secoli arriva a noi: visibili
furono esse coi telescopi di Haerschel.
Ma chi narrerà delle stelle anche più remote,
atomi percettibili solo colle più meravigliose
lenti che la scienza possegga o trovi?
Quale cifra rappresenterà tal distanza che
solo correndo per milioni di
anni la luce alata valicherebbe?
Uomini udite: oltre quelle spaziano
ancora i confini dell' Universo!"

Contents

Abstract

Galaxy clusters and groups are the most massive bounded structures and the knots of the large-scale structure of the Universe. These structures reside in dark matter haloes, hosting tens to hundreds of galaxies and they are filled with hot and rarefied gas.
Radio Galaxies are a peculiar class of galaxies with a luminosity in the radio band up to 10^{46} erg/s between 10 MHz and 100 GHz. These galaxies are a subclass of Active Galactic Nuclei (AGN) in which there is accretion on the Super Massive Black Hole (SMBH). The accretion generates jets of relativistic particles and magnetic fields which lose energy through synchrotron radiation, best observable at radio frequencies. The shape of the spectrum of the synchrotron emission is a power law with a negative slope, typical values are $\sim$0.5-0.8 (in absolute value) and it becomes steeper over time due to energy losses of high-energy particles. The study of the spectral ageing of the AGN plasma is fundamental to understand its evolution, interaction with the environment and to constrain the AGN duty cycle.
Some AGN located in clusters and groups show a pair of radio lobes and radio jets. These jets are not constantly active throughout the entire life of the host galaxy. When the jets are inactive, the radio galaxy starts a quiescent (or inactive) phase in which the plasma evolves without the injection of new particles by the AGN. The radio galaxies observed during an inactive phase are labelled as remnant galaxies. During the quiescent period, the lobe's particle populations and magnetic field still radiate energy through synchrotron emission in the radio band. While the synchrotron spectrum ages, the synchrotron break moves to lower and lower frequencies over time. Remnant radio galaxies could also restart their activity if there is a new inflow of gas in the central SMBH and the jets switch on again. These objects are called restarted radio galaxies and they present an active core and jets.
The duty cycle of an astrophysical source is generally defined as the fraction of time during which the source is active. The cycle is characterised by active and quiescent phases that are thought to occur one after the other with variable timescales. The knowledge of the duty cycle is important for both galaxies and environment evolution because the AGN energy released in the environment during the active phases helps us to investigate AGN feedback, which is essential to study how SMBH impact the galaxies' growth and the thermal evolution of the intra-cluster and intra-group medium.

Because of the radio spectral shape, radio galaxies are brightest at low frequencies, but the previous generation of instruments were not able to perform low-frequency and high-sensitivity observations. Only with the advent of new radio interferometers, such as the low frequency array (LOFAR) and the upgraded giant metrewave radio telescope (uGMRT), the analysis of high-resolution and high-sensitivity MHz observations can

be done, giving access to the oldest detectable electron populations emission to date.

Thanks to these observations, new large-scale diffuse emission analysis can be made, aiming to give new constraints on the duty cycle of the source and to understand the interaction between the old AGN plasma and the surrounding environment. Moreover, recent observations have detected filamentary shape emission of old plasma as the result of re-acceleration or an increase of the magnetic field strength in those regions (i.e. Brienza et al. [2021], Brienza et al. [2022]). The origin of the filaments is still subject of debate and further studies are needed.

In this thesis, we have investigated the duty cycle of the nearby remnant radio galaxy NGC 6086, located in the centre of the galaxy group Abell 2162. This source has already been investigated in the past (i.e. Giacintucci et al. [2007], Murgia et al. [2011]), but we have made major steps forward thanks to the new high-sensitivity interferometers in the low-frequency radio band. We used a LOFAR image at 144 MHz, uGMRT images at 400 MHz and 675 MHz, a 1400 MHz VLA (B + C configuration) image and a 5000 MHz VLA (D configuration) image. This wide range of frequencies allows us to perform resolved spectral ageing analysis. We have detected for the first time three filaments of emission and a second couple of lobes. We have performed an integrated and resolved analysis on the previously known inner lobes, the new filaments and the older outer lobes. We have performed an age estimate of the two pairs of lobes to give constraints on the duty cycle of the source and an estimate of its active time.

This thesis is organised as follows:

- Chapter 1: we present an overview of the main properties of galaxy clusters, galaxy groups and active galactic nuclei with a focus on non-thermal emission and radio classification. We present NGC 6086, the system studied in this thesis work;

- Chapter 2: we present the fundamental concepts of radio observations for a single antenna or an interferometric array and introduce the interferometric arrays used in this thesis;

- Chapter 3: we show the main calibration steps for VLA data and we exhibit how they are applied to two archival datasets that observed NGC 6086;

- Chapter 4: we introduce the new observation images of NGC 6086 at low frequency made with the LOFAR and uGMRT interferometers, which complement the VLA dataset. We show an integrated and resolved analysis of the inner lobes and the analysis of the newly discovered diffuse emission at high and low resolution;

- Chapter 5: we present the spectral age analysis of the source performed with the software `BRATS`. This analysis allows us to give a first-order age estimate of the inner and outer lobes, giving constraints on the duty cycle of the AGN activity in the source;

- Chapter 6: we discuss the results of this thesis work and conclusions. Moreover, we highlight some considerations and future prospects.

Chapter 1

Galaxy clusters and Active Galactic Nuclei

1.1 Galaxy clusters and galaxy groups

The large-scale structure (LSS) of the Universe is driven by the gravitational collapse of dark matter haloes and the subsequent merging of these into progressively larger structures (Sabater et al. [2019]). Galaxies form inside dark matter haloes by radiative cooling of baryons (White and Rees [1978]) and then evolve within them. The vast majority of galaxies are not isolated and in their own halo, instead, they are mostly found in larger bound systems along with dozens, or even hundreds, of other galaxies. The less massive structures ($M < 10^{14}$ $M_\odot$) are called galaxy groups and the massive ones are called galaxy clusters, all of them are linked together in 'filaments', building the so-called cosmic web (see Fig. 1.1).

Galaxy clusters are the most massive gravitationally bound structures in the Universe, their masses reach values up to 10^{15} $M_\odot$ and their viral radii reach the megaparsec (Mpc) scale. Galaxy clusters typically contain up to ~ 1000 (mostly elliptical) galaxies, which, however, constitute only a small fraction of the total system mass, equal to $\sim 1 - 5\%$. The other baryonic component is the intra-cluster medium (ICM), the hot ($\sim 10^7 - 10^8$ K) and rarefied ($\sim 10^{-3}$ cm^{-3}) plasma, which permeates the entire structure and contributes to $\sim 15 - 20\%$ to the total mass value. All the remaining mass is the contribution of the dark matter component (Eckert et al. [2022]).
Galaxy groups have an intermediate scale between individual galactic halos and clusters, with masses between 10^{13} $M_\odot$ and 10^{14} $M_\odot$. They consist of a few tens of galaxies (mainly late-type galaxies) and the intra-group medium (IGrM), both bound in a common gravitational potential, and also in this case, the main contribution to the total mass is given by the enclosing dark matter halo.
Galaxy groups are gaining more and more interest in the scientific community as they are crucial laboratories where to test a wide range of astrophysics: from how galaxies form and evolve to the LSS statistics for cosmology (Oppenheimer et al. [2021]). Being less massive and subject to much less energetic interactions than clusters, minor attention has been received by groups. However, they play a crucial role in cosmic structure formation as they represent the most abundant systems in the Universe and the build-

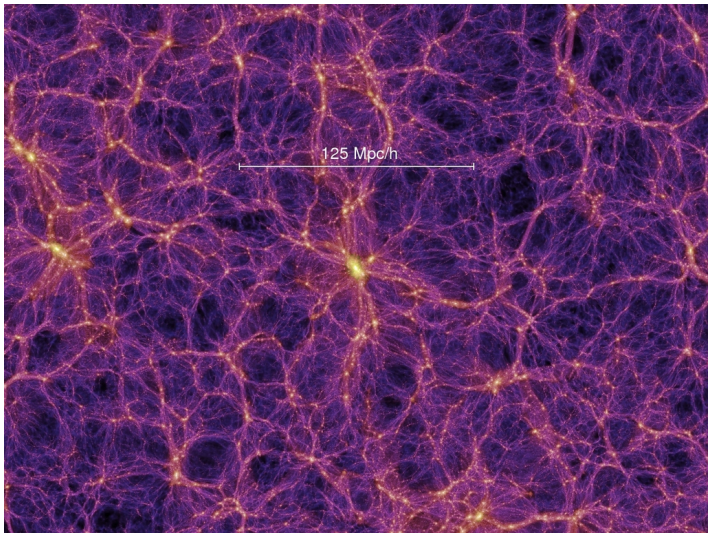

Figure 1.1: Snapshot of the VIRGO Millennium Run simulation. More than ten billion particles are used to trace the evolution of the matter distribution in a cube of two billion light-years side to represent the most accurate cosmic web structure of the Universe. Colours represent the dark matter distribution in which the yellow knots are the higher mass systems, such as clusters and groups. Credit: wwwmpa.mpa-garching.mpg.de, Springel et al. [2005]

ing blocks of massive clusters. This paucity of attention is partly due to challenges associated with their observational detection because, unlike clusters, they have faint X-ray emission, a lower number of optically detectable galaxies, lower gas that leads to lower Sunyaev-Zel'dovich effect and low total mass that implies inefficient gravitational lensing detection. Luckily, the new generation of telescopes in the X-ray, optical and radio bands will pave the way to the galaxy groups surveys and further discoveries will be accomplished, giving them a central role in the study of the structure formation and evolution of the Universe, in measuring the cosmic baryonic content and investigate on the value of the magnetic fields. An example of the application of groups is presented by Mernier et al. [2022], they show how galaxy groups (such as MRC 0166+111, Fig. 1.3) can be used to investigate the magnetic field value in the most direct and least model-dependent way thanks to the high-energy emission.

Other main components of both galaxy groups and clusters are the active galactic nuclei (AGN): supermassive black holes (SMBH) that accrete material from the surrounding environment. If we take a look at their contribution to the system's evolution we can recognise their crucial implication in energy terms. Indeed, the AGN is able to heat, relocate and even remove the surrounding gas from the host galaxy (Fabian [2012], McNamara and Nulsen [2012]). The highest impact of the AGN activity are called feedback processes and they have more influence in the galaxy groups' environment due to the lower masses and shallower gravitational potentials.

Feedback can be associated with the energy radiation coming from the accretion process on the black hole or the powerful jets (and winds or outflow) produced by the

Figure 1.2: Left panel: The picture shows the optical view of Abell 2218, an example of a rich galaxy cluster composed of thousands of individual galaxies at redshift $z = 0.17$. Credit: esahubble.org, NASA, ESA, and Johan Richard (Caltech, USA); right panel: Abell 2744 cluster hosting diffuse radio emission shown in red and the X-ray emission is shown in blue. Credits: van Weeren et al. [2019].

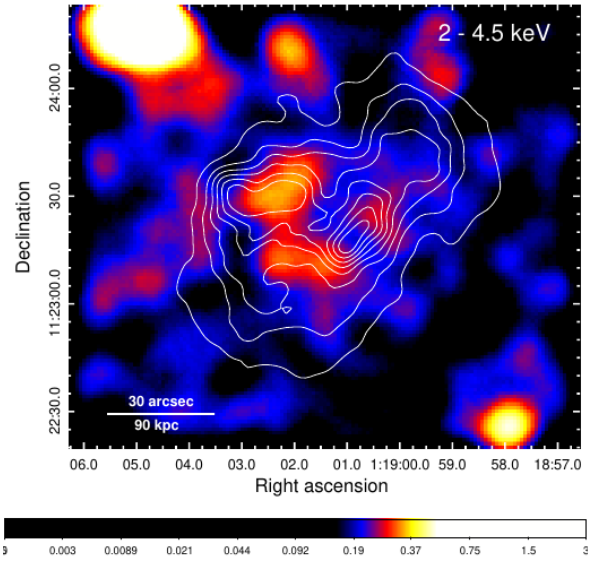

Figure 1.3: The image shows the MRC 0166+111 galaxy group, used to measure the magnetic field of the system. The colour scale shows the XMM-Newton EPIC observation in the hard-X band with overlaid the radio contours of the source at 621 MHz with the GMRT telescope.

inner and most energetic part of the AGN. They have a strong impact on the interstellar medium of the host radio galaxy, i.e. star formation is influenced by the feedback interaction with the surrounding hot IGrM. The AGN release a large amount of energy through feedback in the medium, preventing the gas from cooling and changing the thermal gas evolution of the system. Moreover, these events could be powerful enough

to remove the gas not only from the galaxy but also from the group itself with an impact on larger volumes than in a cluster environment. Groups could experience a baryon depletion if the group binding energy is lower than the AGN energy release. For these reasons, it is crucial to study their activity in the group structures.
This kind of knowledge will help galaxy evolutionary models to include better AGN feedback and feeding conditions, with the aim to reproduce the shape of the galaxy luminosity function and the halo baryon fraction.

Clusters and groups are detectable in a wide range of frequencies. The stars are detectable in the optical, infrared and ultraviolet bands. The radio band is used to detect stars during their formation process. The gas is detectable through atomic hydrogen (HI) and carbon monoxide (CO) lines in the radio band. This emission is produced by the stellar populations and gas clouds that are evolving inside galaxies.
The X-Ray band is dominated by the ICM (or IGrM) emission through bremsstrahlung. The hot plasma loses its energy through the bremsstrahlung emission mechanism, with an exponential cut-off in the X-ray band. The Bremsstrahlung emissivity is:

$$J_{br}(\nu, T) = 6.8 \cdot 10^{-38} T^{-1/2} n_e n_p Z^2 g_f e^{-h\nu/kT} \qquad \left[\frac{\text{erg}}{\text{s cm}^3 \text{ Hz}}\right] \tag{1.1}$$

and the spectral cut-off can be seen in Fig. 1.4, which shows the shape of spectral emissivity.

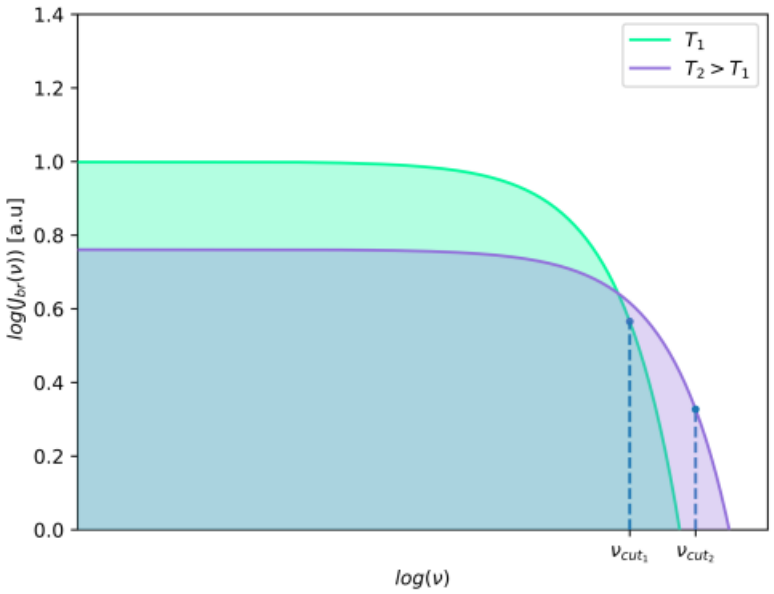

Figure 1.4: Bremsstrahlung radiation specific emissivity for two different temperatures showing the cut-off frequency shifting to higher frequencies (Baldini [2020]).

In the galaxy cluster environments, the radio band could be characterised by diffuse synchrotron emission on different scales: the biggest structures are called giant halos and are detectable on cluster scale (up to few Mpc distances); mini halos have similar characteristics to the giant, but a smaller scale (100-500 kpc) and they are located in

relaxed systems; the last structures are the radio relics which are on Mpc scale and in merger structures as the giant halos, but they have an elongated structure. These sources are generated by merger events, shocks or by dynamical instabilities, influenced by turbulence and their spectrum is characterised by a steep synchrotron radio emission. Compact source radio emissions come from AGN jets, which accelerate electron populations up to the Mpc scales, for most energetic events, leading to the formation of radio lobes and hotspots.
Even if the galaxies in clusters represent the minor baryonic component, galaxy mergers can happen, especially during the system formation and in the central region where the potential well is higher. This process can lead to the formation of supermassive ($M = 10^{11}$ $M_\odot$) elliptical galaxies, which can be up to a few magnitudes brighter than the other. These are called brightest cluster galaxies (BCG, Lin and Mohr [2004], Chu et al. [2021]) or brightest group galaxies (BGG). BCG and BGG are, by definition, the highest luminosity and massive galaxies that can be found in the Universe. They are usually elliptical galaxies that lie close to the centre of the potential well of the system, the high luminosity makes them more easily recognisable and they can be extremely useful to trace how galaxy clusters have formed and evolved. BCG are usually detected nearby to the clusters' X-ray emission peaks, with velocities similar to the rest frame of clusters. These peculiar characteristics could be probes of a different formation history, models suggest that one possibility could be the involvement of galaxy merging within the cluster during the structure collapse.
From an observational point of view, BCG are more likely to have higher emissions in the radio band than other galaxies with the same mass, which means brighter AGN (Best et al. [2006], Dunn et al. [2010]); a large number of them also shows a high level of molecular hydrogen and also recent star formation detectable as a blue optical excess.

1.2 Active Galactic Nuclei

Active galactic nuclei (AGN) are a class of galaxies that host a supermassive black hole (SMBH) in the nuclear region, which is accreting material from the surroundings. This in-fall of gas inside the SMBH releases an enormous amount of energy, which manifests as an excess of emission across the entire electromagnetic spectrum with respect to the standard emission of stars, gas and dust in a galaxy.

The AGN taxonomy is vast and based on observations at different wavelengths. It is hard to discriminate between different typologies and a high number of classification criteria have been proposed. Observation choices make the taxonomy even more complicated because using different wavelengths or different resolutions changes what can be observed in the same source and from the same central engine. The radio frequencies allow us to detect the synchrotron emission coming from the jets; in the optical and x-ray band, we can investigate the accretion disc; we can characterise the shape and properties of the dusty torus with infrared frequencies.
Some examples of classification are: radio-loud (RL) and radio-quiet (RQ) AGN; RQ AGN are also divided in Seyfert 1 or Seyfert 2 depending on the observer line of sight; obscured and unobscured AGN; low power or high power AGN. Unified models have

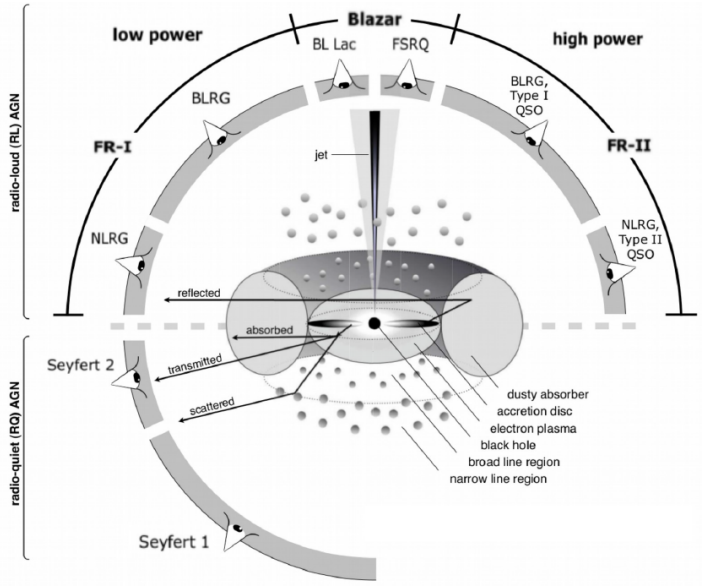

Figure 1.5: Sketch image that shows the AGN components and a partial taxonomy on a line of sight and power basis. Credit: Beckmann and Shrader [2012].

also been proposed, which assume that all AGN types are the same physical object, i.e. seen with a different orientation by the observer.
In this thesis is analysed the AGN radio emission from jets, for this reason, the focus is put on this emission band.

1.2.1 Jetted AGN

Although AGN were originally discovered through their radio emission, radio-loud objects are the exception rather than the rule. Only a small fraction ($\sim 10 - 20\%$) of the AGN population has strong radio power emission (Visnovsky et al. [1992]). Moreover, the RQ and RL AGN dichotomy is thought to be intrinsically related to the radio jet production and/or stage of activity (Lopez-Rodriguez et al. [2022]).
A sharp division between RL and RQ AGN is hard to set, the former are usually $\sim 10^3$ times powerful in the radio band and we take 10^{23} W/Hz as an upper limit for the RQ AGN. Radio loudness can be measured as follows (Kellermann et al. [1989]):

$$R = \frac{F_{5GHz}}{F_{optical(B)}} > 10 \tag{1.2}$$

where R > 10 implies that an RL AGN has been found, but since the optical flux could be originated by different processes, this is not a strong definition.

AGN radio emission can be attributed to:

- non-thermal processes: RL AGN are characterised by strong emission generated by powerful relativistic jets or outflows that emit by synchrotron radiation and inverse Compton scattering;
- thermal processes: RQ AGN are dominated by thermal host galaxy processes, i.e. star formation, AGN processes such as accretion disc wind, coronal disc emission, collimated winds or a combination of them.

As recently suggested, these two kinds of active nuclei can be labelled as *jetted* and *non-jetted* (Padovani [2016]), in order to overtake the luminosity as the division criteria and introduce a new one based on the physic of the source.

Radio jets emit radiation through two main non-thermal processes: synchrotron radiation made by the relativistic electron populations spinning around the magnetic field and inverse Compton scattering made by the same population interacting with the cosmic microwave background (CMB) radiation.
Jetted AGN are typically found in massive galaxies, usually, elliptical galaxies and the main characteristic of this kind of nuclei is the presence of twin jets (not always both visible) that drag off relativistic plasma and magnetic field.
During their forward motion, the lobes of radio plasma inject energy and momentum to the surrounding medium. There are multiple observations which show that AGN are able to deposit the jet energy directly and efficiently into the ICM/IGrM by inflating bubbles or cavities (see reviews by McNamara and Nulsen [2007] and Fabian [2012]).

These lobes and jets are detected on galaxy scales, but they can also expand up to a few Mpc (giant sources). They are usually double and symmetrical and their shape, which is influenced by the jet power and the galaxy environment (i.e. denser galaxy environments increase the probability of jet detection), is used as a classification criterion. Low-frequency studies made by Sabater et al. [2019] have shown that the fraction of galaxies hosting radio AGN rises strongly with stellar mass content and shows little dependence on black hole mass (at a fixed stellar mass), they also found that 100 per cent of the galaxies used for their study (found with Lofar two-metre sky survey, LoTSS and Sloan Digital Sky Survey, SDSS, combined) with masses higher than 10^{11} $M_{\odot}$ display radio AGN activity. This result suggests that the most massive galaxies are always switched on at some level, even with low radio power. In addition, the RL AGN fraction decreases proportionally to the host mass and denser environments are more likely characterised by jets.

According to the AGN unified model (see Fig. 1.5), which was born with observations made by Antonucci and Miller [1985], jetted AGN can be divided into different groups on an observational basis. If the source is seen 'face on', with an active jet pointing toward us (or with an inclination angle smaller than ~ 5 degrees) it is called *blazar*; if the source is seen 'edge on', with jets pointing perpendicularly with respect to our line of sight, they could be a *radio galaxy* (if the viewing angle is higher than 45 degrees) or *radio quasar* (if the viewing angle is lower than 45 degrees).
Radio galaxies are a peculiar class of AGN with a luminosity in the radio band up to 10^{46} erg/s between 10 megahertz (MHz) and 100 gigahertz (GHz).
Despite a variety of morphologies, radio galaxies are historically divided into two main classes called Fanaroff-Riley I (FR I) and Fanaroff-Riley II (FR II), named after the authors who first made the classification (Fanaroff and Riley [1974]). The main morphological characteristics of these two classes of sources are shown in Fig. 1.6.
FR I type sources have less powerful jets, which slow down near the host galaxy and propagate away at a lower speed, forming the so-called edge-darkened lobes. Jets are brighter and wider than in the FR II galaxies. As defined by Leahy et al. [1996], two subclasses of FR I are the *plumed* sources (or *tailed*) and the *lobed* sources (or *bridged*),

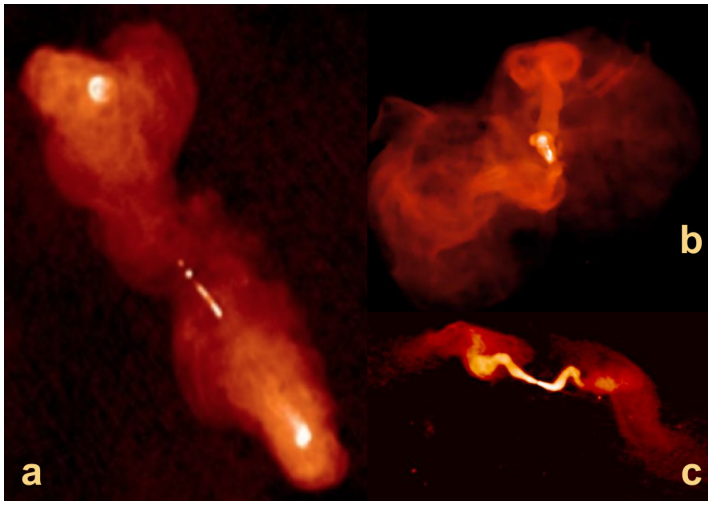

Figure 1.6: Radio maps of three radio galaxies showing the classical Fanaroff-Riley morphological classes: (a) 3C193, FR II; (b) 3C274, lobed FR I; (c) 3C31, plumed FR I. Observations were performed with the Very Large Array at 1.4 GHz and images have 5.5" resolution. Image courtesy of NRAO/AUI.

according to their lobes morphology.
FR II type sources have high relativistic speed jets, forming the so-called hotspots, which are the region where the jets impact onto the external medium creating shocks. The lobes are labelled as edge-brightened because brighter near the hotspot and darker close to the host. Jets in FR II always have low luminosity and are well collimated, suggesting they act as efficient channels of particle flow up to the lobe edges. In some cases, the doppler boosting effect could generate asymmetries between jets.
This canonical morphology division is correlated with the source luminosity, $L_{150MHz} \sim 10^{26}$ W Hz^{-1} is the power upper limit for FR I and the lower limit for FR II (Fanaroff and Riley [1974], Ledlow and Owen [1996]). Another value used as a division line was proposed by Fanaroff and Riley [1974]:

$$L_{178\ \mathrm{MHz}} = 10^{25}\ \mathrm{W/Hz/sterad} \tag{1.3}$$

Recent studies with more sensitive observations and larger samples have shown the lack of a clear dividing line between the two classes, moreover, there is a high quantity of FR II under the division value. The reasons behind the generation of a specific morphology are still not fully known (see Mingo et al. [2019]).

On one hand, the influence of the environment on jet propagation has to be taken into account, the higher the density at which jets propagate and the faster the jets slow down. Under this assumption, FR I are supposed to be in a denser environment. On the other hand, this is not the only variable because physical mechanisms responsible for jet production could play a fundamental role. These mechanisms are still largely unknown, i.e. accretion rate, accretion mode and black–hole spin(e.g. Baum et al. [1995]; Meier [2001]; Garofalo et al. [2010]).

1.3 Cooling flow

Observations have shown that relaxed clusters have, in their core regions, a cusp in the density profile and the X-ray surface brightness profile, meaning that the ICM is flowing to the central regions. Clusters with this feature are labelled as cool core clusters, this name derives from the main process involved in this kind of central region, called cooling flow.
To fully understand the cooling flow, it is necessary to introduce the cooling time: $t_{cool} = \epsilon/\dot{\epsilon}$ (where ϵ is the total energy and $\dot{\epsilon}$ is the energy loss rate), which is defined as the time needed to release all the gas energy through radiative losses. Since $t_{cool} \propto T^{1/2} n^{-1}$ (where T is the temperature and n is the number density) when the bremsstrahlung is the main emission mechanism, time is shorter in the denser regions (it can be shown that the increase in density prevails over the decrease in temperatures).
External regions are characterised by higher cooling time than the age of the cluster, implying that cooling is inefficient when we are far from the centre. On the other hand, inside the central ∼100 kpc region, cooling time is much lower than the cluster's age and radiative losses become efficient.
Cooling radius, r_{cool}, is defined as the radius in which $t_{cool} = t_{age}$ and it is the efficient cooling largest radius. Within r_{cool}, cooling reduces the gas temperature and the gas density must rise to maintain the pressure at r_{cool}. The only way for the gas density to rise is by flowing inward. This leads to the creation of the cooling flow.
During a 'cooling time' period, that lasts $t_{cool} \sim 10^7 - 10^8$ yrs, hot gas cools down in a kpc scale central region and the consequence is the generation of a multiphase medium, with a temperature that goes from T$\sim 10^7$ K at the edge to T$\sim 10^4$ K or less inside, eventually leading to star formation and SMBH cold gas accretion.

This process has been studied for a long time, but is still a hot topic because it is always matched with unsolved problems, called *cooling flow problems*: the old cooling flow problem was introduced because observations shown a lack of cooled material that should be seen, according to theoretical models, as a consequence of past cooling flow events; the new cooling flow problem was introduced when it was possible to do resolved spectral analysis because observations did not show the expected amount of line emission from the multi-phase gas that is cooling at the time of observation in the central cooling region.
Summarising, observations and models disagree on the amount of cold gas that should be present from past events and also on the amount of gas that should cool due to processes that are happening now. The observational paucity of cooled gas and instantaneous cooling led to the necessity to introduce heating mechanisms complementary to the flow, which have to release a specific amount of energy to balance the cooling flow and match observational features.
The searched mechanism should have some specific characteristic to contrast cooling: it has to release higher energy in the central regions, but without disrupting the core structures; $E_{heating} \sim E_{cooling}$; suppress the mean cooling rate by $10^1 - 10^2$ $M_\odot$/yr ; it has to be somehow continuous over the time because cooling is always suppressed.
Several mechanisms have been proposed and analysed through the years, such as su-

pernovae energy release, turbulence, heating conduction, radiative heating and lastly, AGN activity, which is related to the creation of cavities and weak shock waves. Which one is the real responsible for the cooling suppression is still under debate, but it is likely a combination of two or more of them.
Central positions, high amount of released energy and connections with other heating mechanisms make the central AGN the best candidate to suppress the cooling, but it is also a fundamental tool to investigate the interactions between SMBH and galaxies or clusters' evolution.

1.4 Synchrotron radiation

The main emission in radio galaxies is produced by relativistic electrons that spiral around the magnetic field lines and emit energy during the circular motion around them with constant linear and angular speeds.
The energy emission for a single particle is derived starting from the Larmor formula, which represents the emitted power for accelerated charged particles:

$$\frac{dE}{dt} = \frac{2}{3}\frac{q^2\vec{a}^2}{c^3} \tag{1.4}$$

where q is the charge of the particle, a is the acceleration and c is the speed of light. The acceleration is derived from the Lorentz force and the second law of dynamics:

$$\frac{\vec{p}}{dt} = m \cdot \vec{a} = \frac{q}{c}\ \vec{v} \times \vec{B} = q\beta\vec{B}\sin\theta \tag{1.5}$$

where $\vec{p}$ is the momentum, $\vec{B}$ is the magnetic field and θ is the *pitch* angle between the speed and magnetic field vectors.
By replacing $\vec{a}$ in the 1.4 equation, we obtain:

$$\frac{dE}{dt} = \frac{2}{3}\frac{q^4}{m^2c^3}\ \beta^2\vec{B}^2\sin\theta^2 \tag{1.6}$$

Since the electrons producing the synchrotron radiation move at relativistic speed, a γ^2 factor has to be added to the previous equation. The average synchrotron power per relativistic electron in a source with an isotropic pitch angle distribution is:

$$\frac{dE}{dt} = \frac{4}{3}\ c\sigma_T\gamma^2\beta^2 U_B \tag{1.7}$$

where σ_T is the Thompson cross-section and $U_B = \frac{B^2}{8\pi}$ is the magnetic field energy density.
The relativistic emitting particles have an energy distribution that follows $N(E,t) = N_0E^{-\delta}$ (where δ is the particle energy power index). The energy distribution translates in the observed synchrotron power law distribution that follows $S \propto \nu^{-\alpha}$ (where S is the flux density, ν is the frequency and $\alpha = \frac{\delta-1}{2}$ is the particle spectral index, the typical values are between 0.5-0.8).
The spectral index is calculated as follows:

$$\alpha = -\frac{log(S_{\nu_1}/S_{\nu_2})}{log(\nu_1/\nu_2)} \tag{1.8}$$

The power law spectrum can be modified by several effects:

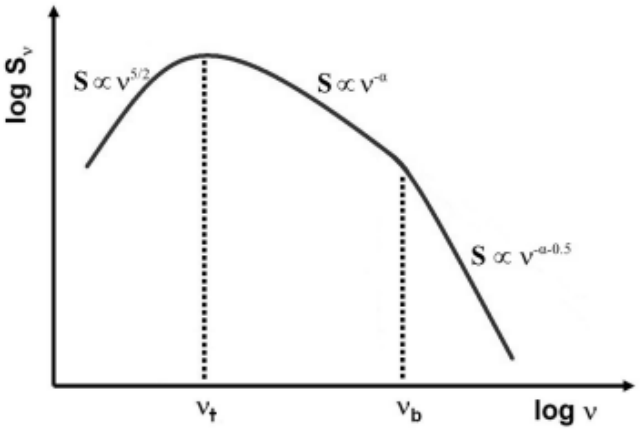

Figure 1.7: Schematic view of an ideal synchrotron spectrum which presents self-absorption in the left part, while in the higher frequencies shows a steepening after the break (Botteon [2013]).

- **synchrotron self-absorption (SSA)**: this absorption is made by the same electrons responsible for the synchrotron emission. This feature is visible in optically thick structures, in which photons are more likely to interact with the same relativistic particles that emitted them. The spectrum is absorbed at lower frequencies and the steepening is $S \propto \nu^{5/2}$ before the emission peak;

- **spectral break**: if we have a particle continuous injection, new high-energy populations are always introduced. As we have seen in Formula 1.7, the energy loss rate is proportional to the energy of the particles (γ^2) and the high-energy particles will lose energy faster than the others. For this reason, the typical feature of the new injection is a steepening of the spectrum with respect to the classical power law and it becomes $S_{>\nu_{break}} \propto \nu^{-\alpha-0.5}$ after the break frequency;

- **spectral cut-off**: this is the typical spectral feature of an aged and inactive plasma. It is caused by the lack of high-energy electrons and therefore a lack of emission above the break frequency. The steepening after this frequency increase over time and generates the so-called cut-off frequency. This frequency value decreases over time and we do not have emission at higher energies;

- **source expansion**: the expansion decreases the magnetic field strength and the electron density. The consequence is the shift of the spectrum to lower frequencies;

- **source compression**: at the opposite of the expansion, compression leads to an enhancement of the magnetic field strength and electron particles and, as a consequence, the spectrum shifts to higher frequencies because the emission increases.

The characteristic lifetime (t_{age}) of the emitting particle populations depends upon the competition between synchrotron radiative losses and the energy lost due to the

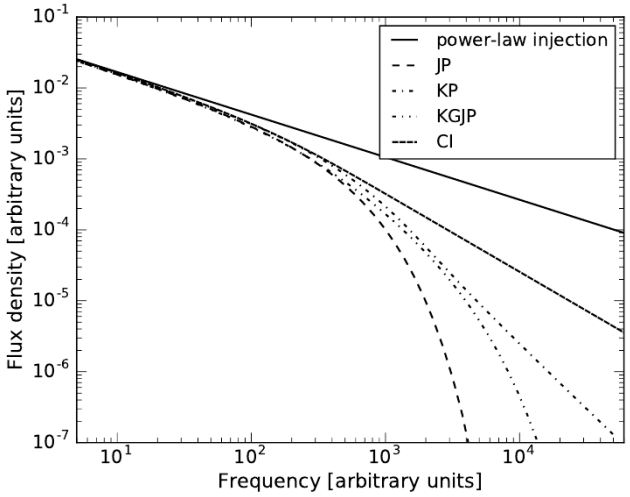

Figure 1.8: Spectra for different synchrotron ageing models (from van Weeren et al. [2019]). All models have $\alpha_{inj} = 0.6$. The solid line depicts the spectral shape before any energy losses, while non-solid lines show different models of spectral ageing

Inverse-Compton (IC) scattering between relativistic electrons and CMB photons as follows:

$$t_{age} \sim 3.2 \times 10^{10} \frac{B^{0.5}}{B^2 + B_{CMB}^2} [(1+z)\nu]^{-0.5} \text{ yr} \tag{1.9}$$

where B [μG] is the magnetic field strength of the source, B_{CMB} is the magnetic field intensity required to have a synchrotron emission equivalent to the IC scattering losses and his value is $B_{CMB} = 3.25\ (1+z)^2$ [μG], z is the redshift and ν [MHz] is the frequency. The formula highlights the inverse proportionality between lifetime and emission frequency.
Since the highest frequencies have the fastest energy losses, the initial power law spectrum steepens beyond a break frequency, whose position is related to the time since the last acceleration event. Different models are trying to represent spectral evolution, i.e. the JP (Jaffe-Perola) synchrotron model (Jaffe and Perola [1973]) or the CI (continuous injection). The former assumes a single injection or acceleration event and subsequent passive ageing, the latter assumes continuous injection of new high-energy particles, an example of power law spectral ageing is shown in Fig. 1.8 (van Weeren et al. [2019]).

Due to the spectral shift to lower and lower frequencies, the new generation of radio interferometers, which will be discussed later in this thesis (see Sec. 2.4), are giving fundamental observational support to the study of the spectral evolution of this class of AGN.

1.5 Magnetic field estimates from equipartition

In order to constraint the radiative age of the plasma, we need information on the magnetic filed strength. The total energy (U_t) of the plasma synchrotron emissivity is

given by both the electron population and the magnetic field, but we cannot disentangle these two contributions in order to give a solid measure to the magnetic field. The usual assumption is to estimate the magnetic field B by minimising the total energy content of the source, or in other words, we make some assumptions about how the energy is distributed between the fields and particles. We know that $U_t = U_e + U_p + U_B$ where U_e is the contribution of the electrons, U_p is the contribution of the positive charges and U_B is the contribution of the magnetic field.
The last term is known to be:

$$U_B = \frac{B^2}{8\pi}\ \phi V \tag{1.10}$$

where ϕ is the filling factor (fraction of the source volume occupied by the magnetic field) and V is the total volume.
The first term is calculated as follows:

$$U_e = V \cdot \int_{\epsilon_1}^{\epsilon_2} N(\epsilon)\, d\epsilon = V \cdot N_0 \int_{\epsilon_1}^{\epsilon_2} \epsilon^{-\delta+1}\, d\epsilon \tag{1.11}$$

which can be expressed as a function of the synchrotron luminosity L_{syn} since:

$$L_{syn} = V \cdot \int_{\epsilon_1}^{\epsilon_2} N(\epsilon) \left(-\frac{d\epsilon}{dt}\right) d\epsilon = V N_0 cost (B \sin\theta)^2 \int_{\epsilon_1}^{\epsilon_2} \epsilon^{-\delta+2}\, d\epsilon \tag{1.12}$$

after the substitution (see Govoni and Feretti [2004] for more details) the result is :

$$U_e = cost \cdot L_{syn} B^{-3/2} \tag{1.13}$$

Lastly, the energy contained in the positive charges (relativistic protons or positrons) is assumed to be proportional to the energy of the electrons since we do not know the abundance of these particles, so we write it as

$$U_p = k U_e \tag{1.14}$$

and now we have a new total energy expression which is a function of the magnetic field:

$$U_t = (1+k)\ cost\ L_{syn} B^{-2} + \frac{B^2}{8\pi}\phi V \tag{1.15}$$

where k and ϕ reflect our uncertainties about the physics of the system and they have to be assumed. Values usually assumed in literature are $\phi = 1$ and $k = 0$ or $k = 1$.

The main assumption made in this contest is that the total energy is represented by its minimum value (Fig. 1.9) and this is the case when the magnetic field and the relativistic particles give the same energy contribution:

$$U_B = \frac{3}{4}\ (1 + k\ ) U_e \tag{1.16}$$

and the total energy equipartition value is:

$$U_t(min) = \frac{7}{4}\ (1+k)\ U_e = \frac{7}{3} U_B \tag{1.17}$$

The magnetic field for which the total energy content is minimum therefore is:

$$B_{eq} = 6\pi(1+k)\ cost\ \frac{L_s}{\phi V} \tag{1.18}$$

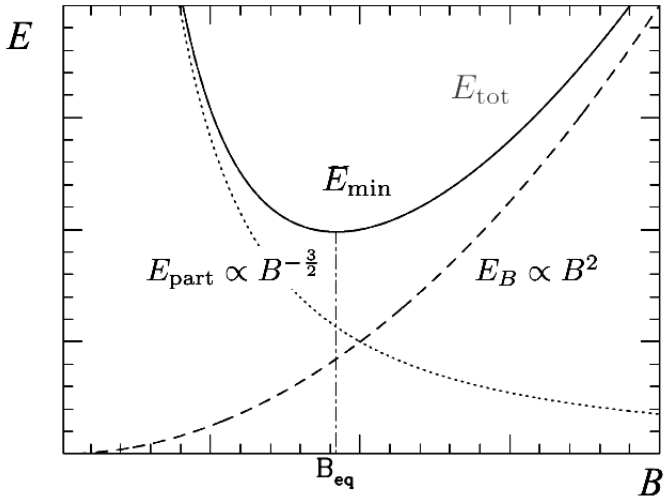

Figure 1.9: Energy content in a radio source (in arbitrary units): the energy of the magnetic field is $U_B \propto B^2$, the energy of the relativistic particles is $U_p = U_e + U_p \propto B^{3/2}$. The total energy content U_t is minimum when the contributions of magnetic fields and relativistic particles are approximately equal (equipartition condition). The corresponding magnetic field is commonly referred to as equipartition value B_{eq}.

1.6 Duty cycle

The duty cycle of an astrophysical source is generally defined as the fraction of time during which the source is active (Romano et al. [2014]). We know that the AGN jets are not constantly active through the entire life of the host galaxy, i.e. when the SMBH stops accreting material and jet activity ceases. This is what usually happens after a period that lasts between a few tens and a few hundred million years. According to that, it is thought that active and quiescent phases occur one after the other with variable timescales, if some conditions are satisfied, i.e. the presence of new fuel is mandatory for the resumption of the process.
The knowledge of the duty cycle is important for galaxy evolution because the AGN energy released in the environment during the active phase helps us to investigate AGN feedback, which is essential to study how SMBH impact the galaxies' growth and the thermal evolution of the ICM and IGrM.
Shabala et al. [2008] found that both the radio source lifetime and duration of the quiescent phase have a strong mass dependence, with massive ones hosting older sources and activities triggered more frequently. They also found that the ICM and IGrM cooling rate shows a similar mass dependence, suggesting that fuel depletion is the reason the jets switch off.
Fuel depletion happens because jets heat the ICM during the active phase, this induces a decrease in the accretion rate into the central black hole, this process can go ahead until the lack of cold gas ends up the accretion process. Once the gas has had sufficient time to cool, the accretion can restart, leading to the possible formation of a new pair of jet and younger electron population lobes.
A powerful jet activity could also carry away all the SMBH fuel from the central re-

gions, stopping future possible episodic activities, but dynamical events, i.e. galaxies' close encounter interactions, could act as a gas replenisher (Bahcall et al. [1997]). As a consequence, once the gas accretion rate is increased, jets can be launched again.

Galaxy evolution simulations have shown that the intermittence of nuclear activity is required to counterbalance the cooling mechanism in galaxies, despite there are manifold uncertainties involving accretion physic and jets formation, a few authors have attempted to develop analytical models and numerical simulations to describe the origin of jets and evolution (e.g. Clarke and Burns [1991]; Clarke [1997]; Reynolds and Begelman [1997]; Mendygral et al. [2012]; Walg et al. [2014]). Some of the main open questions are: to give constraints on the timescales of the active and the quiescent phases of the duty cycle; understand the reasons for the phase recurrence; giving constraints to the physic behind extended radio populations. These are crucial to understanding radio galaxy and the feedback impact in the environment of clusters and groups.

In this thesis, the duty cycle is investigated by modelling the radio spectrum of the remnant radio galaxy NGC 6086 and has been performed an integrated and resolved spectral analysis of its radio emission. In literature has been used also different approaches trying to achieve the same goal: the study of radio luminosity functions and the analysis of X-ray cavities in galaxy clusters.

1.6.1 Remnant sources

At the end of the active phase, when the accretion process stops, the radio galaxies' jets and hotspots (if present) start to disappear. We can label these sources as *remnant radio galaxies*. During the duty cycle's quiescent phase, the lobe's particle populations and magnetic field still radiate energy through synchrotron emission in the radio band for a limited amount of time. In this phase, the lobes have a luminosity drop, but the timescale and evolution are influenced by the environment around them, i.e. they can expand until the reach of pressure equilibrium or they could already be in pressure equilibrium with the medium when the engine switches off, leading to different spectral shape and evolution.

Studying the spectral evolution of the remnant lobes is difficult because it goes through a series of uncertainties, such as the knowledge of magnetic field power, particle injection indexes, in-situ reacceleration processes and compressions due to medium turbulence. Exhaustive statistical studies could not be done in past decades because the surveys, such as B2 and 3CR samples (Feretti et al. [1984]) or the WENSS minisurvey sample (de Ruiter et al. [1998]) and the B2 bright sample (Colla et al. [1975]), identified just a small fraction (1-3%) of the galaxies as remnant radio galaxies.
This paucity could be caused by the concurrence of multiple reasons: the emission become invisible faster than expected when the engine switches off; we have said that synchrotron emission and IC scattering mechanism act together on the electron populations, but IC emission becomes dominant when redshift is higher than $z \sim 0.5 - 1$

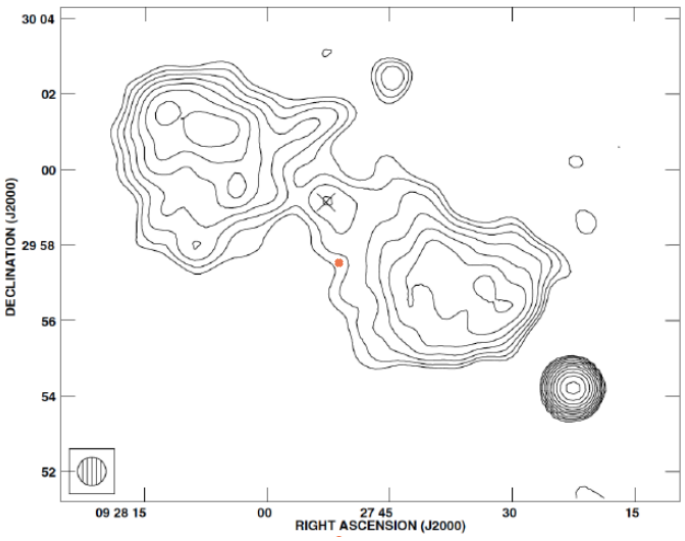

Figure 1.10: Example of a radio map for the remnant radio galaxy B2 0924+30 from Jamrozy et al. [2004];

due to the increase of the volume density of the CMB radiation. For this reason, is still really challenging to find a high number of remnant radio galaxies at higher redshift even with the new telescopes.
The main improvement in the new surveys is that now we are able to perform low-frequency observation with higher resolution and higher sensitivity. Since this kind of emission is brightest at lower frequencies and MHz surveys are now very sensitive thanks to the new generation of radio interferometers (LOFAR, uGMRT, MWA and the future SKA), we are making new steps forward in the investigation of these sources and we are able to perform high sensitivity survey down to tens of MHz in frequency.

Remnant radio sources have been found in different environments. Even if a small number of them have been identified in low-density regions, the majority are found in the galaxy clusters environment. The reason could be that, in clusters, the radio plasma is more confined by the surrounding medium, which slows down the expansion and the subsequent fading and disappearance of the lobes. As already mentioned, the new generation of radio telescopes is finding an increasing number of sources at the moment in order to have the highest statistic available.
One of the aims of new-generation observations is the detection of the oldest AGN jet radio plasma, to study the behaviour of the interaction between aged plasma and surrounding medium through a period that lasts hundreds of million years.
Thanks to their high-sensitivity and high-resolution observations in the MHz band, we are able to see unprecedented details of the synchrotron emission and, likely, we will discover new emission structures, such as the one seen in NGC 507 or the spectacular emission seen in the galaxy group Nest 200047 (Brienza et al. [2021], Brienza et al. [2022]).

The new, cited, detections are the result of the plasma evolution in the radio galaxy environment. The older emission can be disrupted, compressed or spread by the cluster and group dynamics, leading to the generation of atypical structures. For example,

an increasing number of sources presents filamentary emission on different scales and with different shapes (i.e. Nest 200047 has a box-shape filament and the filament of NGC507 has an arc filament). These emissions, alongside high-energy observations and simulations will help to give a better comprehension of the environment around these sources.

1.6.2 Restarted sources

If the central SMBH restarts to accrete thanks to a new inflow of the ICM/IGrM in the inner part of the system, the jets and magnetic field are inflated in the environment again. The large-scale structures formed in the previous active phase (i.e. lobes, cavities, filaments) may have survived during the quiescent phase. This kind of source is called *restarted galaxy*. With radio observations, we can sometimes detect not only the lobes and jets formed in the latest event but also previous AGN activities thanks to their remnant lobes that are still radiating. This is the clearest evidence of the episodic jet activity and they give fundamental constraints on the AGN duty cycle.
We will refer to remnant sources if the radio galaxies do not show an active core at the moment and we will refer to restarted sources if they are detected during a second (or third) active phase with an active core at the moment.

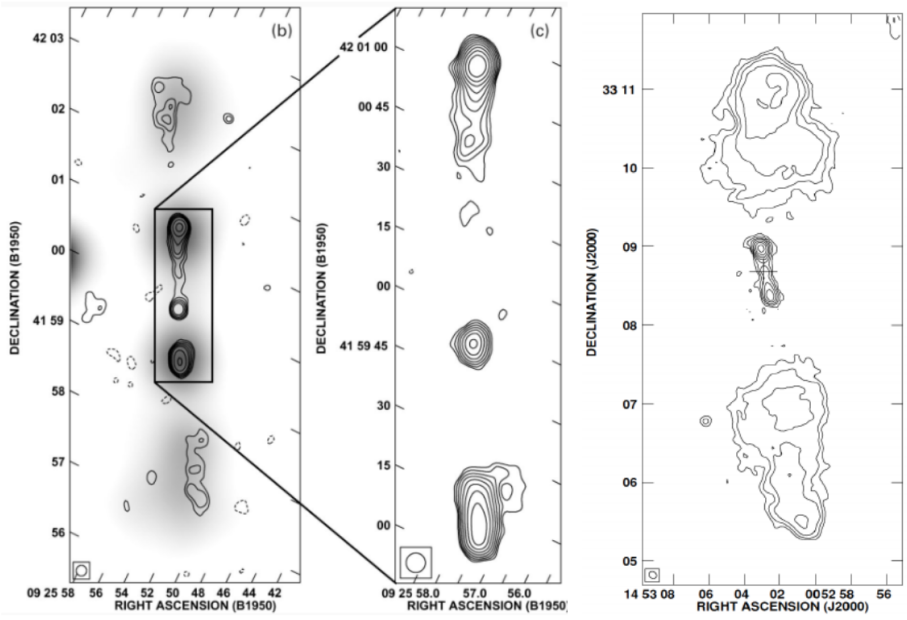

Figure 1.11: Radio contour plots of two sources: B 0925+420 on the left and the result of the restarted activity shown in the zoomed central image (Schoenmakers et al. [2000]; J1453+3308 with radio contours overlaid on the right from Konar et al. [2006].

Double-double radio galaxies (DDRG) are the clearest observational example of episodic jet activity. These sources present two distinguishable pairs of radio lobes, usually aligned along the same direction, with clear evidence of a common central region that originates them. To date, in a limited number of sources have been found

even three pairs of episodic activity.

The taxonomy of restarted sources is characterised by different shapes and morphology, besides the DDRG, such as sources where jets have recently formed and are still embedded in the host galaxy, for example, the compact radio galaxy 3C236.
The reason for the differences in morphological and spectral characteristics observed between restarted radio galaxies could reside in multiple aspects: galaxies could have been observed during different duty cycle phases; the AGN or the SMBH are evolving in different environments; different environments or engines could lead to different radio power values. The little statistic does not help to give the complete picture of the physical processes behind the different sources' morphology.

As it will be presented in Chapter 3 and 5, restarted radio sources give us the perfect environment to analyse multiple aspects of the duty cycle, such as the time between two active phases; how long the inactive and active phases last; how the surrounding environment interferes and first-order age estimate of the different regions of the source.

1.7 This thesis work: NGC 6086

The remnant radio source analysed in this work is called B2 1610+29 and is associated with the nearby ($z = 0.0318$) cD central galaxy NGC 6086, located in the centre of the Abell 2162 galaxy group. The total mass of the system is $3.8 \cdot 10^{13}$ $M_\odot$ (Eckert et. al, in prep.). In the X-ray band, it has been defined as a low-luminosity group, with a value of $L_X = 3 \cdot 10^{42}$ (Burns et al. [1994]). The radio source shows two main lobes that have a projected linear size of approximately 100 $\times$ 30 kpc combined. As presented by previous works (Giacintucci et al. [2007], Murgia et al. [2011]), the morphology of NGC 6086 is what is expected from a typical remnant radio source: it lacks nuclear radio emission, radio jets and hotspots and it shows two symmetric and relaxed radio lobes sitting on the opposite side of the host galaxy. Also in Liuzzo et al. [2010] it was described as a bright cD galaxy, which hosts a double-lobed radio source and without clear substructures. A similar double morphology without a central component was previously found also at 1.4 GHz by Owen and Ledlow [1997] and by Parma et al. [1986]. In particular, Murgia et al. [2011] presented the highest resolution image of the source by combining data at 1.4 GHz with the Very Large Array (VLA) in the B and C arrays. They obtained a final resolution of 5.5 $\times$ 5.5 arcsec^{2}and an RMS (root mean square) noise level of 70 μJy/beam and a flux density consistent with the NVSS (NRAO VLA Sky Survey) flux. In addition, they produced images at 1.4 and 4.8 GHz in the C and D configurations, respectively, and they used these two images to produce the spectral index image of the inner lobes. They confirm the morphological classification of remnant radio galaxy by measuring a steep spectral index between 1.4 GHz and 4.8 GHz with a value of $\alpha_{1.4}^{4.8} = 1.5 \pm 0.02$.

In this thesis, we analyse this source with new observations made in the MHz frequency range with the new generation of interferometers. The new data allow us to perform the most accurate and detailed integrated and resolved spectral analysis to date, in order to take major steps forward in the study of this source. In particular, the

increase in data sensitivity has led to the detection of low surface brightness structures, such as filaments and diffuse emission, that were hidden in past observations. Our purpose is to investigate the spectral properties both in the lobes and in the new structures in order to give constraints on the AGN duty cycle.
Throughout the thesis, we assume a flat Universe model with $H_0 = 70$, $\Omega_M = 0.3$ and redshift $z = 0.0318$, leading to a scale of 0.635 kpc/arcsecond.

Chapter 2

Radio observations and interferometric technique

2.1 Radioastronomy and radio signals

Radio Astronomy is the branch of astronomy that studies the electromagnetic spectrum emission between 10 MHz and 1 THz. Lower frequencies are reflected by electrically charged particles located in the Earth's ionosphere while higher frequencies are part of the microwave regime, in which some frequencies are obscured by atmospheric gas absorption (Condon and Ransom [2016]).
The radio band is characterised by some useful observational properties, such as the possibility to achieve ground-based observations, also in cloudy weather conditions and to cover six decades in frequencies allowing access to broadband radio analysis.

2.1.1 Radio Antennas

To take advantage of radio waves, astronomical signals are captured with antennas. From an electronic point of view, antennas are devices whose purpose is to convert electromagnetic wave signals into electric current signals. Signals go through a receiver and an amplifier and after that, the data computer analysis has to be done.
The simplest antenna is a short dipole (with dipole length $\ll$ wavelength) driven by an oscillating current source. Antennas can be treated as transmitting or receiving instruments, this is confirmed by the reciprocity theorem. The dipole antenna power pattern, defined as the angular distribution of its radiated power, has the same shape as the Larmor radiation from an accelerated charge. Thanks to the previously cited theorem, the receiving response of the dipole to an emitting point-like source, called beam, has the same shape.

The most common radio telescope shape is the paraboloid of revolution and waves are reflected on the paraboloid surface, called the main dish, and then are reflected by the second mirror into the collector. These kinds of telescopes are also-called reflector antennas.
All the reflected waves need to have the same phase when they reach the focal point; this condition is satisfied thanks to the paraboloid shape geometrical properties, but,

in order to do that, waves have to be on-axis plane-parallel. The far-field distance

$$R_{ff} \approx \frac{2D^2}{\lambda} \tag{2.1}$$

where D is the main dish diameter and λ is the wavelength, is the minimum distance of a point-like source to consider its emission formed by plane-parallel waves.
However, depending on the observed frequency, other antenna types can be used (e.g., LOFAR stations, see van Haarlem et al. [2013]).

Antennas do not have the same responses in all directions, they have the highest efficiency in the direction of the pointing and a decrease moving away from that direction. This effect is independent of the antenna diameter. The variation of the antenna response with the angle is called power pattern and it is similar to the diffraction pattern created by a rectangular slit, in the same way as the airy disc is the response to a circular slit.
The functional form of the power pattern is called the $sinc^2$ function and is characterised by a primary (or main) lobe (or beam), followed by secondary (or minor) lobes. The most important value is the half-power beam width (HPBW), it is the width of the primary lobe and it sets the angular resolution limit (or resolution power). The larger the radio telescope diameter, the smaller the HPBW, implying an increase in the angular resolution. This value defines the shortest distance for which two point sources are seen resolved. The power pattern main lobe is also-called the point spread function (PSF) or beam.

2.2 Interferometry

Interferometry was born to answer the necessity to increase the radio image resolution, which, for a single dish telescope, is defined as:

$$\theta_{res} \sim \frac{\lambda}{D} \tag{2.2}$$

with λ wavelength and D single dish diameter.
To perform observations at higher resolution at a fixed wavelength, we need to increase the antenna diameter. The largest single dish ever built is the FAST (Five-hundred-metre aperture spherical telescope, China), which has a diameter of about 500 metres, followed by Arecibo (Puerto Rico), which is 300 metres in width, and their antennas are fixed to the ground, leading to observational pointing limitations. Steerable single dishes are much smaller, due to structural and weight constraints, i.e. the largest fully steerable, single-dish, radio telescopes are the 100 metres Green bank telescope in West Virginia, United States and the 100 metres Effelsberg radio telescope in Bonn, Germany. The building and weight limitations forced the scientific community to move in different directions than the increase of a single dish size. The best solution to get higher angular resolution images was the construction of complex interferometric arrays, formed by numerous single dishes, working all together as one giant telescope, displaced in different combinations and, sometimes, as far as several kilometres from each other.

One of the improvements obtained with the interferometric radio observations over a single antenna can be found in the beam formula, where the single dish diameter is replaced by the length of the baselines, defined as the distance between a pair of single dish antennas, as follows:

$$\theta \sim \frac{\lambda}{b_{max}} \tag{2.3}$$

As mentioned before, antennas can be placed at distances up to tens of km, increasing the angular resolution by three orders of magnitude with respect to a single dish, and achieving unprecedented image quality.
Similarly to Equation 2.3, we can define the largest observable scale by using the smallest baseline available as:

$$\theta_{max} \sim \frac{\lambda}{b_{min}}, \tag{2.4}$$

which is an important value for the study of diffuse emissions.

The collecting area, defined as $A = \frac{\pi D^2}{4}$ for a single dish telescope, is increased by a factor N for an interferometer, where N is the number of antennas in the array. The total number of baselines is given by:

$$N_{baseline} = \frac{1}{2}N(N-1) \tag{2.5}$$

and this is one of the factors that contribute to the total visibility count, presented in Sec 2.3. For this reason, even if the smallest interferometer is made by two antennas, the greater their number, the better the observation results.

The point-source RMS noise of the signal from each dish is measured as:

$$\sigma_s = \frac{2kT_s}{A_e[N(N-1)\Delta\nu t]^{1/2}} \tag{2.6}$$

where T_s is the system noise, A_e is the effective area of the instrument, $\Delta\nu$ is the frequency range and t is the observational time. The RMS value has to be low to have a high sensitivity and, to do that, we need to use the highest number of antennas, increasing the frequency range and the observational time.

The field of view (FOV) is defined in the same way as the resolution for a single-dish telescope: $\theta_{FOV} \sim \lambda/D$, where the numerical factor is the only difference between the formulas. As a consequence, single dish resolution and FOV are values of the same order, while interferometers have a resolution that is much smaller than the FOV.

2.3 Interferometric observations

The source brightness is not directly detected by the interferometer, we have instead a direct measure of its visibilities. Visibility is a complex value defined as:

$$V = \int I(s)\, e^{-2i\pi b\cdot s/\lambda}\, d\Omega \tag{2.7}$$

with s pointing direction, $I(s)$ brightness distribution and Ω fraction of sky covered by the source.
The visibilities produced by two antennas are defined as:

$$V^{ij} = A^{ij} e^{-i\phi^{ij}} \tag{2.8}$$

where indices i and j define two different antennas, A^{ij} and ϕ^{ij} are the visibility amplitude and phase for the baseline formed by the i-th and j-th antennas.

The observed visibilities are not the final value in which we are interested. The sky signal coming from the target suffers from corruption caused by several factors, such as phase distortions due to the atmosphere and amplitude variations due to the electronics. To take into account these variations and correct the visibilities, complex gain values have to be calculated during the calibration process. During an ideal observation campaign, the target is observed together with other sources, called primary and secondary calibrators, used to derive the corrections. Gain solutions are used to correct the registered signal:

$$V^{ij}_{obs} = G^{ij} \cdot V^{ij}_{true} \tag{2.9}$$

where G^{ij} is the gain of that specific antenna pair.

There is a natural cartesian coordinate system for expressing the correlator response of an interferometer, known as the *u,v* plane. The source direction is defined with the 'w' vector (known as the phase centre) and the perpendicular plane to this vector has 'u' and 'v' coordinates. The *l,m* plane is the projection of the celestial sphere on a plane tangential to the pointing direction. In the former plane are mapped the visibilities and in the latter one are mapped the surface brightness values and they relate thanks to the Fourier transform (and vice versa with the anti-Fourier transform):

$$V(u,v) \approx \iint I(l,m)\ e^{-2i\pi(ul+vm)}\, dl\ dm \tag{2.10}$$

$$I(l,m) \approx \iint V(u,v)\ e^{+2i\pi(ul+vm)}\, du\ dv \tag{2.11}$$

Each baseline samples a point (and its complex conjugate) in the *u,v* plane by computing the complex visibility measure, the higher the baseline number, the better the plane sampling, resulting in the best estimate of the surface brightness I(l,m).
Earth rotation plays an important role in interferometric sampling because, through time, the projected plane changes and baselines change their projected plane distances. As a result, longer observation leads to more visibilities and higher sampling. The set of points detected in the Fourier plane is called sampling function $S(u,v)$ or coverage and the total visibility number is given by:

$$N_{vis} = 4 \cdot N_{baseline} \cdot N_{spw} \cdot N_{channel} \cdot \frac{t_{tot}}{t_{int}} \tag{2.12}$$

where the numerical value is representative of the four correlation; *spw* are the spectral windows of the observation; *channel* is the number of sub-frequencies for every *spw*;

t_{tot} and t_{int} are the total time and the integration time respectively.

Since our measures are accessible only where the u,v plane is sampled, what we measure is not the continuous $V(u,v)$ function and it is called the dirty image:

$$I^{dirty}(l,m) = \iint V(u,v) \cdot S(u,v)\ e^{+2i\pi(ul+vm)}\, dl\ dm \tag{2.13}$$

where $S(u,v)$ has a unit value if the point is sampled or has a null value if it is not. To get the true surface brightness, the deconvolution between the dirty image and the dirty beam B (the image PSF) is performed:

$$I^{dirty}(l,m) = I^{true}(l,m) * B(l,m) \tag{2.14}$$

where the last term is calculated as follows:

$$B^{dirty}(l,m) = \iint S(u,v)\ e^{+2i\pi(ul+vm)}\, dl\ dm \tag{2.15}$$

2.4 Interferometers used in this thesis

In this thesis, we have made a spectral analysis of our target NCG 6086 with a multi-frequency approach that aims to investigate the emission spectrum of the source from a few hundred of MHz up to a few GHz. To do that, we have used five observations from three different interferometers, which cover different spectral bands. Observation details are presented in the next chapters while here we introduce the instruments used to make this analysis and their main characteristics.

Karl G. Jansky Very Large Array

Figure 2.1: VLA antennas seen from the ground in the compact array configuration and seen from a few metres up in the air. Credit: NRAO/AUI/NSF.

The Very large array (VLA) is the National radio astronomy observatory (NRAO) interferometer, built in Socorro, New Mexico. It is formed by 28 antennas with a 25-metres diameter (twenty-seven of which are operational, while one is always through maintenance), displaced in a Y-shaped configuration through three 21 km long arms.

When the antennas are all active there is a maximum number of 351 baselines with the longest baselines spacing 40 kilometres from each other (reached with the widest configuration).
The distance between telescopes can be changed, in order to have a higher sensitivity to smaller scales (longer baseline) or larger scales (smaller baseline), thanks to the binary in which antennas can be moved. There are four VLA configurations, from A (longer baseline) to D (closer configuration). Before the start of an observational campaign, the configuration (one or more) has to be chosen carefully depending on the target and the scientific goal. There is the possibility to use a hybrid configuration (i.e. BnA), to avoid the problem of the asymmetric beam when the source has a small declination.
The VLA was inaugurated in 1980 and over 40 years it has undergone several improvements, in particular $\sim$ 15 years ago the receivers have become wide-band, with a sensitivity increase by about an order of magnitude.

Low-Frequency Array

Figure 2.2: LOFAR coverage across European countries on the left and the Superterp, the heart of the LOFAR core, on the right. The large circular island encompasses the six core stations that make up the Superterp. Three additional LOFAR core stations are visible in the upper right and lower left of the image. Credits: https://www.astron.nl/telescopes/lofar/, https://lofar.ie/images/.

The LOw-Frequency ARray (LOFAR, van Haarlem et al. [2013]), is a new generation radio interferometer operated by ASTRON centred in the Netherlands and with stations distributed all around Europe. Using a new design, LOFAR covers the relatively unexplored low-frequency range from 10-240 MHz (corresponding to wavelengths of 30-1.2 m) and provides unique observing capabilities. The all-sky coverage of the dipoles gives LOFAR a large field-of-view (FoV), essential for surveys. This makes LOFAR a powerful instrument in many fields of astrophysics.
Currently, LOFAR comprises 52 individual stations distributed mainly in the northern countries of Europe (Fig. 2.2). Most of the stations are in the Netherlands (38 stations). 24 of these stations are concentrated in an area of 2 km, constituting the Core Stations (CS), located $\sim$ 30 km from ASTRON's headquarters in Dwingeloo. Other stations are located in several countries such as Germany, Poland, France etc. and a station in Italy is also planned as part of the LOFAR 2.0 upgrade, which will occur in

the coming years.
LOFAR consists of an interferometric array of dipole antenna stations, which have no moving parts. Pointing and tracking are then achieved by combining signals from individual antennas to form a phased array. This allows for rapid re-pointing of the telescope and offers also the possibility to perform multiple simultaneous observations from a given station.
In this thesis work, we have used an observation provided by the LOFAR high band antennas (HBA), which operate in the 110-250 MHz range.

Giant Metrewave Radio Telescope

Figure 2.3: Antenna structure of the Giant metrewave radio telescope (GMRT). Image credits: http://www.gmrt.ncra.tifr.res.in/

The Giant metrewave radio telescope (GMRT) is one of the largest and most sensitive fully operational low-frequency radio telescopes in the world, located near Pune, Junnar, in India. It is made of thirty fully steerable parabolic radio telescopes of 45-metre diameter each (almost twice the VLA), which can reach up to 25 km baseline displaced in a Y-shaped configuration, observing at metre wavelengths between 50-1500 MHz with a good angular resolution ($\sim$ arcsec). One of the purposes of this array was to build a very sensitive aperture synthesis radio telescope that will be complementary to both Arecibo and VLA telescopes for investigating many astrophysical problems in the radio band. The antennas are not a conventional (heavy) parabolic structure, they are made up of a series of 4 mm and 2 mm diameter stainless steel wire rope trusses stretched between 16 parabolic frames made of tubular steel. This kind of structure reduces the wind forces on the antenna and reduces the weight by over three times (Ananthakrishnan [1995]). In the last decade, the array has been upgraded and now is called upgraded GMRT (or uGMRT). The upgrade has been proposed in 2007 and started in 2010 and consists of four new wide-band receivers; an increase from 32 MHz to 400 MHz in maximum instantaneous bandwidth; an increase in its sensitivity by up to three times; an updated monitor and control system and several others improvement that makes the uGMRT a more powerful and versatile facility for the radio astronomy community (Gupta et al. [2017]).

Chapter 3

VLA data reduction

3.1 Data

The Common Astronomy Software Applications (CASA, McMullin et al. [2007]) package has been used to perform data reduction on two VLA archival datasets. In these datasets, NGC 6086 and several other sources have been observed at 1400 MHz (L band) with B and C array configurations as presented in Table 3.1. These two datasets have already been used by Murgia et al. [2011] and we take their results as a reference for ours. We have reprocessed these datasets to analyse them in combination with new low-frequency datasets obtained with LOFAR and uGMRT interferometers, presented in Chapter 4.

Telescope	Configuration	Frequency [MHz]	TOS	Date
VLA	C	1400	00:07:00	29/01/1991
VLA	B	1400	00:12:10	21/02/1993

Table 3.1: Observations on which we have performed data analysis and calibration. *TOS* is the time on source for each observation.

3.2 Main calibration steps

Interferometric observations collect a huge number of visibilities, but we have to take into account also the so-called radio frequency interference and instrumental interference that corrupt our data. The main goal of calibration is to be able to correct for effects that may interfere with the scientific outcome of a measurement.
Calibrators are point-like sources used to determine the right visibility corrections. The primary, or flux, calibrator is a non-variable flux object, observed (usually) at the beginning or the end of the observation and it is used to set the amplitude scale in physical units. There are few flux calibrators that are constantly monitored to know their fluxes with high precision. The secondary, or phase, calibrator is used to remove time variation of the phase caused by the atmosphere, antenna position errors and antenna/electronics errors. It has to be near the target (in the sky plane) and it is

observed usually more than one time, before and after the target, to have a good phase sampling.

The data calibration steps are:

- flagging: the first step is the removal of bad or corrupted data. The strongest interference has to be removed at the very start of the data reduction, to delete data that will compromise the calibration. During the next steps, some minor flags can be done on the data to improve the measurement set (MS);

- setting the flux density scale: `CASA` sets the flux density scale of the primary calibrator (here, 1328+307 or 3C286). Within the software are stored visibility models of the flux calibrators that are referred to the accurate flux density scale made by Perley and Butler [2017]. We select $3C286\_L$ because we are using L-band observations and, in future steps, we will compare the model flux with the data to derive the conversion factor that has to be applied to the visibilities;

- determining calibration solutions: Antenna zenith-angle dependent gain table is now calculated; then we use the `gaincal` task to generate the gain solution tables. With the `fluxscale` task we use the primary (flux) calibrator to determine the system response to a source of known flux density and assume that the mean gain amplitudes for the primary calibrator are the same as those for the secondary one. This allows us to find the true flux density of the secondary calibrator;

- applying the calibrations: The amplitude and phase gain solutions found are applied (see Formula 2.9) to the observed visibilities, to derive the true visibilities. This is done with the task `applycal`, which is the last calibration step to prepare the source dataset for imaging. This task is used to apply the complex gain solutions found earlier to the source (and to the calibrators).

Once the calibration is completed, it is important to check the results in order to see if there are any irregularities or calibration errors in the data. We can use `CASA` to plot the corrected visibilities of the calibrators and check if they reflect the expected model. As a final step, we can use the `split` task to save the final calibrated data of the target in a separate file.

After the calibration process, clean deconvolution and imaging have to be performed. The task `tclean` has been used for this purpose. The image visualisation and the interactive cleaning are made by using the `viewer` tool. The cleaning steps are:

- cleaning: the Fourier transform of the visibilities is called *dirty map*, which is the convolution between the surface brightness and the beam. We need to perform a deconvolution of the instrumental response on the map to derive the surface brightness (see Equation 2.14). The clean method identifies the signal peaks in the *dirty map* and performs signal subtractions in these pixels. The subtracted values are usually set as the 10% of the *dirty beam* (see Equation 2.15);

- model subtraction proceeds iteratively, with the search for signal peaks in every cycle. The subtraction process can be stopped in two ways: by reaching a total iteration number or by setting a threshold to the level of the peaks, which usually

corresponds to 3 or 5 times the image noise. In this phase, two nested loops are implemented: the major and the minor cycles. Before the beginning of a major cycle, we can define an iteration number and a threshold for the minor one, which are used as conditions to terminate the minor cycle iterations and trigger the next major cycle (i.e. setting 100 as the maximum minor cycle iterations means that the first major cycle will have 100 minor iterations. This is true if the minor cycle threshold value is not reached before the last iteration). The presence of these cycles is very useful to perform interactive cleaning and see how the *dirty map* changes during the process;

- subtracted components are not cancelled, instead, the algorithm records them. Each iteration adds new components to the so-called *clean component list*. Meanwhile, the initial *dirty map* becomes the *residual map*. When the process is completed, the residual map should contain only the noise;

- restore: the final *clean components* are convolved with the gaussian fit of the *dirty beam* central lobe, called *clean beam* and added to the *residual map*. This last step produces the final *clean image*.

Self-calibration

Self-calibration is a further process of calibration which aims to remove residual calibration errors by using a model for the visibilities obtained from the target field itself. These artefacts are associated with all sources, but in the low-luminosity ones, they do not emerge above the noise value, for this reason, the brightest sources are those that will benefit the most from the self-calibration process.
In the main calibration procedure, we have transferred phase gain solutions from the phase calibrator to the target, but the signal passes through a ionosphere which is different whether we look in the direction of the target or in the direction of the calibrator. This leads to residual calibration errors. Errors can be attenuated with the self-calibration method. The strategy is to generate new calibration tables with `gaincal` and apply them with `applycal` as we have done before, the only difference from the previous data calibration is that we use the target field itself as a calibrator. In particular, the *clean image* is used to generate a field model that is used to refine the gain phase solutions. The new solutions are applied to the visibilities and with the corrected visibilities a new image is created, which will be used as model for the next iteration. We stop the recursive process when we have the best possible solutions, which means that further iteration does not improve the image and the noise value does not decrease.
In self-calibrating the data, it is useful to keep in mind the structure of a measurement set (MS). There are three columns of interest: the DATA column, the MODEL column, and the CORRECTED_DATA column. In normal usage, as part of the initial split, the CORRECTED_DATA column is set equal to the DATA column.

In more detail, the self-calibration steps are:

- producing an image with `tclean` using the DATA column. We aim to obtain a model of the field, it is important to adopt a conservative approach and not

perform deep cleaning, in order to avoid cleaning imaging artefacts or substructures but storing just the source flux density. The source model is converted into model visibilities that are inserted into the MODEL_DATA column;

- using `gaincal` to derive the phase gain corrections, produced by comparing the data and the new MODEL column. These are stored in an external table;
- applying the new table to the data to produce a new CORRECTED_DATA column, overwriting the previous one;
- the amplitude calibration is an optional part of the self-calibration process. It has to be applied only if amplitude-based artefacts are seen. The wrong application of this calibration is dangerous because will change the flux of the sources and introduce artefacts.

The procedure can be performed multiple times to have progressively better solutions. The criteria used to terminate the self-calibration is to look at the field noise. When the noise value in the field does not decrease, it means that the best possible solutions have been found so we do not see any further improvement with other iterations.

The calibration is a central part of in the data reduction of radio observations because having the best images is crucial to draw good physical conclusions and correctly analysing and identifying the radio emission.

C configuration

The first observation analysed for this thesis is the one made in 1991, using the C configuration of the VLA interferometer array. The target NGC 6086 is named 1610+296, while the flux density and phase calibrators are 1328+307 (or 3C286) and 1219+285, respectively. The observing integration times of the three sources are shown in Table 3.2.

Name	Scan	Time
1610+296	40	00:07:00
1328+307	16, 26, 38	00:10:30
1219+285	18, 27, 37, 42	00:14:00

Table 3.2: Target and calibrators observations with the total amount of observational time for each one (cumulative when observed multiple times).

The very first thing to do is to check the antenna position used in the measurement set (MS) using the task `plotants`, in order to see if there are antennas that need to be flagged and to display the geometry of the array. For this MS the antennas are in the right disposition (Fig. 3.1). Knowing the disposition of the antennas is useful also because a reference antenna has to be chosen for some calibration tasks. It has to be near the centre of the array and it will have unity amplitude and null phase by assumption, before this choice, the good quality of the antenna data has to be checked.

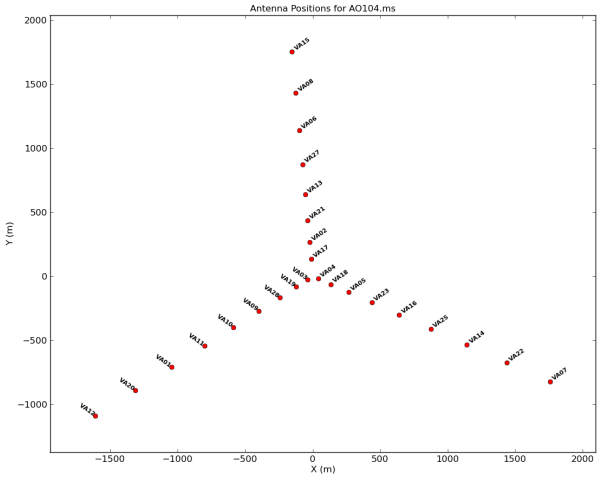

Figure 3.1: VLA array C antenna position.

The data analysis starts with data inspection to identify bad data to be flagged. In the very first step, it is advisable to remove only clearly corrupted data to maintain data that just need to be calibrated. Fig. 3.2 shows two useful plots of the calibrators for a first-order data evaluation: the left panel shows the amplitude of the visibilities as a function of the distance between all the antenna pairs (in wavelength unit). Since the longer baselines have a smaller angular resolution, they are sensitive to compact objects and collect less surface brightness, ending with lower amplitudes with respect to the shorter baselines; the right panel shows the amplitudes versus the observational time, every integration time produces a column in the plot. The observation does not show major corrupted data so we do not need to flag any data points before the calibration procedure.

As mentioned at the beginning of this chapter, the calibration starts by setting the flux density scale. The calibrator used for this purpose is 3C286, a bright point source observed for a few minutes in order to have a high signal-to-noise ratio (SNR). In the task `setjy`, a model has to be chosen for the flux density setting. In our case, we set the task parameter $model = 3C286\_L$ (with the format: calibrator _ band) and it refers to the accurate flux density scale made by Perley and Butler [2017].

The second step is correcting for antenna positions with the task `gencal`. If the antenna positions are incorrect, u and v will be calculated incorrectly and there will be errors in the image because the visibility function is a function of u and v.
After setting the flux density scale, we are ready to generate the gain solution table.It is useful to check the gain solutions found with `plotms` before applying the calibration. We use the `fluxscale` task to produce a new calibration table containing properly-scaled amplitude gains for the secondary calibrator.
If the solutions are satisfactory, we can apply them to the target field and to our calibrators to create the final dataset from which to produce the source images.
The results of the calibration are shown in Fig. 3.3. We show in the first row the

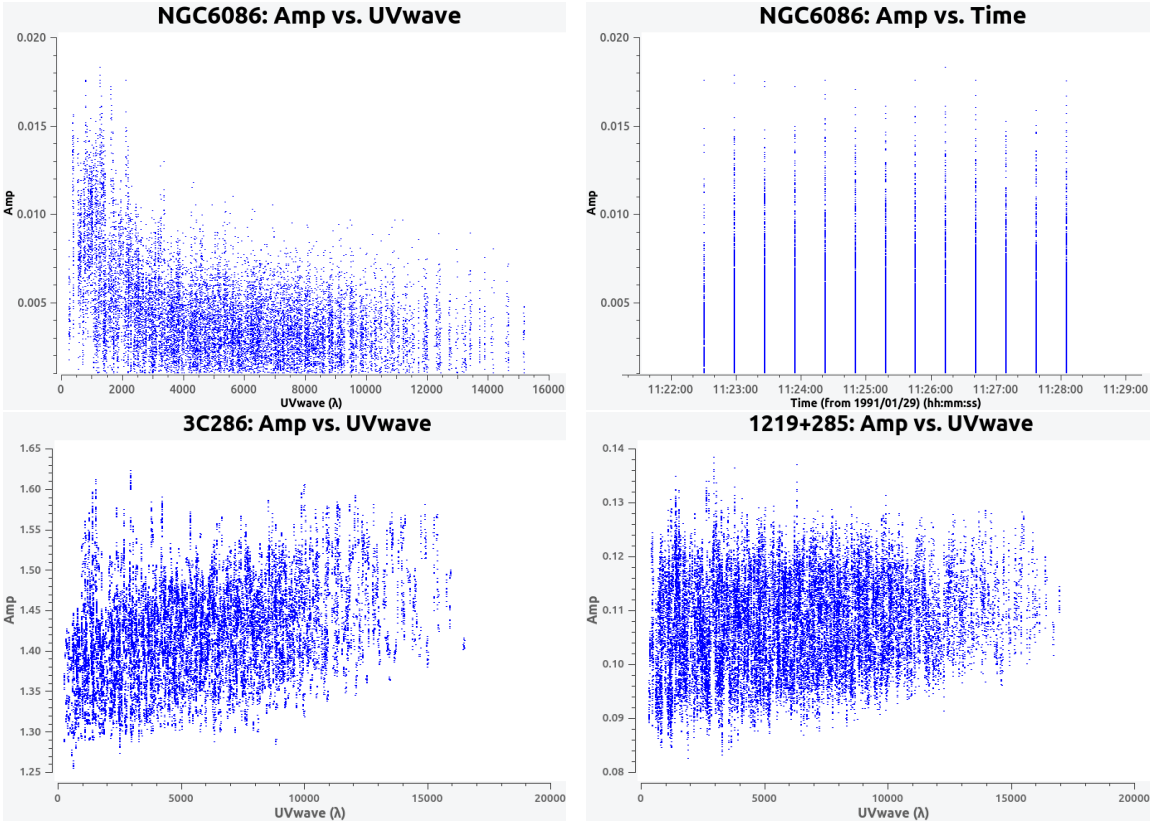

Figure 3.2: Top-left panel: the plot shows the distribution of visibilities with the baseline distances (in wavelength units) versus the amplitudes; top-right: the plot shows target observation in the seven minutes scan, there are not any anomalous peaks in the data. The second row shows the amplitude values of the calibrators versus the baseline distances in wavelength units.

corrected visibilities of the flux calibrator alongside the model of the same source. The amplitude scale obtained is what we expect from the model.

Another plot useful to check if the calibration tables are well calculated is the phase vs. UVwave. Data are successfully calibrated if the random phase distribution (from -180 to +180 degrees) become closer to zero degrees for all the sampled point. What we expect from a point source like the calibrators is that the phases are equal to zero because the Fourier transform of a Dirac function (point source) corresponds to a constant function. We show the calibrated phase for the flux density calibrator in Fig. 3.4.

Imaging

As described in Sec. 3.2, imaging is the process which converts a list of calibrated visibilities into a raw or *dirty* image. Before the cleaning, we have to choose some parameters of the `tclean` task: *cell* is the parameter used to define the pixel size. To be able to uniquely characterise a signal, we must sample it at a rate (Nyquist rate or Nyquist sampling) that is more than twice the maximum frequency in the

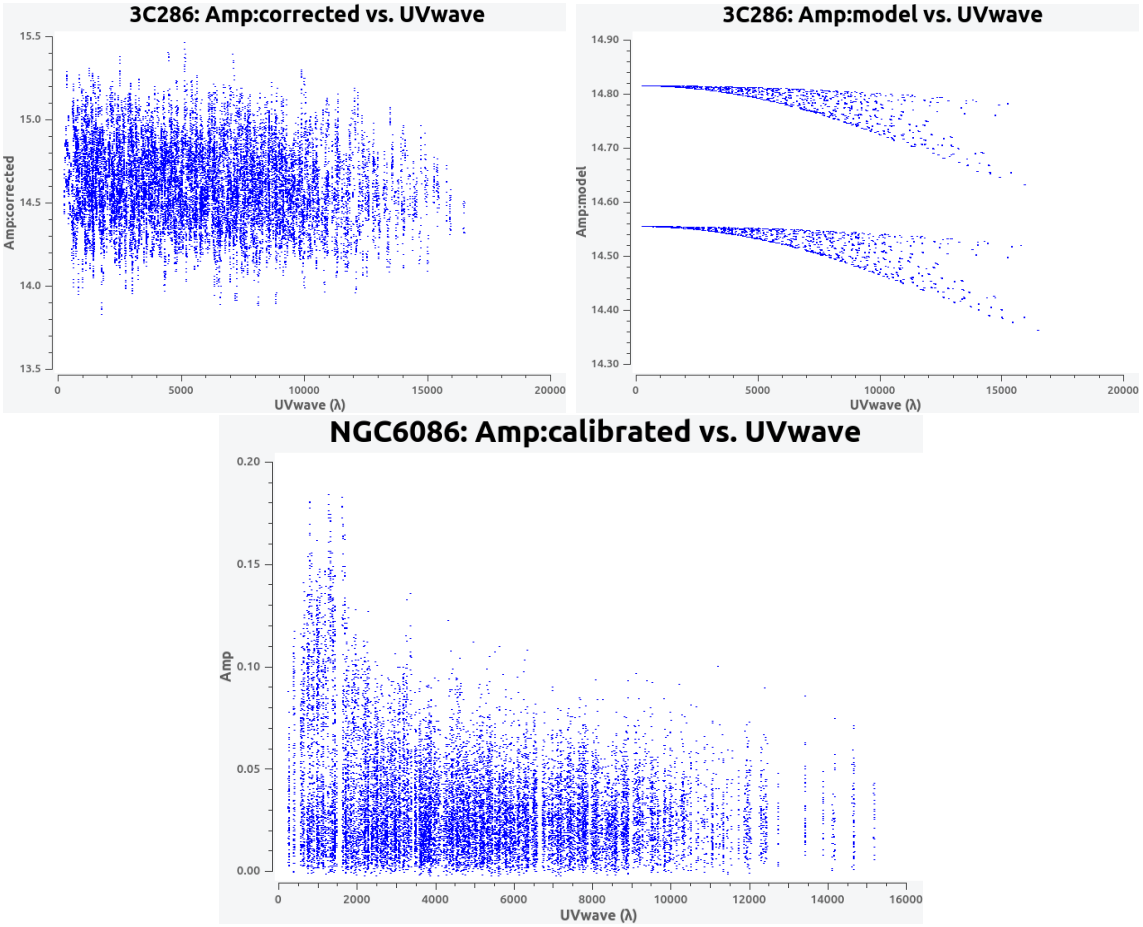

Figure 3.3: In the left panel is shown the result of the calibration on the flux calibrator. There is a visible difference with respect to the initial amplitudes, shown in the bottom-left panel in Fig. 3.2; the right panel shows the model used for the calibration of the amplitudes, with values perfectly in line with our results; bottom panel: the application of the calibration is visible on the y-axis which presents a rescaling of the target amplitude.

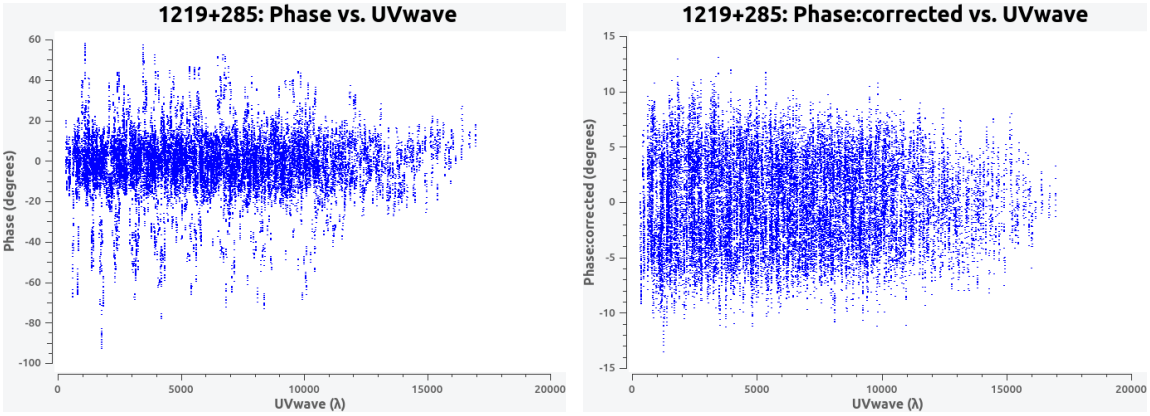

Figure 3.4: Phase angle of the phase calibrator 1219+285 before (left) and after (right) the calibration process.

spectrum of the signal. If we sample the signal less than the Nyquist rate, we will have aliasing, which means we can not reconstruct the signal. To be sure of avoiding aliasing, we sample the beam five times, this means that the *cell* parameter has to be set as the fifth part of the resolution element (or beam), which is calculated as $\theta = b_{max}^{-1} \cdot 206265$ [arcsecond]; *imsize* is how large an image is in pixel unit, a good value for this parameter can be calculated as FOV/pixelsize. It is advisable to have an image that is large, at least, as the primary beam, in order to map the entire sky region observed by the telescope.

Configuration *C* cleaning process results are shown in Fig. 3.5. The figure shows NGC 6086: the FOV size image before and after the cleaning process; the radio contours overlaid to the initial and final image (zoomed on the target) with radio contours overlaid at (-3, 3, 6, 10, 14, 18)$\times\sigma$ levels, $beam = 17 \times 14$ arcsecond, PA62 degree. In the figure are shown the improvements of the observation after the calibration process, it can be seen in the lower artefacts in the FOV and in the higher flux detected in the source region. We overlaid radio contours to the image because they help us to define the source shape and size and they will be used to measure the flux density inside the 3σ contour in Chapter 4. σ is the root mean square (RMS), measured in four boxes throughout the FOV that do not include any source inside; the arithmetic average σ inside these regions is used to define the threshold value.

3.3 B configuration

The second observation analysed is the one made in 1993, using the B configuration of the VLA interferometer array, the target is named 1610+296 as the other dataset. The flux density and amplitude calibrators are 1328+307 (or 3C286) and 1607+268 respectively. The observing time of the three sources are shown in Table 3.3.

Name	Scan	Time
1610+296	12	00:12:10
1328+307	4, 21	00:05:00
1607+268	11, 15	00:03:40

Table 3.3: Target and calibrators observations with the total amount of observational time for each one (cumulative if observed multiple times).

The steps to follow are the same as for the *C* array configuration (see Sec. 3.2). Firstly, we use the task `plotants` to inspect the antenna configuration and to choose the reference antenna near the array centre. As it can be seen in Fig. 3.6, there is one antenna positioned outside the B array configuration (antenna *VA13*) and after a check on its visibilities, we have decided to flag it. It is notable that the antenna disposition covers almost twice the distance than the *C* configuration, since the largest baselines are more sensitive to the smaller scale, we expect that more details will show up in this image instead of more diffuse emission.

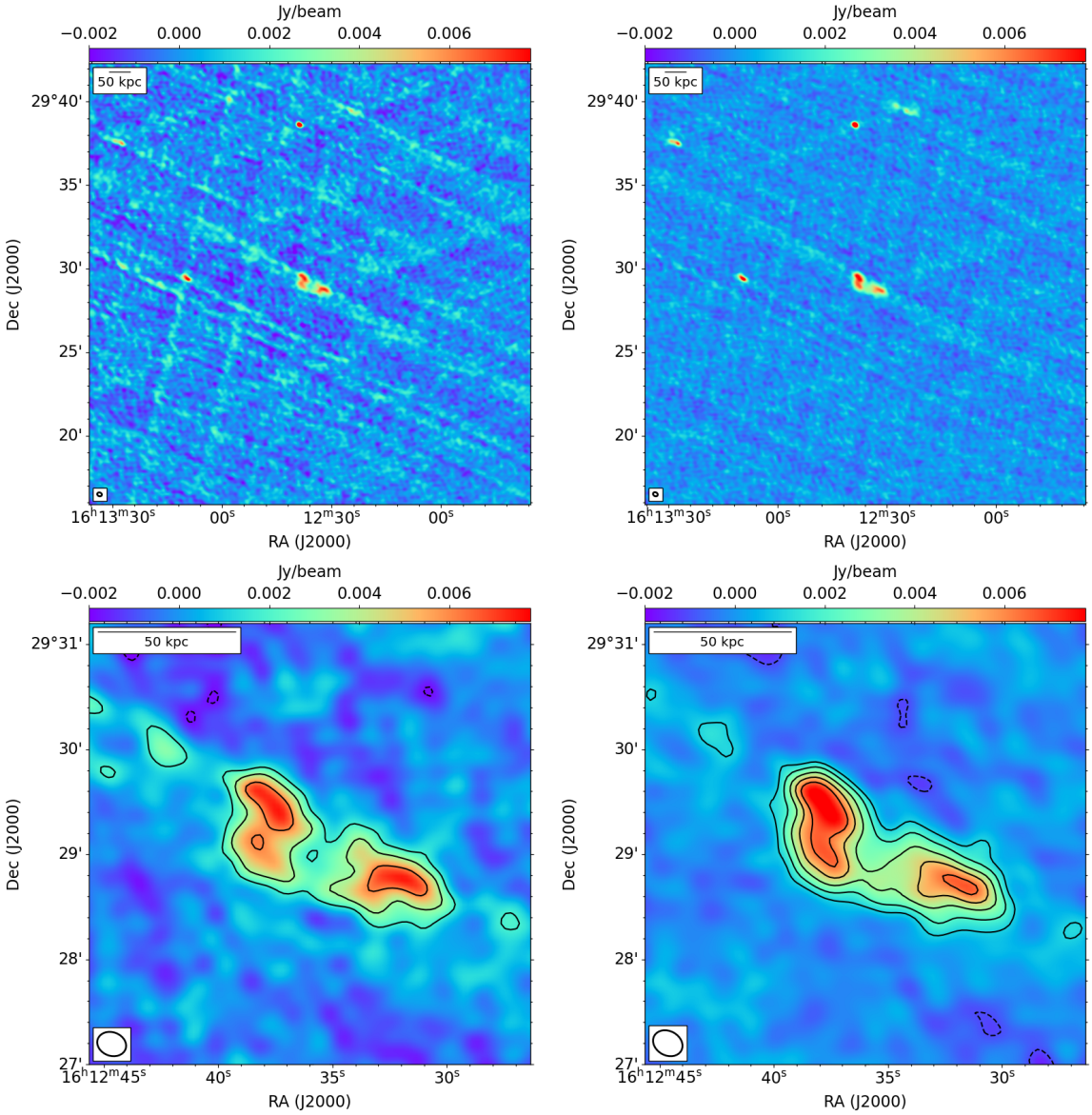

Figure 3.5: First row: FOV size image that shows NGC 6086 with VLA C configuration in the central region and some other minor sources in the surroundings; second row: zoom of the same images on the target, the image in C configuration with radio contours overlaid (-3, 3, 6, 10, 14, 18)$\times\sigma$,
$beam = 17 \times 14$ arcsec^2, PA 62 degree, left image: $noise = 600$ μJy/beam, right image: $noise = 350$ μJy/beam. Left column: resulting image after only 150 cleaning iterations; right column: images achieved after three self-calibration rounds and final deeper cleaning.

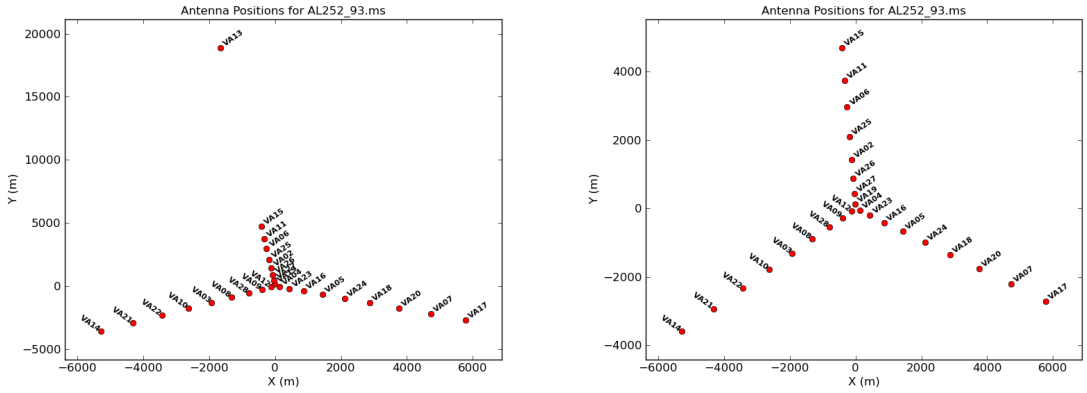

Figure 3.6: Left: VLA array B antennas position in the initial MS; Right: antennas position after the *VA13* flagging, it is significant the variation of values in the ordinate axis.

After the antenna flagging, we can inspect the raw data of the MS. Contrary to the C configuration, there is data interference that has to be flagged, as we can see in Fig. 3.7.

In both figures, there is clear evidence of atypical peaks, probably due to radio-frequency interference (IFR). To remove only the corrupted data, we have analysed which baselines have produced anomalous values and inspected them singularly, in addition, with an amplitude versus time plot we can search if the problem is related just to a single scan for those baselines. This method can help us to save as many visibilities as we can.

After flagging the bad data, the calibration can proceed with the same procedure as previously presented for the C array. The primary or flux density calibrator is unchanged so the `setjy` task has the same *model* of the Perley and Butler [2017] *standard* has before: $3C286\_L$. Moreover, the following steps are the same, calibration table are generated and applied to the target through `gencal`, `gaincal`, `fluxscale` and `applycal` tasks. The results of the calibration are shown in Fig. 3.8. The figure shows NGC 6086: the FOV size image before and after the cleaning process; the radio contours overlaid to the initial and final image (zoomed on the target) with radio contours overlaid at (-3, 2, 3, 5)$\times\sigma$, $beam = 6.3 \times 4.6$ arcsec^2, PA 20 degree and $noise = 200$ μJy/beam.

We show in Fig. 3.9 the results of the calibration on the secondary calibrator phase distribution. The random phases over all the angles become closer to zero, as expected from a good calibration procedure.

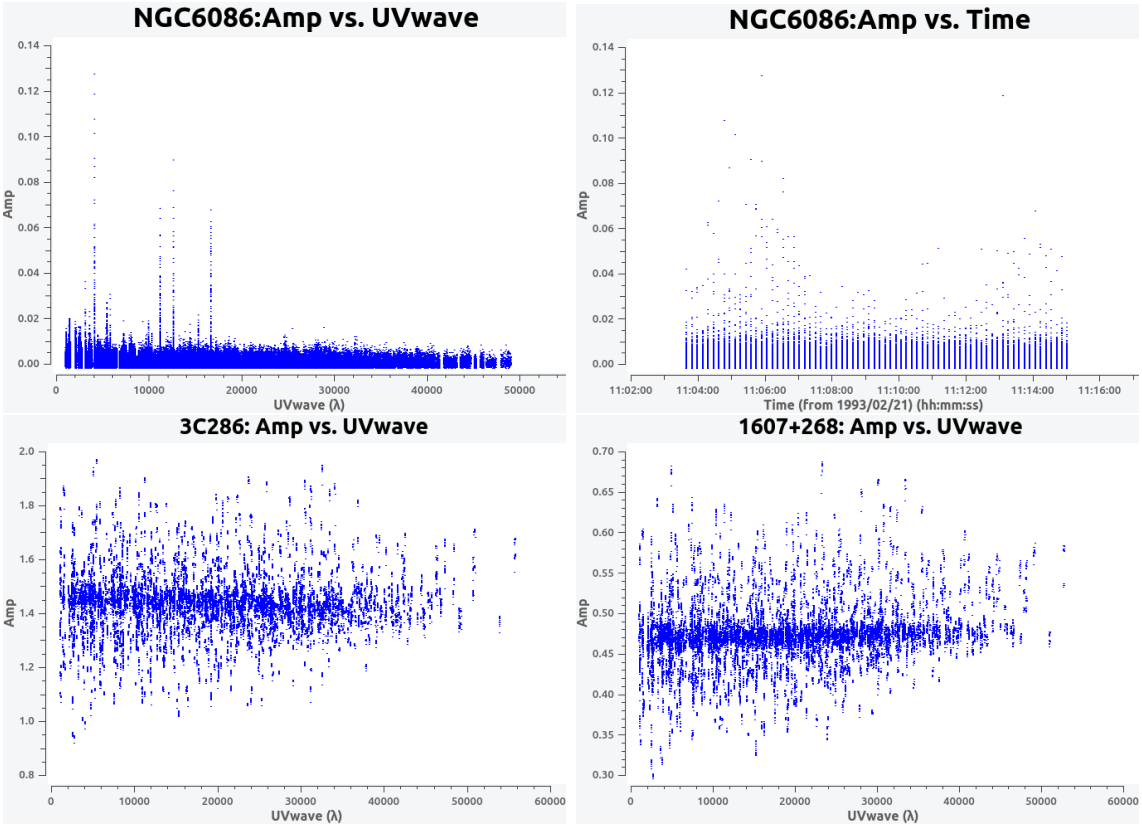

Figure 3.7: Top-left: the plot shows the distribution of source point with the baseline distances (in wavelengths units) versus the amplitudes; top-right: the plot shows target observation in the twelve minutes scan, there are clear anomalous peaks that have to be inspected. The second row shows the amplitude values of the calibrators versus the baseline distances in wavelength units.

Imaging

Imaging this dataset has been more challenging with respect to the C configuration because we are looking at the same extended source with higher resolution and, as a result, we are less sensitive to the diffuse emission. As done in Sec. 3.2, we have plotted the dirty image side by side with the clean one. We have shown the target before and after the self-calibration cycles, in the first row is presented the image with the same size as the FOV, while in the second row, the focus is put on the target. The final image has $beam = 6.3 \times 4.6 arcsec^2$, PA 20 degree and $noise = 200$ μJy/beam. All four images are shown in Fig. 3.10.

3.4 Multi-array VLA images

It is useful to remember that the purpose of this work is to study the spectral age of the plasma throughout the source. To do this reliably, good UV coverage is essential. For this reason, we *combined* the images at 1.4 GHz. Combining two observations at the same frequency allows us to have a sensible increase in the UV coverage and increase

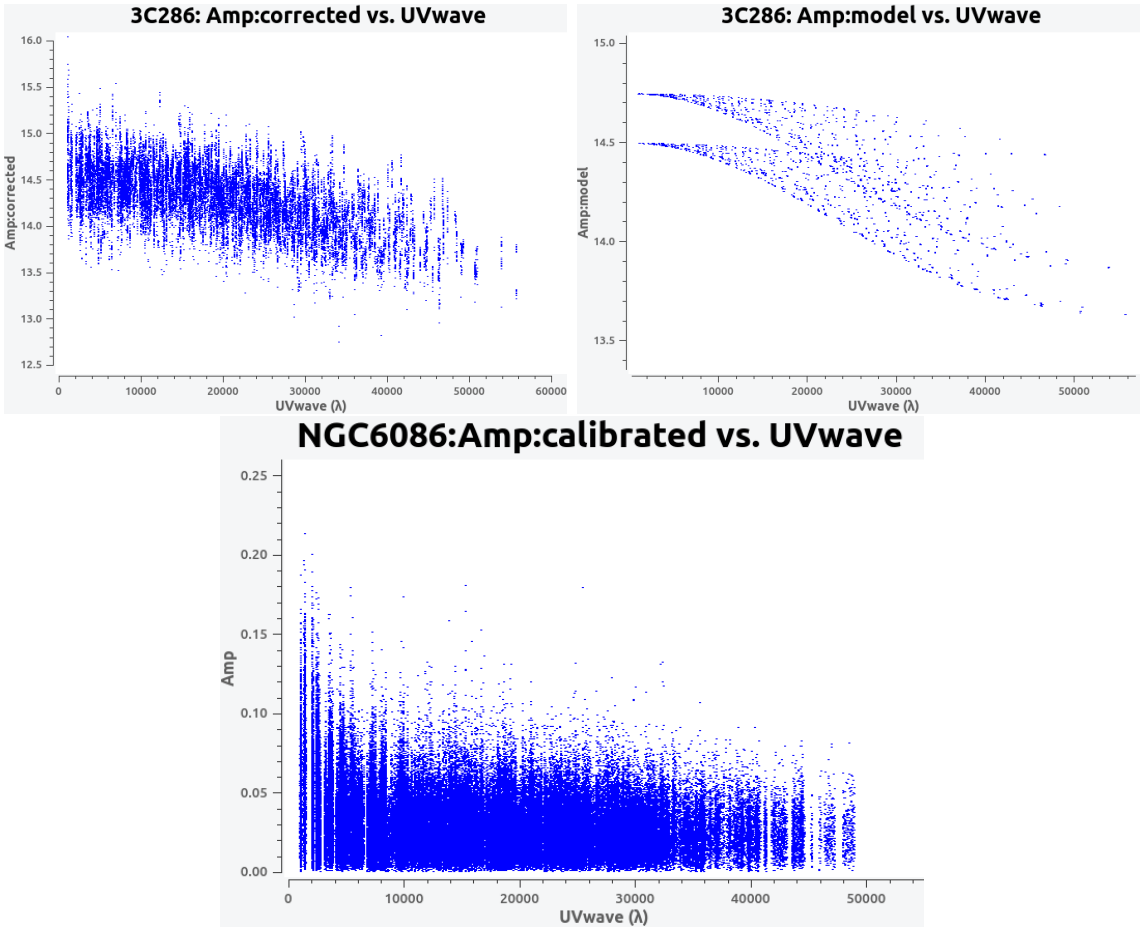

Figure 3.8: In the left panel is shown the result of the calibration on the flux calibrator. There is a visible difference with respect to the initial amplitudes, shown in the bottom-left panel in Fig. 3.7; the right panel shows the model used for the calibration of the amplitudes, with values perfectly in line with our results; bottom panel: the application of the calibration is visible on the y-axis which presents a rescaling of the target amplitude.

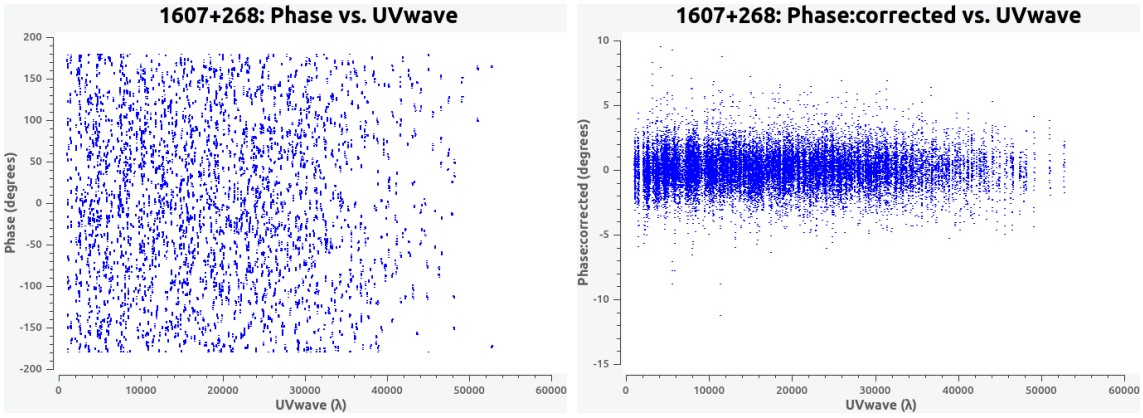

Figure 3.9: Phase angle of the phase calibrator 1607+268 before (left) and after (right) the calibration process.

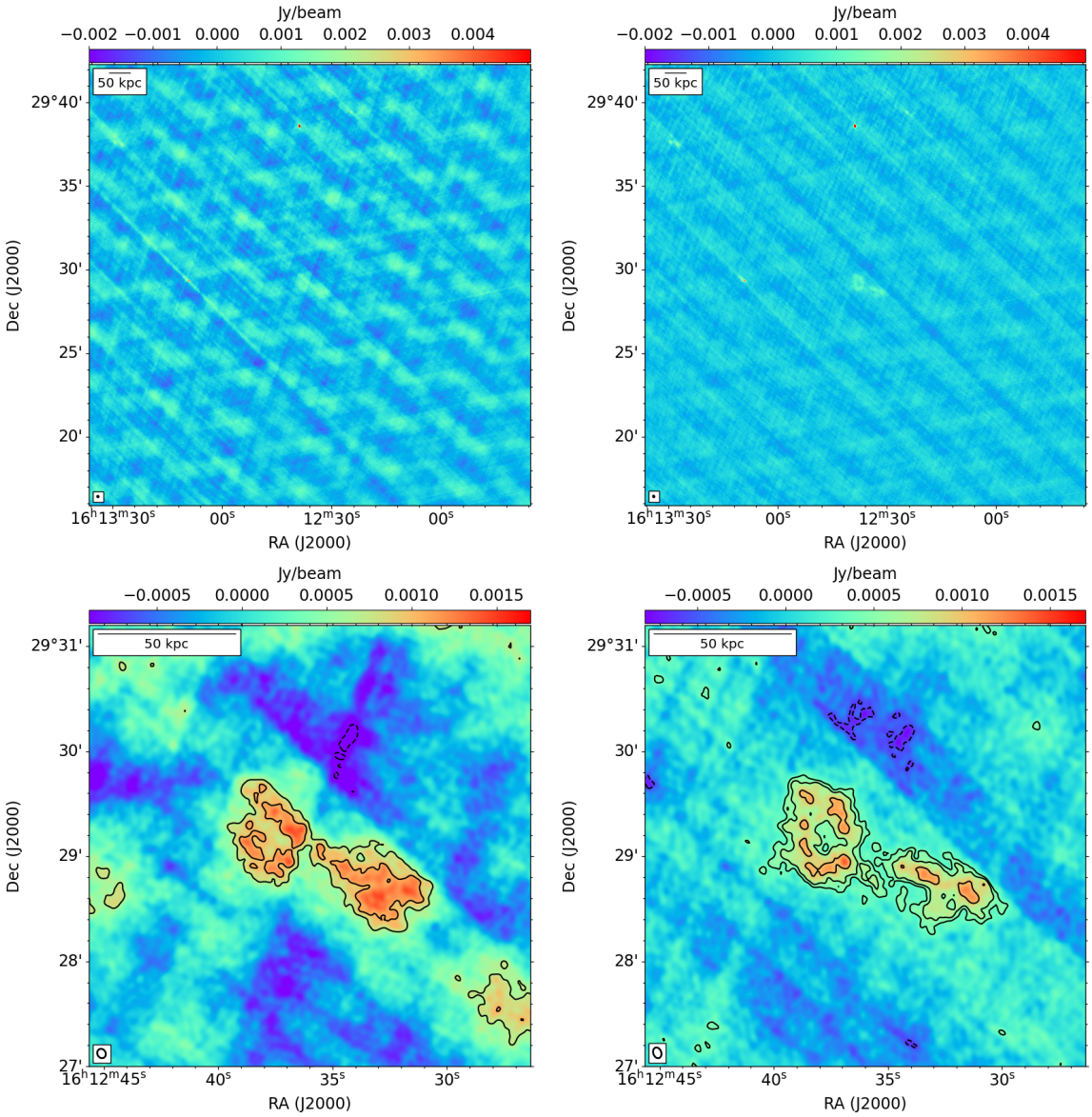

Figure 3.10: First row: FOV size image that shows NGC 6086 with VLA B configuration in the central region; second row: focus of the same images on the target, the image in B configuration with radio contours overlaid (-3, 2, 3, 5)$\times\sigma$, left image: $beam = 5.4 \times 4.7$ arcsec^2, PA 28 degree and $noise = 350$ μJy/beam, right image: $beam = 6.3 \times 4.6$ arcsec^2, PA 20 degree and $noise = 200$ μJy/beam. Left column: resulting image before the cleaning process; right column: images achieved after three self-calibration rounds.

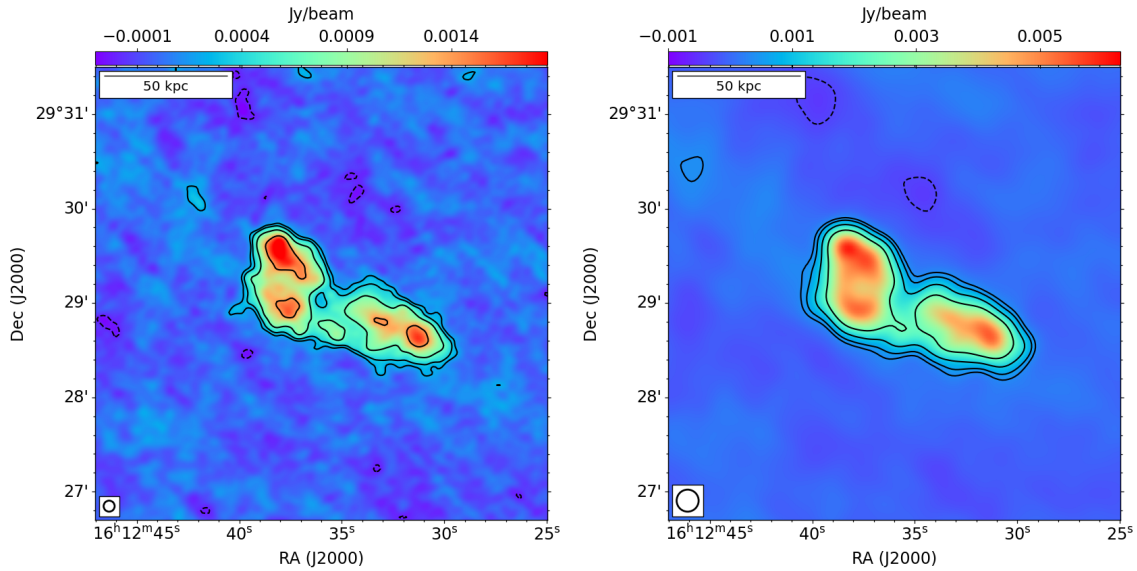

Figure 3.11: NGC 6086 with VLA B+C configuration with radio contours overlaid, left image: (-3, 3, 5, 10, 20)$\times\sigma$ contours, $beam = 7 \times 7$ arcsec^2 and $noise = 70$ μJy/beam, right image: (-3, 3, 5, 10, 20)$\times\sigma$ contours, $beam = 14 \times 14$ arcsec^2 and $noise = 120$ μJy/beam.

the image quality to multiple angular scales.
All the low-frequency images introduced in Chapter 4 and VLA images have been made with a 7×7 arcsec^2 beam. We force the *restoring beam* parameter to the same value and we set the *cell* $= 1.4$ arcsec as a consequence. The source flux density, as measured in the final multi-configuration image at 1.4 GHz, inside 3σ is 99.3 ± 5.0 mJy with a 70 μJy/beam noise. This is in perfect agreement with the value found by Murgia et al. [2011] which is 100 ± 1.4 μJy/beam (has to be noticed that they used a 5.5×5.5 arcsec^2 beam).

In Chapter 4 we will investigate the radio spectrum of the source with multiple frequencies. To have better frequency coverage, we have introduced a 5.0 GHz VLA image with a 14×14 arcsec^2 beam. Therefore, we have also produced a second combined 1.4 GHz image at this resolution. The final images at 1.4 GHz at 7" and 14" resolution are shown in Fig. 3.11. Their noise is 70 μJy/beam and 120 μJy/beam respectively.

Chapter 4

Spectral analysis

4.1 New images

Thanks to the new generation of interferometers we have obtained a unique set of data, covering a very large frequency range from 144 MHz to 5000 MHz. With this new data, we are able to make major steps forward in the analysis of NGC 6086, in particular, thanks to their high resolution and sensitivity, we have performed a resolved spectral analysis down to the lowest frequencies ever used for this galaxy. Murgia et al. [2011] had already examined the same source with an integrated spectral study and resolved spectral analysis made between 1.4-5.0 GHz, where a large fraction of the diffuse emission, however, is not detectable.
In this thesis, we have used a 144 MHz LOFAR observation, a 400 MHz (band-3) observation and a 675 MHz (band-4) uGMRT observation. These are complemented by the 1400 MHz (B+C) VLA image presented in Chapter 3 and, lastly, by an archival VLA 5000 MHz observation. Our image set provides excellent frequency coverage and a massive sensitivity improvement in the longer wavelengths with respect to previous works involving the same source.
To investigate different features of the source, we used three set of images at different angular resolutions:

- high resolution: the first set of images has the highest angular resolution (7" corresponding to 4.4 kpc), sensitive to the smallest scale of the source and tiniest details. This set is used to investigate the presence of filaments, to characterise their shape and emission and to perform the most accurate measures of the size of the components. At this resolution, we have observations at 144 MHz done with LOFAR, 400 MHz and 675 MHz done with uGMRT and 1400 MHz done with VLA;

- mid resolution: the second set has an angular resolution of 14", corresponding to 8.9 kpc. It is used to perform the integrated analysis of the lobes emission, to measure the spectral index throughout the inner lobes and to do a resolved spectral age estimate. At this resolution we have observations at 144 MHz done with LOFAR, 400 MHz and 675 MHz done with uGMRT, 1.4 GHz VLA and 5.0 GHz done with VLA;

- low resolution: the last set of images has the lower angular resolution (30" corresponding to 19.0 kpc) and it is sensitive to the largest scale of the source and diffuse emission. This set is used to investigate the presence of large-scale emission and the characterisation of their spectral shape and age estimate. At this resolution, we have observations at 144 MHz done with LOFAR, 400 MHz and 675 MHz done with uGMRT.

The UV-range is 0.1-40 kλ for the LOFAR datasets, 0.2-33 kλ for the 400 MHz and 0.3-58 kλ for the 675 MHz datasets. The VLA 1400 MHz (B+C configuration)has a 0.3-50.4 kλ range and the VLA 5000 MHz dataset has a 0.6-17 kλ range. To make sure we recover the flux density on the same maximum spatial scales at all observed frequencies, we excluded baselines below 0.3 kλ. This value corresponds to the shorter well-sampled baseline of the VLA 1400 MHz dataset and it corresponds to a physical distance of $\sim$ 60 m.

To perform a spatially resolved analysis of the spectral properties of the source, the images involved must have the same pixel size and restoring beam.

Before the spectral analysis can be performed, it is important to check if the maps are spatially aligned. Indeed, imaging and self-calibration can introduce tiny spatial shifts that can compromise the quality of the spectral analysis (i.e. leading to unreliable spectral index values) and should be corrected. This method consists of selecting a bright point source located near the target (in all the images that have to be matched) and fitting it with a 2D-Gaussian function. We have selected a reference image and shifted the others to have a matched position for the point source in all the images (0.01 pixel accuracy is sufficiently accurate for our analysis). All the image information is reported in Table 4.1.

To emphasise the radio emission on various spatial scales, we present, in Sec. 4.2, two maps at each frequency, one at high and one at low resolution, in particular, the 144 MHz images in Fig. 4.1 include labels for the main morphology regions of our interest, which will be described in Sec. 4.2. The images at 400 MHz and 675 MHz are shown in Fig. 4.2.

4.2 NGC 6086 radio morphology

The radio emission of NGC 6086 is the archetype of what we expect to find in a remnant radio galaxy, showing two lobes without bright hot-spots, jets or a radio core. The two symmetric and relaxed radio lobes are inflated from the central host galaxy in the IGrM as a result of the last accretion activity in the central SMBH. The lobes of this galaxy have already been detected and studied by several authors (Burns et al. [1994], Owen and Ledlow [1997], Giacintucci et al. [2007] and Murgia et al. [2011]), mostly at low resolution, from the low-frequency to few GHz. The dimension of the lobes is $\sim$ 100 kpc $\times$ 30 kpc and they have approximately an elliptical shape, at least in projection. The western lobe is slightly narrower than the other one, but it is more extended along the major axis.

Murgia et al. [2011] performed an integrated and resolved spectral analysis of the lobes between 1.4 GHz and 5.0 GHz, which shows a spectral index steepening from the edges

Telescope	Frequency [MHz]	Beam [arcsec^2]	RMS [μJy/beam]
LOFAR HBA	144	7	100
LOFAR HBA	144	14	160
LOFAR HBA	144	30	300
uGMRT	400	7	30
uGMRT	400	14	60
uGMRT	400	30	150
uGMRT	675	7	14
uGMRT	675	14	28
uGMRT	675	30	80
VLA (B+C)	1400	7	70
VLA (B+C)	1400	14	150
VLA (D)	5000	14	70

Table 4.1: Summary of the observation and images used in this work.

to the central host galaxy.

The morphology of the lobes at low-frequencies is in agreement with the one found in previous works. However, the new images, presented in this thesis for the first time, show new emission, located outside the lobes. The high-resolution images show three peculiar filamentary structures, as shown in Fig. 4.1, left panel. These filaments are located both below and above the inner lobes and are narrow and elongated structures. Their dimensions are approximately 57 × 6 kpc, 54 × 8 kpc and 22 × 10 kpc for F1, F2 and F3 respectively. In the low-resolution image, especially in the 144 MHz one, we have seen previously undetected large-scale diffuse emission (see Fig. 4.1, right panel). The diffuse emission is detected both at low and high-resolution, but with the low-resolution images, we can underline a couple of outer lobes. In particular, the LOFAR observation at 144 MHz has detected this emission in a more extended region than the two uGMRT observations at higher frequencies. This extended emission is likely associated with past phases of jet activity of the central SMBH. The north-east diffuse emission, labelled as D1, reaches up to 165 kpc away from the host galaxy, while the south-west emission, D2, is less expanded and is detected up to 111 kpc away from the SMBH (measures are referred to the 144 MHz observation). In the following analysis, we will refer to the central lobes as *inner lobes* and to the newly detected emission as *outer lobes*.

4.3 Inner lobes analysis

The remnant inner radio lobes are the brightest components of the radio emission and they strongly emerge both at low and high resolution. Thanks to their detection at the lowest to the highest frequencies available, we can have a clear picture of the injection and spectral index of the emission and investigate the synchrotron break frequency, which is fundamental for a good spectral fit in order to give an age estimate of the

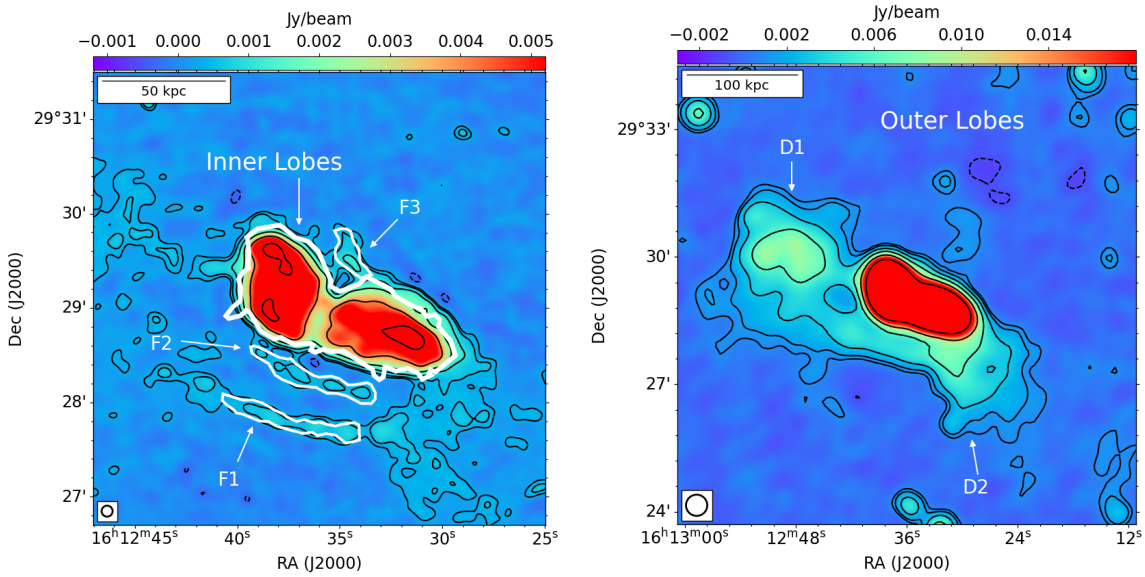

Figure 4.1: Low-frequency radio images of the source NGC 6086 at 144 MHz. The left panel shows the high-resolution (7") image; the right panel shows the low-resolution (30") image. Both images have labels that highlight the most significant features of the system: inner lobes and three filaments (F1, F2 and F3) in the left one; Outer lobes (D1 and D2) in the right one. Beam is shown in the bottom-left corner and a reference scale in the top-left one. Radio contours overlaid: (-3, 3, 5, 10 20, 40, 80)$\times\sigma$ for both the images and the noise values are shown in Table 4.1.

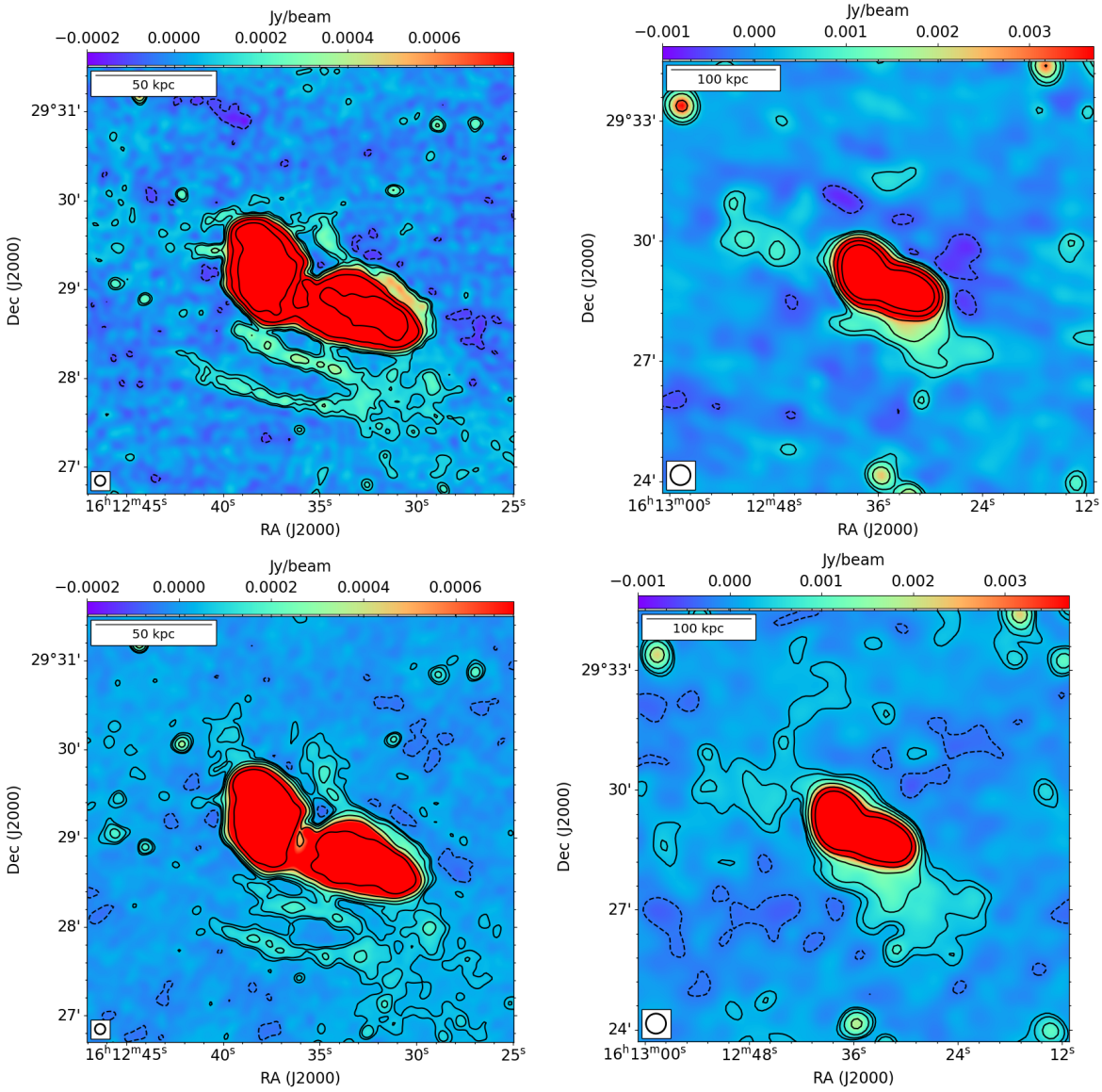

Figure 4.2: Low-frequency radio images of the source NGC 6086 at 400 MHz (upper row) and 675 MHz (lower row). The left column shows images at high-resolution (7") and the right column at low-resolution (30"). Beam is shown in the bottom-left corner and a reference scale in the top-left one. Radio contours overlaid: (-3, 3, 5, 10 20, 40, 80)$\times\sigma$ for all the images and noise values are shown in Table 4.1.

lobes plasma.

To obtain information on the integrated synchrotron spectrum and to look for a possible spectral break frequency, we have measured the flux density of the lobe inside a common region above 3σ. The region inside 3σ of the VLA combined image at 1400 MHz (Fig. 3.11, left panel) is the smallest one compared to lower frequency regions with the same threshold criteria. Table 4.2 shows the frequencies, the flux density values, the noises and the errors associated with the flux density, which are measured as follows:

$$\delta S = \sqrt{(\Delta \cdot S)^2 + (\sigma \cdot \sqrt{N_{beam}})^2} \tag{4.1}$$

where S is the flux density, σ is the noise, Δ is the flux density scale uncertainty (5% for the VLA and 10% for the low-frequency interferometers) and N_{beam} is the number of beams that sample the selected region.
The plot in Fig. 4.3 shows the integrated radio spectrum (blue dots). The linear fit is shown with a red line and returns a spectral index of $\alpha = 0.79^{+0.06}_{-0.07}$, this value is similar to the typical value of active sources, which lies between 0.5 and 0.8. It is clear that the line perfectly fits the points, representing a perfect power law, leading to the conclusion that the break frequency is above 1400 MHz. This is a new result that we did not expect because in the integrated spectrum shown by Murgia et al. [2011] reported in Fig. 4.4 it is clear that the spectral steepening starts at frequencies lower than 1400 MHz. Our low-frequency images, made with high-sensitivity interferometers, show lower flux density values in the 144-675 MHz range and for this reason, the spectrum is flatter than expected. As a consequence, the 1.4 GHz flux density value lies on the best-fit line, instead of beyond the spectral break. The reason why our values are lower than the published values is probably related to a better spatial resolution and image fidelity thanks to new imaging software.

Telescope	Frequency [MHz]	Flux density [mJy]	RMS [mJy/beam]
LOFAR	144	594 ± 59.4	0.1
uGMRT	400	266 ± 26.6	0.03
uGMRT	675	174 ± 17.4	0.014
VLA	1400	99.3 ± 4.98	0.07

Table 4.2: Flux density values measured inside the VLA 3σ region for all the images with the relative flux density errors and noise in the last column.

To look for the spectral curvature in the integrated spectrum, we have added to the four frequencies an archival 5000 MHz observation made with the VLA D array. The compact configuration has been chosen to sample a UV-range as similar as possible to the one at 1.4 GHz (see Formula 2.4).

The highest angular resolution for the new dataset is 14". The target image is shown in Fig. 4.5 with (-3, 3, 5, 10)$\times\sigma$ contours overlaid and a noise of 70 μJy/beam. The other frequency images at 14" resolution are shown in Fig. 4.6 with (-3, 3, 5, 10, 20 40, 80)$\times\sigma$ contours overlaid.

We have measured the flux densities of the inner lobes at all frequencies at 14" resolution. New values are measured using the 5000 MHz 3σ contour and they are presented in Table 4.3.
Fig. 4.7 shows the radio spectrum (blue dots) and the linear fit of the first four points (the red line), which returns a spectral index of $\alpha = 0.80^{+0.07}_{-0.06}$. The linear fit does not include the highest frequency point because we have a clear indication that we have passed the break frequency and the spectrum has a spectral index steepening between 1400 MHz and 5000 MHz.

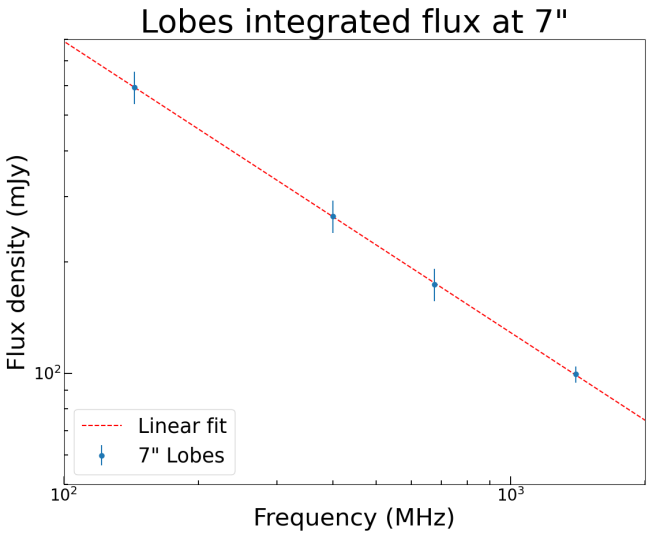

Figure 4.3: The plot shows flux density values (mJy) (blue points) reported in table 4.2 as a function of the frequency, the linear best fit of these values has been found in the red line with $\alpha = 0.79^{+0.06}_{-0.07}$.

Telescope	Frequency [MHz]	Flux density [mJy]	RMS [mJy/beam]
LOFAR	144	569 ± 56.9	0.16
uGMRT	400	239 ± 23.9	0.06
uGMRT	675	167 ± 16.7	0.03
VLA	1400	91.3 ± 4.65	0.12
VLA	5000	20.6 ± 1.15	0.07

Table 4.3: Flux density values measured inside the VLA 5000 MHz 3σ region for all the images with relative flux density errors and noise of the images in the last column.

Using the 14" aligned radio images, we have created two different spectral index maps at low and high frequencies in the range 144-400 MHz and 1400-5000 MHz. The spectral index map is made by measuring, for each pixel, the value of α between two frequencies (see Formula 1.8). The first map allows us to image the spectral index values not only of the inner lobes, but also of the filaments and the region surrounding the inner lobes, whereas the second map allows us to image the inner lobes around the frequency break. To create the spectral index maps, only regions with surface brightness above 3σ in both pairs of radio images were used. Spectral index maps are generated using the `immath` task in `CASA` with the spectral index formula in the *expr* parameter. In the same way, we also generate error maps where the spectral index error is calculated as follows:

$$\alpha_{err} = \frac{1}{\ln \frac{\nu_1}{\nu_2}} \sqrt{\left(\frac{\delta S_1}{S_1}\right)^2 + \left(\frac{\delta S_2}{S_2}\right)^2} \tag{4.2}$$

where ν_i are the frequencies, S_i are the flux densities associated with the frequencies and δS is the absolute flux scale uncertainty.

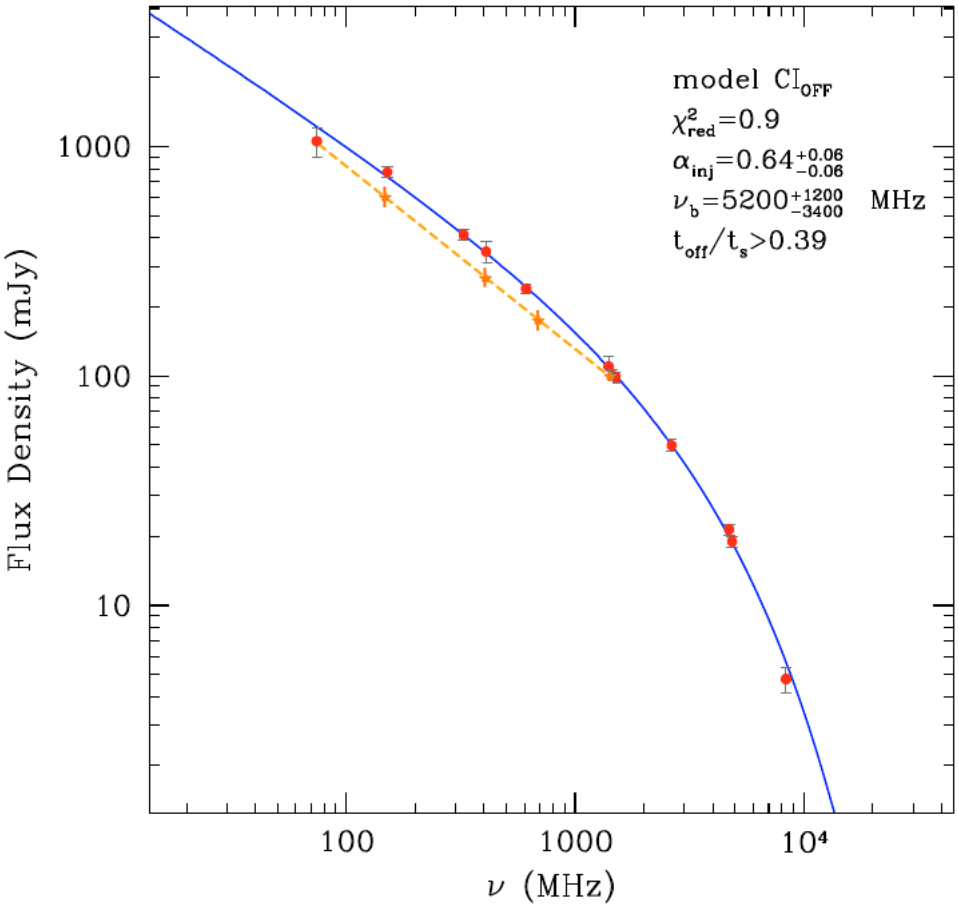

Figure 4.4: The plot shows the integrated spectrum of the source, measured by Murgia et al. [2011] (red point) along with the best fit synchrotron model obtained with the CI_{off} model (blue line). We have superimposed the flux density value of the inner lobes to show the flattening of the new fit (yellow point and dotted line).

Spectral index and error maps are shown in Fig. 4.8 with LOFAR 144 MHz contour at 3σ level overlaid for the low-frequency one and VLA 5000 MHz contours at 3σ level overlaid for the second one. These maps allow us to study spectral index distribution all over the source and search for any trends or gradients that could explain the dynamics and the evolution of the system. The edges of the maps could present some artefacts that have to be excluded from the analysis, i.e. the purple spot in the third panel of the 4.8 figure. This problem occurs in low signal-to-noise regions and so the derived spectral index values are not reliable. We see in the error maps (right column in 4.8) that the edges of the regions are characterised by an error that is around two or three times higher than the central part

We see clearly that the low-frequency image show an $\alpha^{400\mathrm{MHz}}_{144\mathrm{MHz}} \sim 0.8 - 1$ in the inner lobes region, as expected from the integrated spectrum in Fig. 4.7. The only exception is the mild steepening of the central region, where the host galaxy is located, which reaches values higher than 1. We do not recognise any of the clear gradients typically reported in active radio galaxies as already measured by Murgia et al. [2011] between

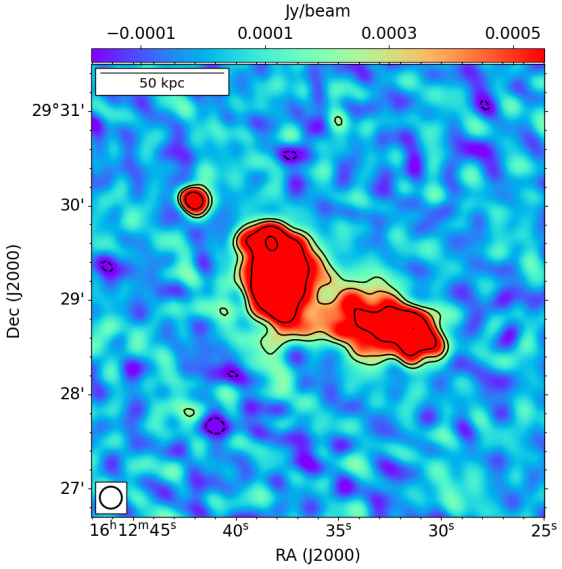

Figure 4.5: VLA (array D) 5000 MHz observation of NGC 6086 with (-3, 3, 5, 10)×σ contour overlaid, noise=70 μJy/beam. The 14 × 14 restoring beam is shown in the bottom-left corner.

1.4 and 5.0 GHz. For example, the FR I have a steepening of the spectral index moving from the centre to the wide edges, while, conversely, the FR II have a flattening moving towards the hotspot (see Sec. 1.2.1). The behaviour observed in NGC 6086 could be associated with an inactive FR II galaxy, but the lack of a clear trend makes the classification very tricky at low frequencies. This is similar to what is observed in the lobes of NGC 507 (Brienza et al. [2022]), while in the remnant radio galaxy B20924+35 studied by Shulevski et al. [2017] there is a clear FR II steepening behaviour. Projection effects and consequent superposition of different particle populations might also play an important role in smoothing any spectral index trends.
In the high-frequency images we are looking at the spectral index distribution beyond the spectral break frequency and the spectral index is more patchy than observed at low frequencies. We can suppose a steepening toward the centre that culminates in the two red steep spectrum regions, located, in projection, on the east and west side of the host galaxy.

To further investigate the trends observed in the spectral index maps discussed above, we selected eleven regions to extract the spectral index profile. The regions are shown with black rectangles in Fig. 4.9. The spectral index profile is shown in Fig. 4.10. We have measured flux densities and derived the spectral indices (see Formula 1.8) between 144-400 MHz (blue dots) and between 1400-5000 MHz (green dots) in the same rectangles. α values are plotted from the east (region 1) to the west (region 11) and we can see clearly that the spectral index map results are confirmed: $\alpha_{144\mathrm{MHz}}^{400\mathrm{MHz}}$ has a uniform value around 0.8 and a steepening in the central part in the sixth region, corresponding to the position of the host galaxy; $\alpha_{1400\mathrm{MHz}}^{5000\mathrm{MHz}}$ always has a steeper value and shows a steepening going from the edges to the centre.

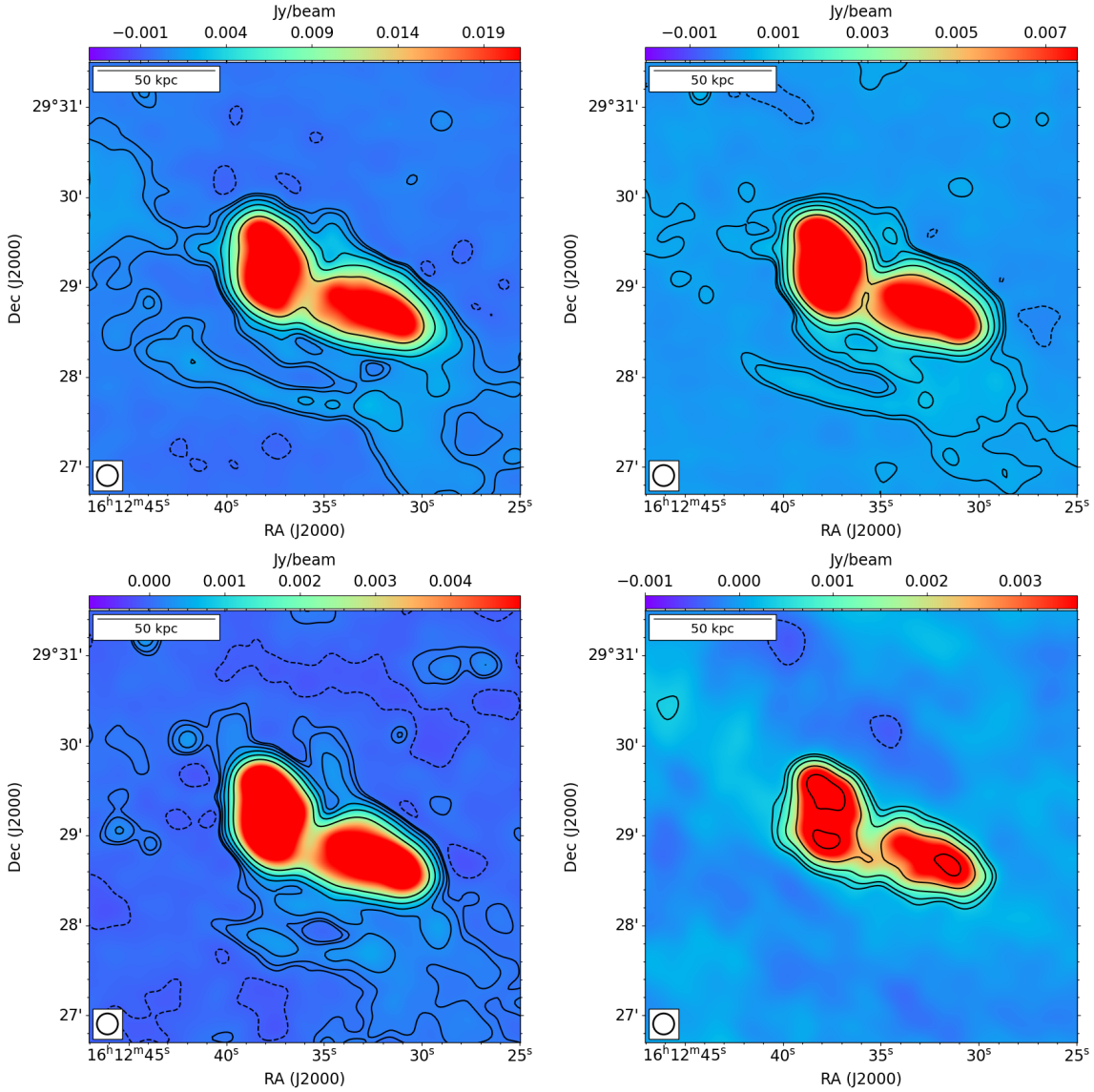

Figure 4.6: Images at 144, 400, 675 and 1400 with 14×14 arcsec^2 restoring beam (shown in the bottom-left corner), (-3, 3, 5, 10, 20, 40, 80)$\times\sigma$ contour overlaid and noise value of 160, 60, 28 and 120 μJy/beam, respectively. A reference scale is shown in the upper-left corner.

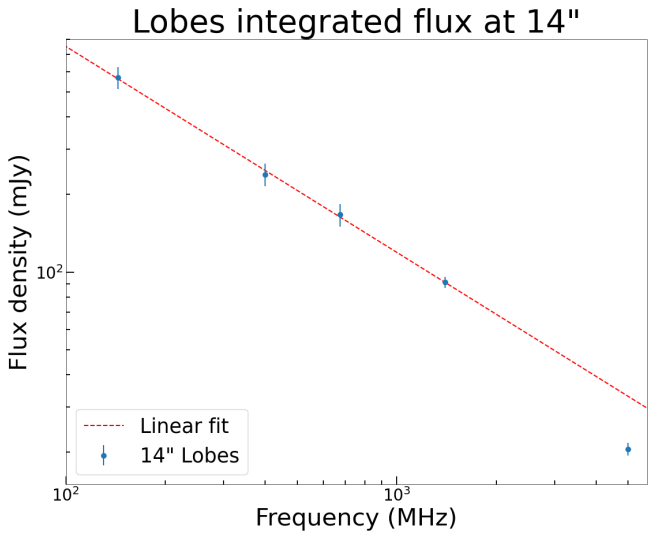

Figure 4.7: The plot shows flux density values (mJy) (blue points) reported in table 4.3 as a function of the frequency, the linear best fit of the first four values has been found in the red line with $\alpha = 0.80^{+0.07}_{-0.06}$. For the first time we have seen a clear indication of the spectral index steepening as a result of passing the synchrotron radiation break frequency.

Further spectral analysis to investigate the duty cycle of the inner lobes at 14" resolution are presented in Chapter 5.

4.4 New diffuse emission

An aspect of great interest in the observations of NGC 6086 is the detection of new diffuse emission surrounding the inner lobes. The study of this emission is crucial to understand the dynamical evolution picture of this system, its interaction with the medium and to constrain the AGN duty cycle. In particular, the new images reveal for the first time incredible new emission features at different scales.

4.4.1 High resolution analysis

High-resolution images at 7" have shown clearly the presence of small-scale multiple filamentary features. The filamentary emission within and around non-thermal radio galaxy is starting to be commonly detected when high angular resolution and high sensitivity observations are available (i.e. NGC 507, Brienza et al. [2022]; NGC 1272, Gendron-Marsolais et al. [2021]; NGC 326, Hardcastle et al. [2019], Nest 200047 Brienza et al. [2021], 3C40A-3C40B Rudnick et al. [2022]). Magnetohydrodynamics (MHD) simulations suggest that such filaments trace enhancements in the magnetic field distribution (e.g. Huarte-Espinosa et al. [2011]; Hardcastle [2013]), which form as a consequence of the complex internal dynamics of the lobes. The origin of these filamentary features is still under debate and several hypotheses have been made such as interaction with the magneto-ionic surrounding medium, plasma escaping from jets,

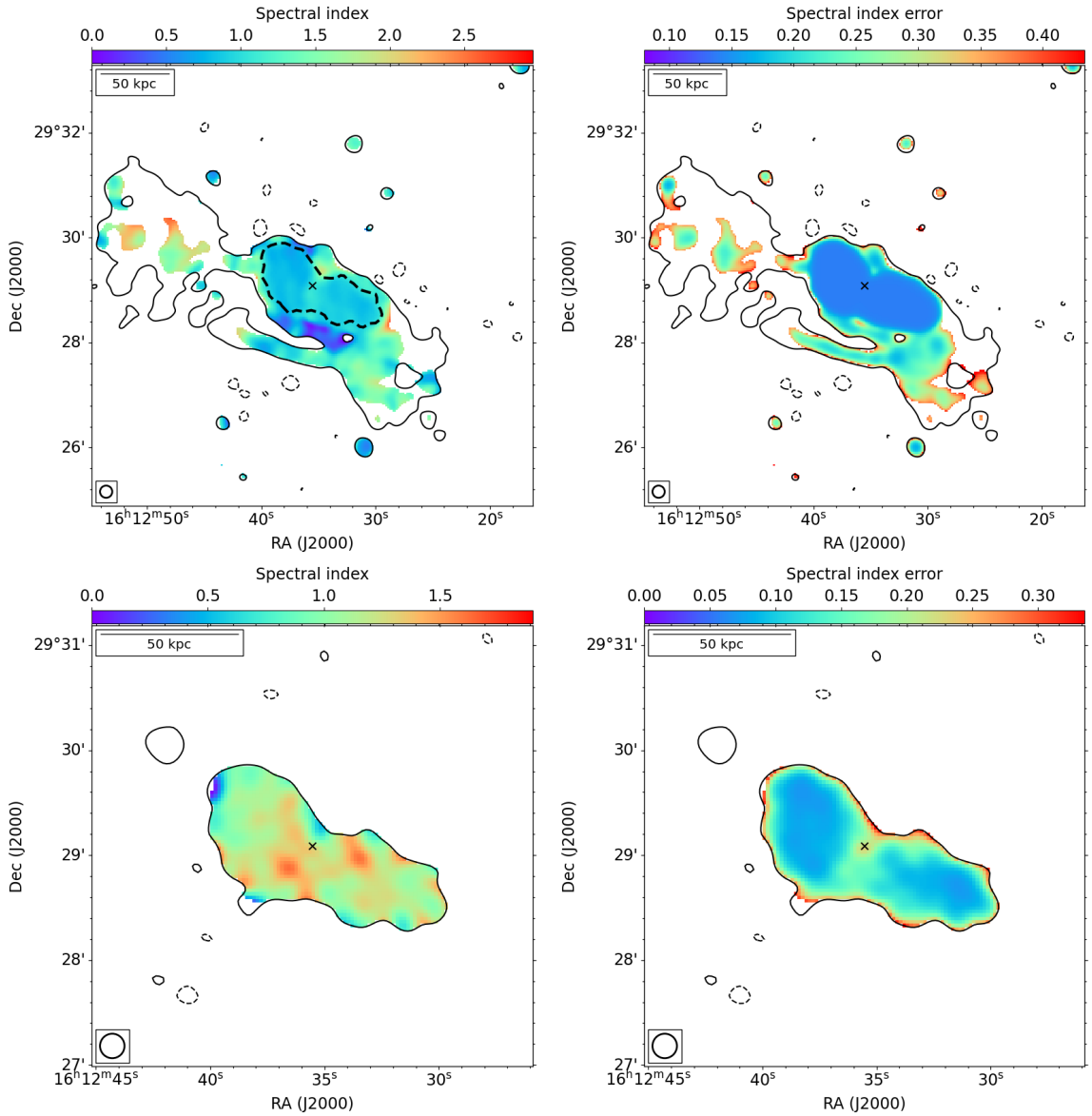

Figure 4.8: First row, left panel: NGC 6086 spectral index map between 144 MHz and 400 MHz at a resolution of 14", the black dotted line region is the 5000 MHz contour above 3σ and is used as a reference for the inner lobes. Right panel: the map shows the error value associated with the spectral index map. Contours show the LOFAR emission and are drawn at 3σ. Second row: NGC 6086 spectral index and error maps between 1400 MHz and 5000 MHz at a resolution of 14" with VLA 5000 MHz 3σ contours overlaid. The black '$\times$' marker is used to underline the location of the host galaxy. Beam is shown in the bottom-left corner and a reference scale is in the top-left one.

old AGN plasma accumulated under the influence of buoyancy combined with cluster/group weather and also compression by weak shock waves.
In NGC 6086, we have detected for the first time filaments that have emerged both from the southern and the northern side of the inner lobes. In particular, we distinguish clearly the two radio filaments on the southern side and a third filament on the

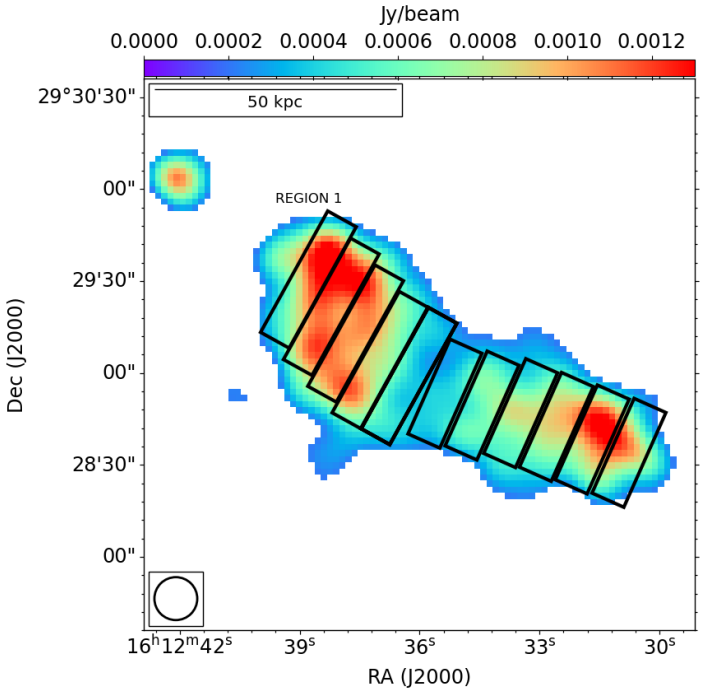

Figure 4.9: The image shows NGC 6086 at 14" resolution where all five frequencies are above the 3σ threshold. The eleven regions used for the spectral index analysis are overlaid. Beam is shown in the bottom-left corner and a reference scale in the top-left one.

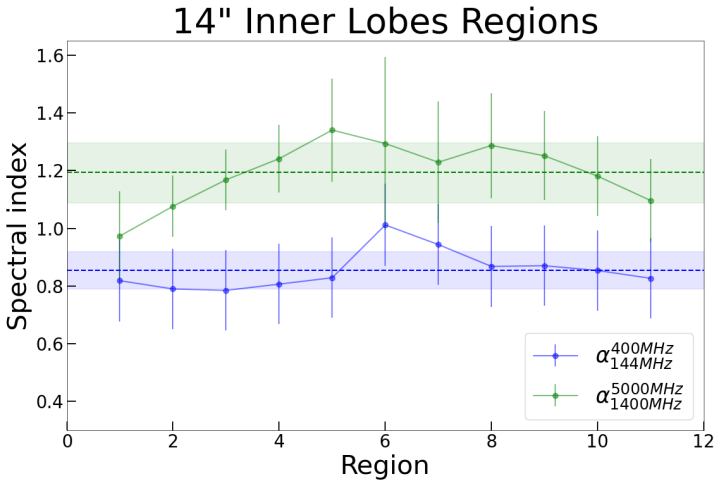

Figure 4.10: Radio spectral index profile across the lobes of NGC 6086 with 14" resolution at 144-400 MHz (blue line) and 1400-5000 MHz (green line). The dashed lines represent the mean values equal to 0.86 ± 0.07 and 1.19 ± 0.10 respectively. Coloured areas represent the standard deviation of the mean value.

northwest side. Projection effects have to be always taken into account since we can only investigate 2-D images, i.e. the northern filament could be superposed to the inner lobes emission in the west side. For clarity, we have labelled these three structures as

F1, F2 and F3 as shown in Fig. 4.11. With the data presented in this thesis, we can derive the integrated and resolved spectral index of these new filaments.
The filamentary structures are analysed with the highest resolution available of 7". To estimate the spectral index in these filaments, we have measured the flux density of F1, F2, and F3 inside a region above 3σ (where σ is the image RMS noise) for all three observations. In Table 4.4 we have listed the flux density values related to F1, F2, and F3 and the selected regions are shown in Fig.4.2. In Fig.4.11 are shown the linear best fit for the flux densities found. The slope of the best fit represents the spectral index, an alternative approach with respect to the Formula 1.8. It is clear that F1 and F3, despite the opposite location, have approximately the same spectral index value: $\alpha_{F1} = 1.14^{+0.13}_{-0.15}$ and $\alpha_{F3} = 1.19^{+0.11}_{-0.07}$ respectively. On the other hand, F2 has clear evidence of spectrum steepening and for this reason, we have considered the two points before the spectral break, resulting in a spectral index of $\alpha^{pre}_{F2} = 0.65^{+0.22}_{-0.22}$ and the two points after the break, where the spectral index is $\alpha^{post}_{F2} = 1.62^{+0.41}_{-0.41}$. The differences between F2 and F1/F3 are not clear, a possibility is that the two similar filaments are connected to a past common generation event or could be related to the same re-energising event, despite their opposite location with respect to the galaxy (in projection), but more informations are needed to prove that.

Region	$S_{144\ \mathrm{MHz}}$	$S_{400\ \mathrm{MHz}}$	$S_{675\ \mathrm{MHz}}$	α_{fit}
F1	7.81 ± 0.86	2.30 ± 0.26	1.36 ± 0.15	$1.14^{+0.13}_{-0.15}$
F2	6.63 ± 0.76	3.41 ± 0.36	1.46 ± 0.16	$0.65^{+0.22}_{-0.22}$
F3	4.78 ± 0.54	1.22 ± 0.14	0.78 ± 0.09	$1.19^{+0.11}_{-0.07}$

Table 4.4: Filament flux density (S) values inside the common regions for all three frequencies and the spectral index obtained from the best fit of the three flux densities.

For a more detailed analysis, we have generated a spectral index map at high-resolution and we have analysed the spectral index through the filamentary emission, in the same way as already done for the inner lobes with the datasets at 14" resolution. The spectral index map is shown in Fig. 4.12, alongside the error map, are generated using the 144 MHz and the 675 MHz images at 7" resolution. We have overlaid on the filaments the regions used to investigate the spectral index trends. The values inside the regions are plotted in Fig. 4.13, the regions are numbered from the east side to the west one. From the plot, we note that the F1 region has around 1.2±0.3 while the F2 regions have approximately the same mean value, but with a larger scatter around 1.0±0.4. Moreover, they both have a decreasing trend on the east side, but in the final three regions, they diverge a little. From these spectral index trends, we can hypothesise that they are formed under the same physical conditions and maybe at the same time. The third filament has an opposite trend with a comparable mean value of ∼1.1 but, as we mentioned before, the superimposition with the western lobe limits further spectral index investigation.

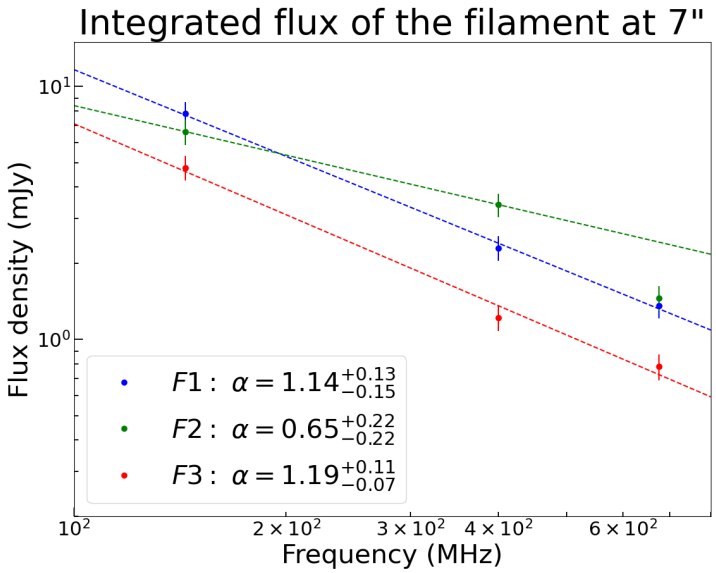

Figure 4.11: Linear best fit of the flux density value, colour information is visible in the bottom-left corner along with the spectral index value.

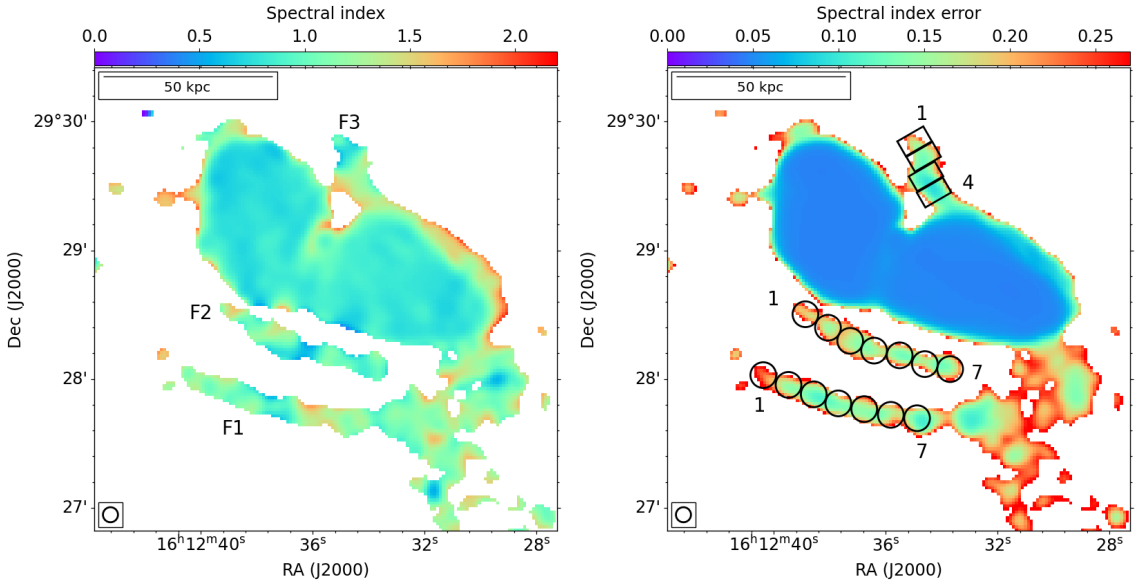

Figure 4.12: The image shows NGC 6086 spectral index and error map at 7" resolution with the black region used for the spectral analysis overlaid. The observations used to generate the map are the 144 MHz and the 675 MHz. Beam is shown in the bottom-left corner and a reference scale in the top-left one.

4.4.2 Low-resolution analysis

As presented in the right column of Fig. 4.2, the diffuse emission can be more effectively characterised with low-resolution images because we are more interested in the large-scale structure rather than the resolved smaller details. The LOFAR image at 144 MHz has detected more diffuse emission with respect to the higher frequencies,

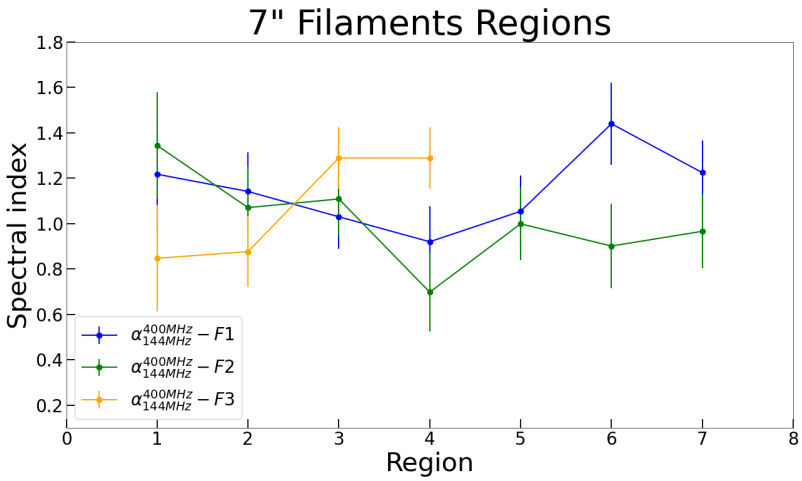

Figure 4.13: The plot shows the spectral index trend in the region of the filaments shown in Fig. 4.12. The region are numbered from east to west in all three filaments, the first and last number for each filament is highlighted in Fig. 4.12.

especially in the northern region. For the first time, we have 30" interferometric low-resolution images with high sensitivity, which show large-scale diffuse radio emission that broadens on much larger scales with respect to the previously known inner radio lobes. This emission exceeds the edges of the inner lobes in all directions. The most likely explanation is that these radio features are the remnants of past jet activities which are fading away and due to low surface brightness and spectral evolution they are not detectable at the GHz frequencies. The northern outer lobe is more extended with respect to the southern (especially in the 144 MHz image). The reason for the outer lobes asymmetries (at least in projection) could be the different expansion due to the not homogeneous IGrM and only future X-ray observations will improve our knowledge of the medium. To study the spectral index distribution throughout the two outer lobes, we have generated a pixel-to-pixel spectral index map as presented in this section. Moreover, in Chapter 5, we will derive first-order age estimates of the plasma with the help of the `BRATS` software.
For this analysis, we can use images at 144, 400 and 675 MHz because this emission is not detected in the GHz regime. For the spectral index analysis, we use two of the three frequencies to probe a broader frequency range. The 400 MHz regions above the 3σ threshold are much smaller than in the other two frequencies. To maximise the regions above the threshold, we decided to use the LOFAR 144 MHz and the uGMRT band-4 675 MHZ images to create the spectral index map of the source. The spectral index and error maps are shown in Fig. 4.14.

From the spectral index map, we can identify that the inner lobes region in the centre has almost a uniform value of around $\alpha_{144\mathrm{MHz}}^{675\mathrm{MHz}} \sim 0.8 - 0.9$, in perfect agreement to what has been found at higher resolution (see Sec. 4.3). This distribution suggests that lobes' electron populations have approximately the same age with a slight increase when they are closer to the host. On the other hand, we can see clearly that the diffuse emission has a steeper spectrum, with values that reach $\alpha_{144\mathrm{MHz}}^{675\mathrm{MHz}} \sim 2.2 - 1.3$

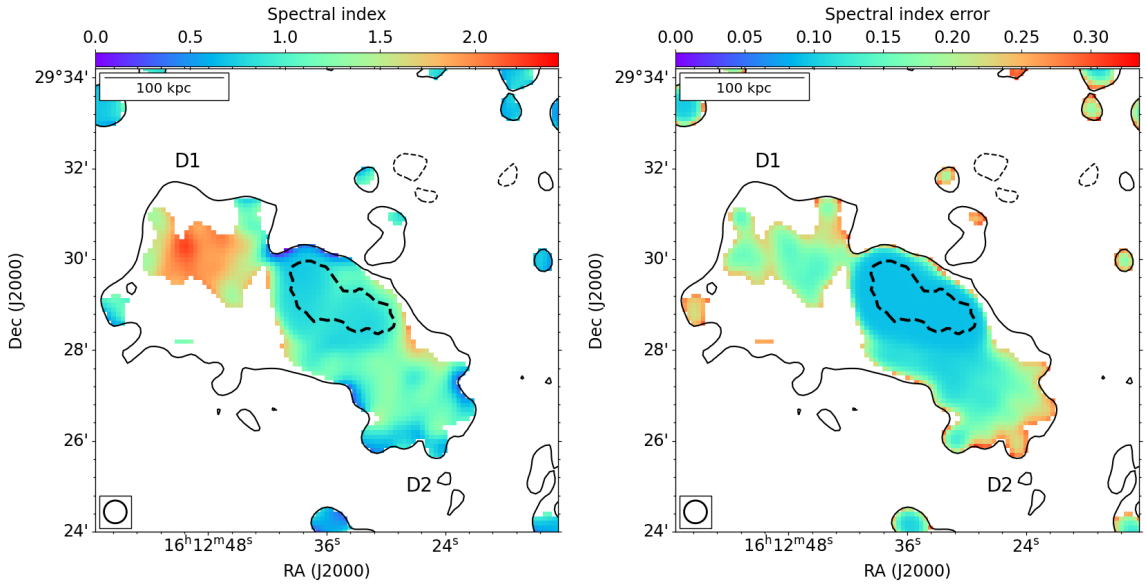

Figure 4.14: Left panel: NGC 6086 spectral index map between 144 MHz and 675 MHz at a resolution of 30". Right panel: the map shows the error value associated with the spectral index. Contours show the LOFAR emission and are drawn at (-3, 3)$\times\sigma$. The black dotted line is the inner lobes region, defined by the 3σ contour of the VLA 5000 MHz and used as a reference. Beam is shown in the bottom-left corner and a reference scale in the top-left one.

for the northern and the southern region respectively. This difference implies that the emission in the two regions D1 and D2 could be related to different AGN phases that happened in two different moments or that they are created in the same event but have undergone different evolution. For example, they could have interacted differently with the external medium (different compression/expansion) or magnetic field could be different. A very steep radio spectrum is what we expect from remnant AGN plasma created by past AGN activity, but the most interesting feature in these two outer lobes is the absence of a clear steepening gradient. In fact, in D1 we have a spectral index peak surrounded by lower values and for D2 the distribution seems more uniform with less spectral index variation, but with some patchy zones. The error map shows an almost uniform 10% error value.

We have then performed the same analysis made for the lobes in Sec. 4.3. We have selected fourteen regions from the east (region 1) to the west (region 14) (see Fig. 4.15) and estimated the spectral index from the flux densities measured at 144 MHz and 675 MHz. All the regions are larger than the beam size. With this analysis, we aim to characterise how α varies along the whole diffuse emission in order to have representative integrated values other than the spectral index map.
The spectral index trends are shown in Fig. 4.16, from east to west, with the colour associated with the three different parts of the target. The D1 and D2 regions have higher spectral index values than the lobes, as previously found in the spectral index map (see Fig. 4.14), with integrated values around 1.75 and 1.1, while the target inner lobes confirm a constant value around 0.8.
From this plot, we see an opposite behaviour in the spectral index trend of the outer

lobes, with a flattening in the eastern region and a steepening in the western one by moving towards the inner lobes.

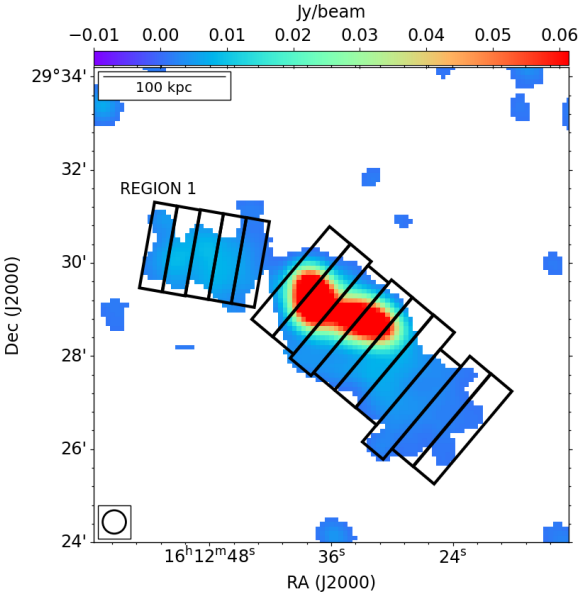

Figure 4.15: NGC 6086 at a resolution of 30" where data are above 3σ level both from LOFAR 144 MHz and uGMRT 675 MHz. In the map are selected fourteen regions through all the emission to measure the spectral index gradient. Beam is shown in the bottom-left corner and a reference scale in the top-left one.

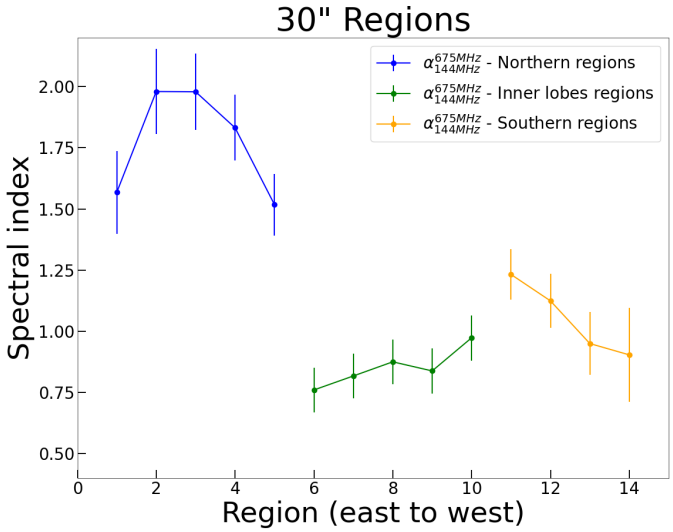

Figure 4.16: $\alpha_{144\mathrm{MHz}}^{675\mathrm{MHz}}$ value for the fourteen regions chosen are plotted in order to see differences in the target components, we see clearly a highest steepening in the east diffuse region than in the west one and the lobes confirm their slope already found in other maps.

In Fig. 4.17 we show the 30" resolution image at 144 MHz with a threshold above 3σ for both the 144 MHz and for the 675 MHz observation. We added a polygonal

region located under the northern outer lobe and with the 3σ contours of the LOFAR 144 MHz observation at 30". This region has been investigated to give a constraint on the spectral index in a region that is detected only at 144 MHz. For this estimate we have used two points: the first is the flux density inside the selected region for the 144 MHz observation and the second is the value of two times the noise of the 675 MHz observation multiplied by the number of beams inside the same region. The result is a conservative upper limit and the value of the spectral index is $\alpha_{upper} \geq 1.56$.

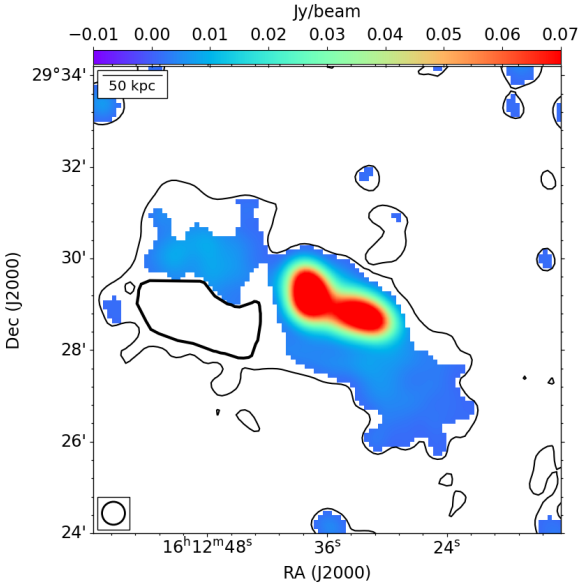

Figure 4.17: NGC 6086 at 30" resolution at 144 MHz with a threshold above 3σ both for the 144 MHz and for the 675 MHz observation. We have overlaid the LOFAR contours at 3σ and a polygonal region where the upper limit of the spectral index is estimated.

Chapter 5

Spectral age analysis

The evolution of the synchrotron spectrum is dictated by the amount of radiative losses that the particles have experienced and it is directly related to the age of the plasma. As shown in Sec. 1.4, the synchrotron age depends on the magnetic field, redshift and break frequency. The lifetime analytic equation (Formula 1.9) is used in the historical approach for spectral break measurements and gives a first-order age value, but a more accurate analysis can be done by using the integration of radiative cooling equations. For this second approach, we used the Broadband Radio Astronomy Tools (`BRATS`) software (Harwood et al. [2018]. `BRATS` can be used to fit the observed radio spectra in each pixel with a modelled spectrum and thus to create spectral age maps.
The model used for the analysis of NGC 6086 is called the Jaffe-Perola model (or JP model, Jaffe and Perola [1973]) and the assumptions are: the electrons are accelerated in a single event at an initial time t=0 with an energy distribution equal to $N(E,t) = N_0 E^p$ and the magnetic field is uniform across the source. This model is similar to the Kardashev-Pacholczyk model (or KP model, Kardashev [1962]), but while this last one considers the pitch angle of the electron as a constant, the JP model assumes a more realistic situation, where single particles are subject to many scattering events that randomise their pitch angles. This different assumption naturally leads to differences in the spectrum curvature. For a given age, the KP model is relatively flatter than its JP counterpart at high frequencies. Another category of models assumes the continuous injection of particles, resulting in the sum of multiple single-injection models and they are usually used for fitting integrated spectra. The CI (continuous injection) and the CIOFF (continuous injection OFF) are two examples. The CIOFF is a continuous injection model like the CI, but it assumes that the source accelerates new particles for a limited amount of time. After the active period, the spectral evolution continues passively. This model represents the typical evolution of the integrated spectrum of a remnant radio galaxy.

5.1 The colour-colour diagram

The colour-colour diagram is used to investigate the spectral shape of the plasma by plotting spectral index values of different regions of the source and representative evolutionary models, it was presented for the first time by Katz-Stone et al. [1993]. This

is a plot of a spectral index versus another spectral index, in two different frequency range. In particular, if the spectral index does not change between the two frequency ranges, the values will follow the bisector of the diagram because all the points have $\alpha_1 = \alpha_2$. On the other hand, if we look at an aged spectrum, before and after the spectral break, the data will follow different trajectories than the bisector line. The models try to reproduce the evolution of the spectrum with different assumptions, for instance, they could assume a single or a continuous injection of new particles in the plasma or different physical assumptions. Spectrum evolution implies also a spectral index evolution and the colour-colour diagram is used to investigate it. We plot the value and look at which model best reproduces the data.
We have made a colour-colour diagram (Fig. 5.1) to investigate the spectral index evolution of the inner lobes at 14" resolution. The coordinates of the plot are two spectral index: $\alpha^{400\mathrm{MHz}}_{144\mathrm{MHz}}$ in the x-axis and $\alpha^{5000\mathrm{MHz}}_{1400\mathrm{MHz}}$ in the y-axis. The spectral index values reported in the diagram are measured in the eleven regions shown in Fig. 4.9. We have plotted the Jaffe-Perola model (or JP model, Jaffe and Perola [1973]) and the Continuous Injection Off model (or CIOFF model).
The black dotted line is the diagram bisector and represents $\alpha^{400\mathrm{MHz}}_{144\mathrm{MHz}} = \alpha^{5000\mathrm{MHz}}_{1400\mathrm{MHz}}$; the red line is the JP model with the equipartition magnetic field value, the green line is the CIOFF model. Despite the large error bars, all the points are below the bisector line (grey dotted line), which means that all the regions have a steeper spectral index after the spectral break, as expected. It is clear that the single injection model is not a good representation of the data because the model assumptions are not representative of the evolution of the system. On the other hand, the CIOFF model represents the data better. The JP model is used when the analysis is made on small regions because the electrons are assumed to have the same age, while the CIOFF model is used in integrated analysis on larger regions, where the single injection index is not representative of all the populations.

5.2 Injection index and magnetic field

Before creating the age map, we need to set the magnetic field and injection index. The injection index is estimated by using the `findinject` task. This performs the model fitting of the source pixel-by-pixel radio spectrum using a range of spectral indices given in input and, for every iteration, it returns the chi-squared value of the fit. The injection index value that minimises the chi-squared is $\alpha_{inj} = 0.60$, so this value is used for the following analysis.
We assumed the equipartition value as a good estimate for the magnetic field of this source (derived as presented in Sec. 1.5). For the $\mathrm{B_{eq}}$ estimate, we followed Murgia et al. [2012] whose formula is:

$$B_{eq} = \left[\frac{4\pi m_e c^2 (1+\alpha)(1+k)\nu^{\alpha} L_{\nu} (\gamma_{max}^{1-2\alpha} - \gamma_{min}^{1-2\alpha})}{(C_{\alpha})_{LOS}(1-2\alpha)V} \right]^{1/(3+\alpha)} \tag{5.1}$$

where γ values are the Lorents factors range of the electron population, assumed as $\gamma_{max} = 10^6$ and $\gamma_{min} = 10^2$; m_e is the electron mass; $\alpha = 0.6$ is the injection index found with the model fitting in BRATS; $k = 0$ is used assuming positron as positive

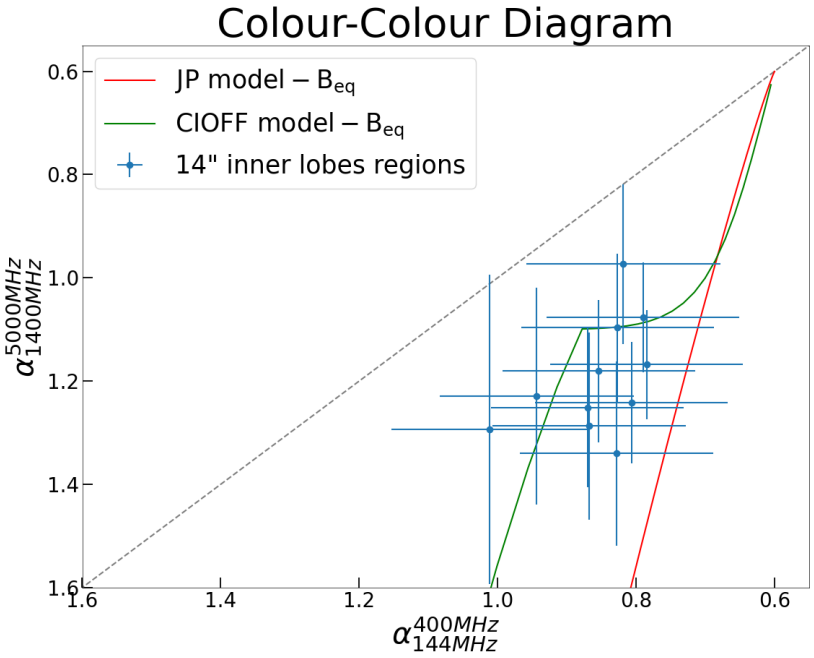

Figure 5.1: The colour-colour diagram of the selected eleven regions showing the spectral shape of the plasma, the dotted grey line represents the same value for both spectral indexes. The red line represent the evolution expected for a JP model with $\alpha = 0.6$ and $B_{eq} = 4.44$ μG, which is the injection index reported in Sec. 5.2. The green line is the evolution expected for a CIOFF model with the same α and magnetic field.

charges and $z = 0.0318$ is the redshift. The volume of the inner lobes has been modelled as two ellipsoids with the third axis length equal to the shorter one.
The result of the equation is $B_{eq} = 4.44$ μG.
We have also performed a lower magnetic field estimate, calculated as:

$$B_{min} = \frac{B_{CMB}}{\sqrt{3}} = \frac{3.25(1+z)^2}{\sqrt{3}} \tag{5.2}$$

which corresponds to the minimum radiative losses allowed for the plasma at a given redshift. With this magnetic field, the spectrum of the plasma will get steeper more slowly than with the equipartition value. The minimum magnetic field is a lower limit of this value and, for this reason, it is useful because provides an upper limit to the spectral age values. On the other hand, the equipartition value is a better estimates of the field and it is the value commonly used for the further analysis (i.e. also Shulevski et al. [2017] and Brienza et al. [2022] used the equipartition assumption).

5.3 Spectral age maps

5.3.1 Inner lobes

The spectral age map is a pixel-to-pixel age estimate. It is generated by assuming a magnetic field value, an injection index value and a model for particle ageing. For the map creation, we need the highest number of available frequencies, in order to trace the spectral curvature as better as possible. For this reason, we have used the five images at a 14" resolution, with a frequency range from 144 MHz and 5000 MHz. We investigate the plasma age in all pixels above 3σ for all five images, corresponding to the inner lobe region. We have used the JP single injection model because we assume (to first order) that all the electrons in a single pixel are accelerated by the same event and at the same time. The fitting results are shown in Table 5.1.
In the final spectral age map, every pixel value is the result of the spectral fit in that single point. One representative good spectral fit (flux density versus frequency) for an individual pixel is shown in Fig. 5.3.
In Fig. 5.2 we have shown the spectral age maps and the correspondent error maps of NGC 6086 at 14" using all five frequencies available when the data are fitted with the JP model. We show the results obtained using the equipartition magnetic field value of $B_{eq} = 4.44$ μG in the first row of the figure. We show the same plots in the second row, but in this case, we have used the minimum value of $B_{min} = 2.00$ μG. It is clear that the magnetic field does not change the age distribution, but it increases in every pixel the age value because of the lower particle energy losses.

Model	B	Mean χ^2_{red}	Confidence Bins					Rejected	Median
	μG		<68	68-90	90-95	95-99	≥99		confidence
JP	4.44	1.71	891	423	126	137	195	No	<68
JP	2.00	1.71	887	426	127	135	197	No	<68

Table 5.1: Data of the JP model applied to the inner lobes of the five images at 14" resolution. The injection index is $\alpha = 0.6$ in both cases.

In the spectral age maps, we can find anomalous pixel values, especially in the near edges. They are artefacts caused by flux values that are very close to the threshold value, resulting in anomalous spectral indices and ages. For this reason, we have excluded them from our analysis.
From the spectral age map generated using B_{eq}, we can see that the youngest populations are located near the edges of the lobes, with values of 35 Myr, while the oldest population resides in the central part with 55 Myr. This means that the source has been switched off for, at least, the last 35 Myr and the last episode of jet activity, which inflated the inner lobes, lasted approximately 20 Myr.
We obtain the same trends from the map with B_{min} because the magnetic field does not change the evolution of the particles. On the other hand, a lower value of the field implies that the spectrum has a slower evolution and the populations have higher ages, as expected when we have lower energy losses. With the B_{min} magnetic field, we obtain that the youngest populations at the edges of the source are 45 Myr old

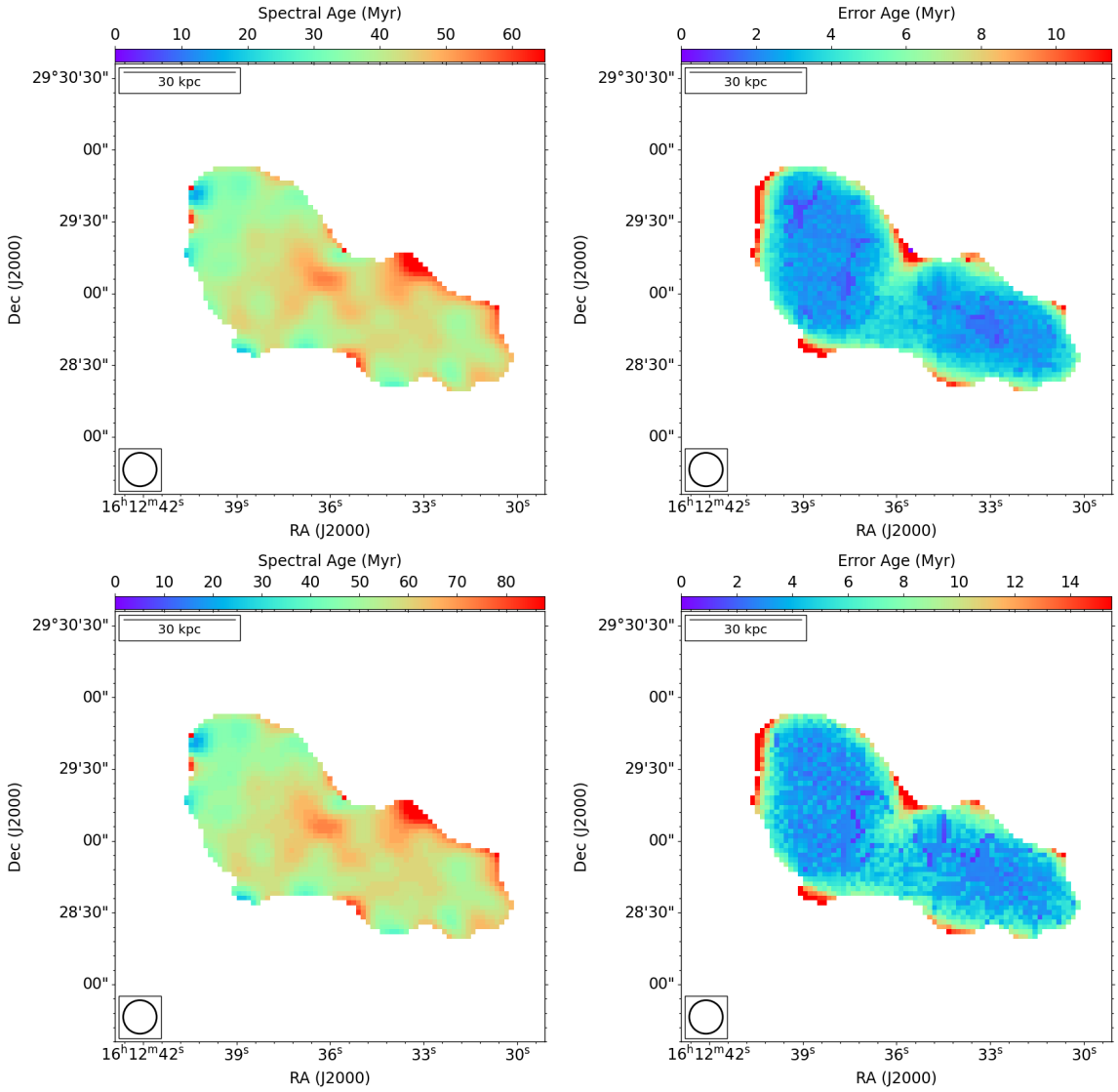

Figure 5.2: Left panel: NGC 6086 spectral age map using the JP model at a resolution of 14". Right panel: the map shows the error value associated with the ages. The first row is the age map resulting by using the magnetic field equipartition value 4.44 μG while the second row by using the minimum magnetic field value 2.00 μG. Beam is shown in the bottom-left corner and a reference scale in the top-left one.

while the oldest population in the central part have almost 85 Myr. The duty cycle has doubled its periods of activity/inactivity.

5.3.2 Outer lobes

The outer lobes are detected only by the three frequencies below 1 GHz, for this reason, we cannot generate the spectral map as done for the inner lobes. We can make a first-order age estimate by generating a series of simulated JP model with a selected

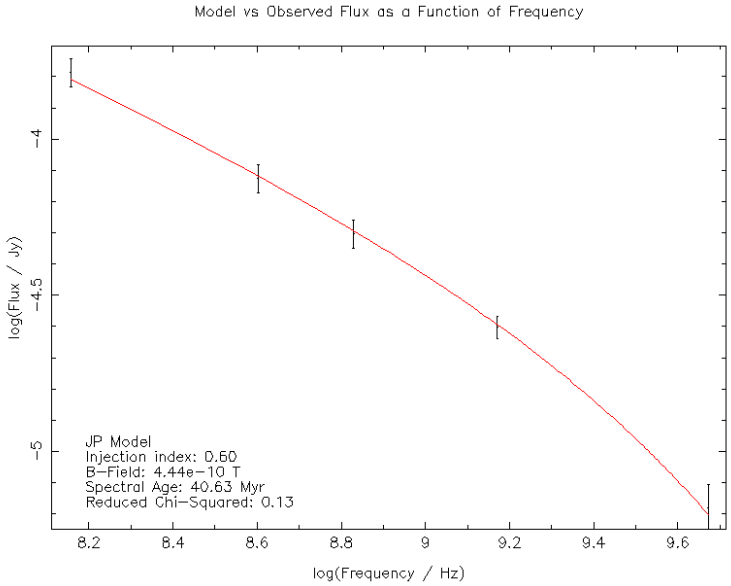

Figure 5.3: Representative radio spectrum (flux density vs. frequency) for an individual pixel with a good fitting result. Black points are observational data, and the red solid line is the best fit using the JP model. Model parameters, ages (in Myr), and statistics are shown in the bottom left corner of the panel.

injection index, magnetic field and frequency range. From these models, we compared the generated spectral indices with the values found in the spectral index map (see Fig. 4.14). For this estimate, we set the injection index $\alpha = 0.6$, magnetic field $B_{eq} = 4.44$ μG or $B_{min} = 2.00$ μG and we select 144 MHz and 675 MHz as frequencies. We generate a series of spectra for each time bin. We are interested in the flux densities at the chosen frequencies, which evolve over time following the JP model spectral evolution. From this list, we can derive a list of spectral indices that steepen over time. From the outer lobe age estimate using B_{eq}, we derive that the active period of the northern outer lobe started 210 Myr ago and lasted 90 Myr, while the southern lobe started its active phase 130 Myr ago and this phase lasted 65 Myr. As we have seen with the inner lobes, the age vales increase a lot with the minimum magnetic field with the B_{min} magnetic field, in particular, we obtain that the northern lobe experienced an active phase between 282 Myr and 160 Myr ago, while the southern lobe had an active phase between 188 Myr and 102 Myr ago.
A summary of the age estimates is presented in Table 5.2, in order to have a more clear view of the system duty cycle.

The spectral age values reported in Table 5.2 present remarkable differences between the two outer lobes, as a consequence of the gap between the spectral index values. In particular, the D1 outer lobe seems to be a factor 1.6-1.7 older than the other one. This difference could be explained in different ways, as discussed below: they can be in different environments that lead to different expansion; the different magnetic fields could lead to different energy loss rates. It is hard to find the real cause, especially without X-ray observations that help to investigate the dynamics and interaction with the surrounding medium. We can just make some considerations and hypotheses that

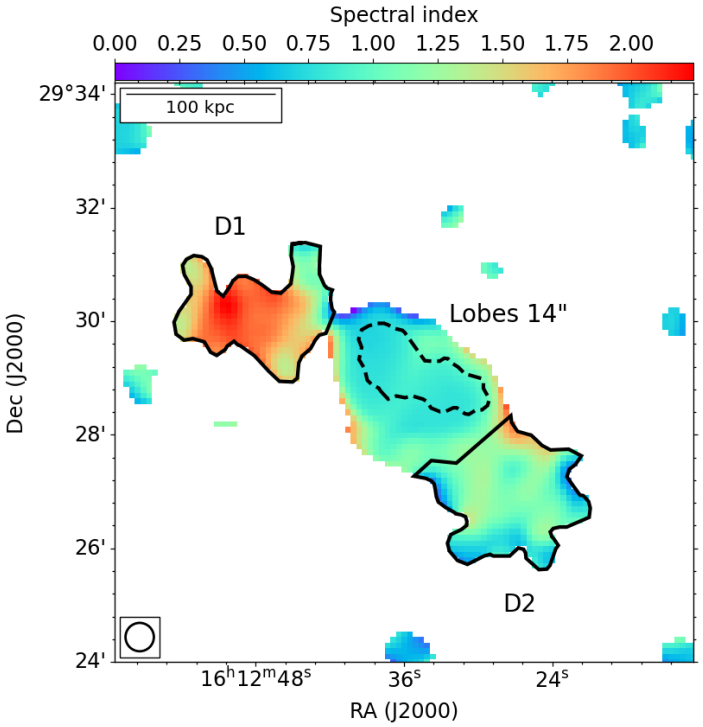

Figure 5.4: Spectral index map between 144-675 MHz at 30" of NGC 6086 with overlaid the two diffuse emission regions used to investigate the spectral index and the 14" lobes region used for the lobes analysis. Beam is shown in the bottom-left corner and a reference scale in the top-left one.

Region	α_{min}	α_{max}	B_{eq}		B_{min}	
			Min age [Myr]	Max age [Myr]	Min age [Myr]	Max age [Myr]
Lobes	0.8	1.0	35	55	45	85
D1	1.2	2.2	120	210	160	282
D2	0.9	1.3	75	130	102	188

Table 5.2: Spectral index measured at 144-675 MHz and 30" resolution in the diffuse region of NGC 6086, shown in Fig. 5.4 and the age estimate using the JP model both with B_{eq} and B_{min}.

have to be further investigated in the future.
We considered it unlikely that the lobes are made by different AGN active phases because of the comparable size and shape of the regions (at least in projection). For these reasons, we assume that the age discrepancies are due to a different evolution of the outer lobes, but generated in the same AGN outburst.
As presented in Sec. 1.4, the magnetic field strength is a fundamental value in the synchrotron spectral evolution, but it is very hard to give an estimate of its value. There are few methods that give a value estimate, such as the equipartition that we have used in this thesis, but they take advantage of some assumptions. Another assumption is to assume the same equipartition value for the inner and outer lobes. Moreover, the outer lobes could have different magnetic field strengths and assuming

them equal to the equipartition value could be the reason for the age discrepancy. To obtain the same age for the D1 and D2 lobes, we investigated the spectral evolution by using the JP model with different values of the magnetic field. We have assumed that D2 has the same magnetic field as the inner lobes, while D1 has a higher value. The results are reported in Table 5.3. To obtain the same age in the outer lobes, a difference in the magnetic field of almost a factor of two is needed.

Outer lobe	B [μG]	α_{min}	α_{max}	Min Age [Myr]	Max Age [Myr]
D1	7.00	1.2	2.2	75	135
D2	4.44	0.9	1.3	75	130

Table 5.3: Magnetic field value difference in the outer lobes in order to obtain the same spectral age.

5.4 Jet duty cycle

By combining the age estimates presented in the previous sections we can derive the duty cycle of the jets in NGC6086. We have detected the last two events of jet activity: using the equipartition magnetic field of $B_{min} = 4.44$ μG, we find that the first phase of activity happened around 170 Myr ago and lasted ∼70 Myr; while the second one started after ∼45 Myr of AGN quiescent phase and lasted 20 Myr. In the last 35 Myr, NGC 6086 has not experienced another active phase. We also considered a more conservative magnetic field value equal to $B_{min} = 2.00$ μG. In this case the first active phase started 250 Myr ago and lasted ∼ 110 Myr and, after a quiescent phase of 65 Myr, the second active phase started and lasted 40 Myr. In this scenario, the current quiescent phase has started 45 Myr ago.
We note that these estimates are a first approximations and they do not take into account physical effects, such as the compression or expansion and the magnetic field variations.
All the timescales relative to the jet activity are summarised in Table 5.4. We can consider the B_{min} as a lower limit for the magnetic field which implies an upper limit for the age results. Although the equipartition value is the result of few assumptions, it is reasonable to think that the real age of the active and inactive phases is located inside the age range derived with the two magnetic field values used.

To have a more clear representation, we have reported the mean age values between D1 and D2 regions. When we have used the values obtained assuming B_{eq}, the duty cycle is about a third shorter than using the other value of the magnetic field.
We have investigated the fractional active time of the source since the first active phase by measuring $A.t. = \Delta t_{on}/(\Delta t_{on} + \Delta t_{off})$. In the active time are taken into account the two active phases, while in the inactive time we have considered the two quiescent periods (between the active phases and between the second phase and now), the activity is measured for both the magnetic field:

$$\text{Active time}(\mathrm{B_{eq}}) = \frac{\mathrm{t_{on}}}{\mathrm{t_{on}} + \mathrm{t_{off}}} = \frac{(20+70)_{\mathrm{on}}}{(20+70)_{\mathrm{on}} + (35+45)_{\mathrm{off}}} = 53\% \qquad (5.3)$$

Phase	B_{eq}		B_{min}	
	Age range [Myr (ago)]	Δt [Myr]	Age range [Myr (ago)]	Δt [Myr]
First active	100-170	70	140-250	110
Inactive	55-100	45	85-140	65
Second active	35-55	20	85-45	40

Table 5.4: Duty cycle time-scales estimated using spectral age results, obtained using the JP model on the lobes and the diffuse emission regions. The age estimate is presented as divided between the two magnetic field values and the ages are expressed in Myr looking back. Δt represents how the phase lasts.

$$\text{Active time}(\mathrm{B_{min}}) = \frac{\mathrm{t_{on}}}{\mathrm{t_{on}} + \mathrm{t_{off}}} = \frac{(40+110)_{\mathrm{on}}}{(40+110)_{\mathrm{on}} + (45+65)_{\mathrm{off}}} = 58\% \tag{5.4}$$

We found an active time of 53% and 58% for the B_{eq} and for the B_{min} respectively. This result shows that the active time has a small correlation with the magnetic field used for the analysis, in fact, the active time varies by only 5% with an increase in the magnetic field by a factor larger than two.

Despite there are only few cases of duty cycle analysis in radio galaxies with multiple active phases, the derived duty cycles and active time periods are consistent with the results found in other studies of radio galaxy, such as: B2 0924+39 (see Shulevski et al. [2017]) in which they found an active time of $\sim$ 66% with a resolved analysis of the radio emission; the restarted radio galaxy 3C388 (see Brienza et al. [2020]) in which they found an active time of $\gtrsim$ 60% and also in MS 0.735.6+7421 (see Biava et al. [2021]) is found a very rapid cycle with brief quiescent phases.

Chapter 6

Summary and conclusions

In this thesis, we have presented the study of the radio galaxy B2 1610+29, associated with the galaxy NGC 6086, located at the centre of the galaxy group Abell 2162. The source shows diffuse emission detectable in the radio band and it is classified as a remnant radio galaxy. NGC 6086 has been studied by several authors (Giacintucci et al. [2007], Liuzzo et al. [2010], Murgia et al. [2011]) and they all described the source as a remnant (or dying), double lobe radio galaxy without an active core. Thanks to the new generation of low-frequency interferometers (i.e. LOFAR and uGMRT), we have confirmed this view, but we are also able to perform resolved studies to derive accurate spectral ages. Thanks to these new detection, we made major steps forward in the analysis of the source and we improved our knowledge of its evolution. These observations allowed us to investigate new diffuse and filamentary emission, previously undetected. In particular, the diffuse emission has highlighted a second pair of lobes, probably addressable to a previous AGN active phase, labelled as outer lobes.
We performed the data calibration of two VLA archival datasets at 1.4 GHz, in B and C configurations. Our integrated analysis of the inner lobes is consistent within the errors with the one made by Murgia et al. [2011]. We combined them to obtain an image at 7" and 14" resolution (with a physical scale of 0.635 kpc/"). For a better analysis of the inner lobes spectrum, we added a 5.0 GHz observation at 14" made with the VLA. Then, we added three new low-frequency images centred at 144 MHz, 400 MHz and 675 MHz respectively and each of them has been imaged at 7", 14", and 30" resolution.

Our main results of the analysis of NGC 6086 are reported below:

- We investigated the inner lobes of the source with five images at 14" resolution. We have found that the synchrotron spectral break is located between 1.4 GHz and 5.0 GHz by performing the integrated analysis of the inner lobes. This result improved our knowledge of the shape of the radio emission spectrum. In addition, we performed for the first time a resolved spectral analysis of the inner lobes in a frequency range located at frequencies lower than the spectral break. No clear spectral index trend across the inner lobes has been found, the only feature is a light steepening of the spectrum in the central region, where the host galaxy is located. As a consequence of the long quiescent phase, the features commonly used for the Fanaroff-Riley classification are not clearly recognisable and the spectral index distribution has roughly the same value throughout the

inner lobs. We supposed the FR II nature of the source because of the spectral index steepening in the central part.
We used the BRATS software to perform a resolved spectral ageing analysis of the lobes' electron populations, which consists of a pixel-to-pixel model fitting of the flux density values. To proceed with the analysis, we had to assume the value of the injection index, the magnetic field value and a spectral evolution model. We chose the single-injection JP model because we applied it to every single pixel, in which we assumed that all the particles are accelerated by the same event. The injection index value is derived by performing a model fitting of our data and we used the value with the lower chi-squared which is $\alpha_{inj} = 0.6$; lastly, we chose to generate two maps with different magnetic field values. The first value used is the equipartition magnetic field. The second value corresponds to the lowest synchrotron energy losses and is defined as $B_{min} = B_{CMB}/\sqrt{3}$, the consequence of this lower value is an increase of the total ages.
From the spectral ageing analysis, we derived that the last active phase which inflates the inner lobes happened: between 35 and 55 Myr ago with B_{eq}; between 45 and 85 Myr ago with B_{min}.

- We have used the three low-resolution and low-frequency images to explore the diffuse emission that emerged at higher distances from the galaxy. In particular, the 144 MHz observation shows a large quantity of diffuse emission which decreases in the other two frequencies. With the new datasets, we have detected for the first time two diffuse emission regions with a shape that can be associated to an older active phase of the radio galaxy. We labelled these regions as the outer lobes and their analysis provided more information on the duty cycle of NGC 6086. We generated the spectral index map, as already done for the other emission regions, and we noticed that the northern outer lobe reaches higher spectral index values than its southern counterpart. Furthermore, the integrated analysis showed us that the outer lobes have an opposite spectral index trend as they move toward the host galaxy. These differences in the outer lobes synchrotron spectrum could be explained in different ways. In particular, we think it is unlikely that they are two different active phases because of their approximately similar shapes, sizes and distances from the galaxy. Moreover, it is unlikely that two subsequent active phases generate a single jet in two opposite direction, extremely aligned as we see in the outer lobes morphology. A more realistic scenario for the observed differences is that the outer lobes undergo a different evolution, in which the environment (i.e. adiabatic expansion or compression) or the magnetic field strength play a fundamental role. We have measured that with a magnetic field of only 3.5 μG more than the equipartition value, the value of the spectral indices in the outer lobes becomes the same.
  We analysed the age of the outer lobes with the same assumptions used for the inner ones: JP model, $\alpha_{inj} = 0.6$; B_{eq} and B_{min} for the values of the magnetic field already used. We are not able to perform a pixel-to-pixel model fitting because this emission is detected at three frequencies only and it is a small number for reliable fitting results. For this reason, we did not perform a complete spectral analysis but we used the observed spectral index to obtain a first-order estimate

of the age. As expected, the northern outer lobe is more aged than the southern one and it was injected between 120 and 210 Myr ago with the B_{eq} value and between 160 and 282 with the B_{min}. The southern outer lobe was injected between 75 and 130 Myr ago with B_{eq} and between 102 and 188 Myr ago with B_{min}.

- We assumed an average age value of the outer lobes to give constraints on the duty cycle of the source. With the equipartition assumption, the duty cycle is characterised by a first active phase that started 170 Myr ago and lasted 70 Myr; between the active phases there are 45 Myr of quiescent phase; finally, a second active phase that turned on 55 Myr ago and lasted 20 Myr. With the minimum magnetic field assumption, the cycle is longer and characterised by a first active phase that lasted 110 Myr and started 250 Myr ago; a 65 Myr quiescent phase; a second active phase that lasted 40 Myr and started 85 Myr ago. The total active time of the source with B_{eq} or B_{min} is 53% and 58%, respectively.

- The three high-resolution and low-frequency images have shown the presence of new multiple filamentary structures, previously undetected in NGC 6086. We have analysed the integrated flux densities and spectral index trends, in order to achieve information about their origin and evolution. This peculiar diffuse emission has been observed in other structures (i.e. NGC 507, Nest 200047, 3C40A-3C40B) thanks to the new high-sensitivity and high-resolution observations. Several hypotheses have been proposed in the literature to explain the filamentary emissions, but without an accurate magnetic field estimate and X-ray observations, it is very hard to understand the dynamics and evolution of these structures. We noticed that the northern filament could be partially superimposed (in projection) to the western inner lobe, making its characterisation even more complicated than the others. It is hard to associate the filaments to what originated them, a possible explanation is an enhancement of the magnetic field intensity in these regions, which ends up in an increase in the emissivity. Another explanation is that the compression of the filament regions enhanced the emissivity. The absence of clear spectral index trends makes the analysis even more complicated. As mentioned before, future high-energy observation could provide more information on the dynamics around these structures and find out how they have been originated.

Without high-energy observation, we are not able to derive solid conclusions on the dynamics of the gas in the environment of NGC 6086. To date, we can not prove how the AGN plasma interacts with the surrounding medium. For example, Brienza et al. [2022] found a spiral morphology of the X-ray emission of NGC 507, suggesting sloshing that induced gas motion on larger scales. Moreover, X-ray studies could find cavities inflated by the radio jets, as found by Biava et al. [2021] in MS 0735.6+7421, which could give us reliable information about the energy of the system and the jet power needed to inflate those cavities. These kinds of studies are also important to characterise the heating of the central gas and so to prevent it from cooling.
Further investigation with highly-sensitive observation at low-frequencies (i.e. LOFAR

Low Band Antennas, LOFAR 2.0 and, in the near future, the Square Kilometre Array) and high-energy observation in the X-ray band will be ideal for gaining a more detailed investigation of older diffuse radio emission in the system, its duty cycle, filaments and magnetic field. Thanks to the new radio interferometers, galaxy groups like Abell 2162 are receiving increasing attention. This kind of spectral study will be very important to achieve new knowledge on the diffuse emission in radio galaxies, on the duty cycles of the AGN and on the interaction between the emission of the galaxies and the environment of the group.

Bibliography

S. Ananthakrishnan. The Giant Meterwave Radio Telescope / GMRT. *Journal of Astrophysics and Astronomy Supplement*, 16:427, Jan. 1995. URL https://ui.adsabs.harvard.edu/abs/1995JApAS..16..427A. Provided by the SAO/NASA Astrophysics Data System.

R. R. J. Antonucci and J. S. Miller. Spectropolarimetry and the nature of NGC 1068. *The Astrophysical Journal*, 297:621–632, Oct. 1985. doi: 10.1086/163559. URL https://ui.adsabs.harvard.edu/abs/1985ApJ...297..621A. Provided by the SAO/NASA Astrophysics Data System.

J. N. Bahcall, S. Kirhakos, D. H. Saxe, and D. P. Schneider. Hubble Space Telescope Images of a Sample of 20 Nearby Luminous Quasars. *The Astrophysical Journal*, 479 (2):642–658, Apr. 1997. doi: 10.1086/303926. URL https://ui.adsabs.harvard.edu/abs/1997ApJ...479..642B. Provided by the SAO/NASA Astrophysics Data System.

P. Baldini. *Emissione di Bremsstrahlung e applicazioni astrofisiche*. PhD thesis, 2020. URL http://amslaurea.unibo.it/22210/.

S. A. Baum, E. L. Zirbel, and C. P. O'Dea. Toward Understanding the Fanaroff-Riley Dichotomy in Radio Source Morphology and Power. *The Astrophysical Journal*, 451: 88, Sept. 1995. doi: 10.1086/176202. URL https://ui.adsabs.harvard.edu/abs/1995ApJ...451...88B. Provided by the SAO/NASA Astrophysics Data System.

V. Beckmann and C. R. Shrader. *Active Galactic Nuclei*. 2012. URL https://ui.adsabs.harvard.edu/abs/2012agn..book.....B. Provided by the SAO/NASA Astrophysics Data System.

P. N. Best, C. R. Kaiser, T. M. Heckman, and G. Kauffmann. AGN-controlled cooling in elliptical galaxies. *Monthly Notices of the RAS*, 368(1):L67–L71, May 2006. doi: 10.1111/j.1745-3933.2006.00159.x. URL https://ui.adsabs.harvard.edu/abs/2006MNRAS.368L..67B. Provided by the SAO/NASA Astrophysics Data System.

N. Biava, M. Brienza, A. Bonafede, M. Gitti, E. Bonnassieux, J. Harwood, A. C. Edge, C. J. Riseley, and A. Vantyghem. Constraining the AGN duty cycle in the cool-core cluster MS 0735.6+7421 with LOFAR data. *Astronomy and Astrophysics*, 650:A170, June 2021. doi: 10.1051/0004-6361/202040063. URL https://ui.adsabs.harvard.edu/abs/2021A&A...650A.170B. Provided by the SAO/NASA Astrophysics Data System.

A. Botteon. *Synchrotron emission and astrophysical applications*. PhD thesis, 2013. URL http://amslaurea.unibo.it/5626/.

M. Brienza, R. Morganti, J. Harwood, T. Duchet, K. Rajpurohit, A. Shulevski, M. J. Hardcastle, V. Mahatma, L. E. H. Godfrey, I. Prandoni, T. W. Shimwell, and H. Intema. Radio spectral properties and jet duty cycle in the restarted radio galaxy 3C388. *Astronomy and Astrophysics*, 638:A29, June 2020. doi: 10.1051/0004-6361/202037457. URL https://ui.adsabs.harvard.edu/abs/2020A&A...638A..29B. Provided by the SAO/NASA Astrophysics Data System.

M. Brienza, T. W. Shimwell, F. de Gasperin, I. Bikmaev, A. Bonafede, A. Botteon, M. Brüggen, G. Brunetti, R. Burenin, A. Capetti, E. Churazov, M. J. Hardcastle, I. Khabibullin, N. Lyskova, H. J. A. Röttgering, R. Sunyaev, R. J. van Weeren, F. Gastaldello, S. Mandal, S. J. D. Purser, A. Simionescu, and C. Tasse. A snapshot of the oldest active galactic nuclei feedback phases. *Nature Astronomy*, 5:1261–1267, Oct. 2021. doi: 10.1038/s41550-021-01491-0. URL https://ui.adsabs.harvard.edu/abs/2021NatAs...5.1261B. Provided by the SAO/NASA Astrophysics Data System.

M. Brienza, L. Lovisari, K. Rajpurohit, A. Bonafede, F. Gastaldello, M. Murgia, F. Vazza, E. Bonnassieux, A. Botteon, G. Brunetti, A. Drabent, M. J. Hardcastle, T. Pasini, C. J. Riseley, H. J. A. Röttgering, T. Shimwell, A. Simionescu, and R. J. van Weeren. The galaxy group NGC 507: Newly detected AGN remnant plasma transported by sloshing. *Astronomy and Astrophysics*, 661:A92, May 2022. doi: 10.1051/0004-6361/202142579. URL https://ui.adsabs.harvard.edu/abs/2022A&A...661A..92B. Provided by the SAO/NASA Astrophysics Data System.

J. O. Burns, G. Rhee, F. N. Owen, and J. Pinkney. Clumped X-Ray Emission around Radio Galaxies in Abell Clusters. *The Astrophysical Journal*, 423:94, Mar. 1994. doi: 10.1086/173792. URL https://ui.adsabs.harvard.edu/abs/1994ApJ...423...94B. Provided by the SAO/NASA Astrophysics Data System.

A. Chu, F. Durret, and I. Márquez. Physical properties of brightest cluster galaxies up to redshift 1.80 based on HST data. *Astronomy and Astrophysics*, 649:A42, May 2021. doi: 10.1051/0004-6361/202040245. URL https://ui.adsabs.harvard.edu/abs/2021A&A...649A..42C. Provided by the SAO/NASA Astrophysics Data System.

D. A. Clarke. A Restarting Jet Revisited: MHD Computations in 3-D. In D. A. Clarke and M. J. West, editors, *Computational Astrophysics; 12th Kingston Meeting on Theoretical Astrophysics*, volume 12 of *Astronomical Society of the Pacific Conference Series*, page 255, Jan. 1997. URL https://ui.adsabs.harvard.edu/abs/1997ASPC..123..255C. Provided by the SAO/NASA Astrophysics Data System.

D. A. Clarke and J. O. Burns. Numerical Simulations of a Restarting Jet. *The Astrophysical Journal*, 369:308, Mar. 1991. doi: 10.1086/169762. URL https://ui.adsabs.harvard.edu/abs/1991ApJ...369..308C. Provided by the SAO/NASA Astrophysics Data System.

G. Colla, C. Fanti, R. Fanti, I. Gioia, C. Lari, J. Lequeux, R. Lucas, and M. H. Ulrich. Radio and optical data on a complete sample of radio faint galaxies. *Astronomy and Astrophysics, Supplement*, 20:1–36, Apr. 1975. URL https://ui.adsabs.harvard.edu/abs/1975A&AS...20....1C. Provided by the SAO/NASA Astrophysics Data System.

J. Condon and S. Ransom. *Essential radio astronomy*. Princeton University Press, Princeton, 2016.

H. R. de Ruiter, P. Parma, G. M. Stirpe, I. Perez-Fournon, I. Gonzalez-Serrano, R. B. Rengelink, and M. N. Bremer. Bright galaxies from WENSS. I. The minisurvey. *Astronomy and Astrophysics*, 339:34–40, Nov. 1998. URL https://ui.adsabs.harvard.edu/abs/1998A&A...339...34D. Provided by the SAO/NASA Astrophysics Data System.

R. J. H. Dunn, S. W. Allen, G. B. Taylor, K. F. Shurkin, G. Gentile, A. C. Fabian, and C. S. Reynolds. The radio properties of a complete, X-ray selected sample of nearby, massive elliptical galaxies. *Monthly Notices of the RAS*, 404(1):180–197, May 2010. doi: 10.1111/j.1365-2966.2010.16314.x. URL https://ui.adsabs.harvard.edu/abs/2010MNRAS.404..180D. Provided by the SAO/NASA Astrophysics Data System.

D. Eckert, S. Ettori, E. Pointecouteau, R. F. J. van der Burg, and S. I. Loubser. The gravitational field of X-COP galaxy clusters. *Astronomy and Astrophysic*, 662:A123, June 2022. doi: 10.1051/0004-6361/202142507. URL https://ui.adsabs.harvard.edu/abs/2022A&A...662A.123E. Provided by the SAO/NASA Astrophysics Data System.

A. C. Fabian. Observational Evidence of Active Galactic Nuclei Feedback. *Annual Review of Astronomy and Astrophysics*, 50:455–489, Sept. 2012. doi: 10.1146/annurev-astro-081811-125521. URL https://ui.adsabs.harvard.edu/abs/2012ARA&A..50..455F. Provided by the SAO/NASA Astrophysics Data System.

B. L. Fanaroff and J. M. Riley. The morphology of extragalactic radio sources of high and low luminosity. *Monthly Notices of the RAS*, 167:31P–36P, May 1974. doi: 10.1093/mnras/167.1.31P. URL https://ui.adsabs.harvard.edu/abs/1974MNRAS.167P..31F. Provided by the SAO/NASA Astrophysics Data System.

L. Feretti, G. Giovannini, L. Gregorini, P. Parma, and G. Zamorani. Statistical properties of the radio cores in elliptical galaxies. *Astronomy and Astrophysics*, 139:55–63, Oct. 1984. URL https://ui.adsabs.harvard.edu/abs/1984A&A...139...55F. Provided by the SAO/NASA Astrophysics Data System.

D. Garofalo, D. A. Evans, and R. M. Sambruna. The evolution of radio-loud active galactic nuclei as a function of black hole spin. *Monthly Notices of the Royal Astronomical Society*, 406(2):975–986, 07 2010. ISSN 0035-8711. doi: 10.1111/j.1365-2966.2010.16797.x. URL https://doi.org/10.1111/j.1365-2966.2010.16797.x.

M. L. Gendron-Marsolais, C. L. H. Hull, R. Perley, L. Rudnick, R. Kraft, J. Hlavacek-Larrondo, A. C. Fabian, E. Roediger, R. J. van Weeren, A. Richard-Laferrière, E. Golden-Marx, N. Arakawa, and J. D. McBride. VLA Resolves Unexpected Radio Structures in the Perseus Cluster of Galaxies. *The Astrophysical Journal*, 911(1):56, Apr. 2021. doi: 10.3847/1538-4357/abddbb. URL https://ui.adsabs.harvard.edu/abs/2021ApJ...911...56G. Provided by the SAO/NASA Astrophysics Data System.

S. Giacintucci, T. Venturi, M. Murgia, D. Dallacasa, R. Athreya, S. Bardelli, P. Mazzotta, and D. J. Saikia. Radio morphology and spectral analysis of cD galaxies in rich and poor galaxy clusters. *Astronomy and Astrophysics*, 476(1):99–119, Dec. 2007. doi: 10.1051/0004-6361:20077918. URL https://ui.adsabs.harvard.edu/abs/2007A&A...476...99G. Provided by the SAO/NASA Astrophysics Data System.

F. Govoni and L. Feretti. Magnetic Fields in Clusters of Galaxies. *International Journal of Modern Physics D*, 13(8):1549–1594, Jan. 2004. doi: 10.1142/S0218271804005080. URL https://ui.adsabs.harvard.edu/abs/2004IJMPD..13.1549G. Provided by the SAO/NASA Astrophysics Data System.

Y. Gupta, B. Ajithkumar, H. S. Kale, S. Nayak, S. Sabhapathy, S. Sureshkumar, R. V. Swami, J. N. Chengalur, S. K. Ghosh, C. H. Ishwara-Chandra, B. C. Joshi, N. Kanekar, D. V. Lal, and S. Roy. The upgraded GMRT: opening new windows on the radio Universe. *Current Science*, 113(4):707–714, Aug. 2017. doi: 10.18520/cs/v113/i04/707-714. URL https://ui.adsabs.harvard.edu/abs/2017CSci..113..707G. Provided by the SAO/NASA Astrophysics Data System.

M. J. Hardcastle. Synchrotron and inverse-Compton emission from radio galaxies with non-uniform magnetic field and electron distributions. *Monthly Notices of the RAS*, 433(4):3364–3372, Aug. 2013. doi: 10.1093/mnras/stt1024. URL https://ui.adsabs.harvard.edu/abs/2013MNRAS.433.3364H. Provided by the SAO/NASA Astrophysics Data System.

M. J. Hardcastle, J. H. Croston, T. W. Shimwell, C. Tasse, G. Gürkan, R. Morganti, M. Murgia, H. J. A. Röttgering, R. J. van Weeren, and W. L. Williams. NGC 326: X-shaped no more. *Monthly Notices of the RAS*, 488(3):3416–3422, Sept. 2019. doi: 10.1093/mnras/stz1910. URL https://ui.adsabs.harvard.edu/abs/2019MNRAS.488.3416H. Provided by the SAO/NASA Astrophysics Data System.

J. J. Harwood, M. J. Hardcastle, J. H. Croston, and J. L. Goodger. BRATS: Broadband Radio Astronomy ToolS. Astrophysics Source Code Library, record ascl:1806.025, June 2018. URL https://ui.adsabs.harvard.edu/abs/2018ascl.soft06025H. Provided by the SAO/NASA Astrophysics Data System.

M. Huarte-Espinosa, M. Krause, and P. Alexander. 3D magnetohydrodynamic simulations of the evolution of magnetic fields in Fanaroff-Riley class II radio sources. *Monthly Notices of the RAS*, 417(1):382–399, Oct. 2011. doi: 10.1111/j.1365-2966.2011.19271.x. URL https://ui.adsabs.harvard.edu/abs/2011MNRAS.417..382H. Provided by the SAO/NASA Astrophysics Data System.

W. J. Jaffe and G. C. Perola. Dynamical Models of Tailed Radio Sources in Clusters of Galaxies. *Astronomy and Astrophysics*, 26:423, Aug. 1973. URL https://ui.adsabs.harvard.edu/abs/1973A&A....26..423J. Provided by the SAO/NASA Astrophysics Data System.

M. Jamrozy, U. Klein, K. H. Mack, L. Gregorini, and P. Parma. Spectral ageing in the relic radio galaxy B2 0924+30. *Astronomy and Astrophysics*, 427:79–86, Nov. 2004. doi: 10.1051/0004-6361:20048056. URL https://ui.adsabs.harvard.edu/abs/2004A&A...427...79J. Provided by the SAO/NASA Astrophysics Data System.

N. S. Kardashev. Nonstationarity of Spectra of Young Sources of Nonthermal Radio Emission. *Soviet Astronomy*, 6:317, Dec. 1962. URL https://ui.adsabs.harvard.edu/abs/1962SvA.....6..317K. Provided by the SAO/NASA Astrophysics Data System.

D. M. Katz-Stone, L. Rudnick, and M. C. Anderson. Determining the Shape of Spectra in Extended Radio Sources. *The Astrophysical Journal*, 407:549, Apr. 1993. doi: 10.1086/172536. URL https://ui.adsabs.harvard.edu/abs/1993ApJ...407..549K. Provided by the SAO/NASA Astrophysics Data System.

K. I. Kellermann, R. Sramek, M. Schmidt, D. B. Shaffer, and R. Green. VLA Observations of Objects in the Palomar Bright Quasar Survey. *Astronomical Journal*, 98:1195, Oct. 1989. doi: 10.1086/115207. URL https://ui.adsabs.harvard.edu/abs/1989AJ.....98.1195K. Provided by the SAO/NASA Astrophysics Data System.

C. Konar, D. J. Saikia, M. Jamrozy, and J. Machalski. Spectral ageing analysis of the double-double radio galaxy J1453+3308. *Monthly Notices of the Royal Astronomical Society*, 372(2):693–702, Oct. 2006. doi: 10.1111/j.1365-2966.2006.10874.x. URL https://ui.adsabs.harvard.edu/abs/2006MNRAS.372..693K. Provided by the SAO/NASA Astrophysics Data System.

J. P. Leahy, A. H. Bridle, and R. G. Strom. An Atlas of Extragalactic Radio Sources. In R. D. Ekers, C. Fanti, and L. Padrielli, editors, *Extragalactic Radio Sources*, volume 175, page 157, Jan. 1996. URL https://ui.adsabs.harvard.edu/abs/1996IAUS..175..157L. Provided by the SAO/NASA Astrophysics Data System.

M. J. Ledlow and F. N. Owen. 20 CM VLA Survey of Abell Clusters of Galaxies. VI. Radio/Optical Luminosity Functions. *The Astrophysical Journals*, 112:9, July 1996. doi: 10.1086/117985. URL https://ui.adsabs.harvard.edu/abs/1996AJ....112....9L. Provided by the SAO/NASA Astrophysics Data System.

Y.-T. Lin and J. J. Mohr. K-band Properties of Galaxy Clusters and Groups: Brightest Cluster Galaxies and Intracluster Light. *The Astrophysical Journal*, 617(2):879–895, Dec. 2004. doi: 10.1086/425412. URL https://ui.adsabs.harvard.edu/abs/2004ApJ...617..879L. Provided by the SAO/NASA Astrophysics Data System.

E. Liuzzo, G. Giovannini, M. Giroletti, and G. B. Taylor. Parsec-scale properties of brightest cluster galaxies. *Astronomy and Astrophysics*, 516:A1, June 2010. doi: 10.1051/0004-6361/200913888. URL https://ui.adsabs.harvard.edu/abs/2010A&A...516A...1L. Provided by the SAO/NASA Astrophysics Data System.

E. Lopez-Rodriguez, M. Kishimoto, R. Antonucci, M. C. Begelman, N. Globus, and R. Blandford. On the origin of radio-loudness in active galactic nuclei using far-infrared polarimetric observations. *arXiv e-prints*, art. arXiv:2207.09466, July 2022. URL https://ui.adsabs.harvard.edu/abs/2022arXiv220709466L. Provided by the SAO/NASA Astrophysics Data System.

J. P. McMullin, B. Waters, D. Schiebel, W. Young, and K. Golap. CASA Architecture and Applications. In R. A. Shaw, F. Hill, and D. J. Bell, editors, *Astronomical Data Analysis Software and Systems XVI*, volume 376 of *Astronomical Society of the Pacific Conference Series*, page 127, Oct. 2007. URL https://ui.adsabs.harvard.edu/abs/2007ASPC..376..127M. Provided by the SAO/NASA Astrophysics Data System.

B. R. McNamara and P. E. J. Nulsen. Heating Hot Atmospheres with Active Galactic Nuclei. *Annual Review of Astronomy and Astrophysics*, 45(1):117–175, Sept. 2007. doi: 10.1146/annurev.astro.45.051806.110625. URL https://ui.adsabs.harvard.edu/abs/2007ARA&A..45..117M. Provided by the SAO/NASA Astrophysics Data System.

B. R. McNamara and P. E. J. Nulsen. Mechanical feedback from active galactic nuclei in galaxies, groups and clusters. *New Journal of Physics*, 14(5):055023, May 2012. doi: 10.1088/1367-2630/14/5/055023. URL https://ui.adsabs.harvard.edu/abs/2012NJPh...14e5023M. Provided by the SAO/NASA Astrophysics Data System.

D. L. Meier. The Association of Jet Production with Geometrically Thick Accretion Flows and Black Hole Rotation. *The Astrophysical Journall*, 548(1):L9–L12, Feb. 2001. doi: 10.1086/318921. URL https://ui.adsabs.harvard.edu/abs/2001ApJ..548L...9M. Provided by the SAO/NASA Astrophysics Data System.

P. J. Mendygral, T. W. Jones, and K. Dolag. MHD Simulations of Active Galactic Nucleus Jets in a Dynamic Galaxy Cluster Medium. *The Astrophysical Journal*, 750(2):166, May 2012. doi: 10.1088/0004-637X/750/2/166. URL https://ui.adsabs.harvard.edu/abs/2012ApJ...750..166M. Provided by the SAO/NASA Astrophysics Data System.

F. Mernier, N. Werner, J. Bagchi, M. L. Gendron-Marsolais, Gopal-Krishna, M. Guainazzi, A. Richard-Laferrière, T. W. Shimwell, and A. Simionescu. Discovery of inverse-Compton X-ray emission and robust estimation of magnetic field in a galaxy group. *arXiv e-prints*, art. arXiv:2207.10092, July 2022. URL https://ui.adsabs.harvard.edu/abs/2022arXiv220710092M. Provided by the SAO/NASA Astrophysics Data System.

B. Mingo, J. H. Croston, M. J. Hardcastle, P. N. Best, K. J. Duncan, R. Morganti, H. J. A. Rottgering, J. Sabater, T. W. Shimwell, W. L. Williams, M. Brienza, G. Gurkan, V. H. Mahatma, L. K. Morabito, I. Prandoni, M. Bondi, J. Ineson, and S. Mooney. Revisiting the Fanaroff-Riley dichotomy and radio-galaxy morphology with the LOFAR Two-Metre Sky Survey (LoTSS). *Monthly Notices of the Royal Astronomical Society*, 488(2):2701–2721, Sept. 2019. doi: 10.1093/mnras/stz1901. URL https://ui.adsabs.harvard.edu/abs/2019MNRAS.488.2701M. Provided by the SAO/NASA Astrophysics Data System.

M. Murgia, P. Parma, K. H. Mack, H. R. de Ruiter, R. Fanti, F. Govoni, A. Tarchi, S. Giacintucci, and M. Markevitch. Dying radio galaxies in clusters. *Astronomy and Astrophysics*, 526:A148, Feb. 2011. doi: 10.1051/0004-6361/201015302. URL https://ui.adsabs.harvard.edu/abs/2011A&A...526A.148M. Provided by the SAO/NASA Astrophysics Data System.

M. Murgia, M. Markevitch, F. Govoni, P. Parma, R. Fanti, H. R. de Ruiter, and K. H. Mack. Chandra observations of dying radio sources in galaxy clusters. *Astronomy and Astrophysics*, 548:A75, Dec. 2012. doi: 10.1051/0004-6361/201219702. URL https://ui.adsabs.harvard.edu/abs/2012A&A...548A..75M. Provided by the SAO/NASA Astrophysics Data System.

B. D. Oppenheimer, A. Babul, Y. Bahé, I. S. Butsky, and I. G. McCarthy. Simulating Groups and the IntraGroup Medium: The Surprisingly Complex and Rich Middle Ground between Clusters and Galaxies. *Universe*, 7(7):209, June 2021. doi: 10.3390/universe7070209. URL https://ui.adsabs.harvard.edu/abs/2021Univ...7..209O. Provided by the SAO/NASA Astrophysics Data System.

F. N. Owen and M. J. Ledlow. A 20 Centimeter VLA Survey of Abell Clusters of Galaxies. VII. Detailed Radio Images. *The Astrophysical Journals*, 108(1):41–98, Jan. 1997. doi: 10.1086/312954. URL https://ui.adsabs.harvard.edu/abs/1997ApJS..108...41O. Provided by the SAO/NASA Astrophysics Data System.

P. Padovani. The faint radio sky: radio astronomy becomes mainstream. *Astronomy and Astrophysicsr*, 24(1):13, Sept. 2016. doi: 10.1007/s00159-016-0098-6. URL https://ui.adsabs.harvard.edu/abs/2016A&ARv..24...13P. Provided by the SAO/NASA Astrophysics Data System.

P. Parma, H. R. de Ruiter, C. Fanti, and R. Fanti. VLA observations of low luminosity radio galaxies. I. Sources with angular size smaller than two arcminutes. *Astronomy and Astrophysics*, 64:135–171, Apr. 1986. URL https://ui.adsabs.harvard.edu/abs/1986A&AS...64..135P. Provided by the SAO/NASA Astrophysics Data System.

R. A. Perley and B. J. Butler. An Accurate Flux Density Scale from 50 MHz to 50 GHz. *The Astrophysical Journals*, 230(1):7, May 2017. doi: 10.3847/1538-4365/aa6df9. URL https://ui.adsabs.harvard.edu/abs/2017ApJS..230....7P. Provided by the SAO/NASA Astrophysics Data System.

C. S. Reynolds and M. C. Begelman. Intermittant Radio Galaxies and Source Statistics. *The Astrophysical Journall*, 487(2):L135–L138, Oct. 1997. doi: 10.1086/310894. URL https://ui.adsabs.harvard.edu/abs/1997ApJ...487L.135R. Provided by the SAO/NASA Astrophysics Data System.

P. Romano, C. Guidorzi, A. Segreto, L. Ducci, and S. Vercellone. Constraining duty cycles through a Bayesian technique. *Astronomy and Astrophysics*, 572:A97, Dec. 2014. doi: 10.1051/0004-6361/201424180. URL https://ui.adsabs.harvard.edu/abs/2014A&A...572A..97R. Provided by the SAO/NASA Astrophysics Data System.

L. Rudnick, M. Brüggen, G. Brunetti, W. D. Cotton, W. Forman, T. W. Jones, C. Nolting, G. Schellenberger, and R. van Weeren. Intracluster Magnetic Filaments and an Encounter with a Radio Jet. *The Astrophysical Journal*, 935(2):168, Aug. 2022. doi: 10.3847/1538-4357/ac7c76. URL https://ui.adsabs.harvard.edu/abs/2022ApJ...935..168R. Provided by the SAO/NASA Astrophysics Data System.

J. Sabater, P. N. Best, M. J. Hardcastle, T. W. Shimwell, C. Tasse, W. L. Williams, M. Brüggen, R. K. Cochrane, J. H. Croston, F. de Gasperin, K. J. Duncan, G. Gürkan, A. P. Mechev, L. K. Morabito, I. Prandoni, H. J. A. Röttgering, D. J. B. Smith, J. J. Harwood, B. Mingo, S. Mooney, and A. Saxena. The LoTSS view of radio AGN in the local Universe. The most massive galaxies are always switched on. *Astronomy and Astrophysics*, 622:A17, Feb. 2019. doi: 10.1051/0004-6361/201833883. URL https://ui.adsabs.harvard.edu/abs/2019A&A...622A..17S. Provided by the SAO/NASA Astrophysics Data System.

A. P. Schoenmakers, A. G. de Bruyn, H. J. A. Röttgering, H. van der Laan, and C. R. Kaiser. Radio galaxies with a 'double-double morphology'- I. Analysis of the radio properties and evidence for interrupted activity in active galactic nuclei. *Monthly Notices of the Royal Astronomical Society*, 315(2):371–380, 06 2000. ISSN 0035-8711. doi: 10.1046/j.1365-8711.2000.03430.x. URL https://doi.org/10.1046/j.1365-8711.2000.03430.x.

S. S. Shabala, S. Ash, P. Alexander, and J. M. Riley. The duty cycle of local radio galaxies. *Monthly Notices of the Royal Astronomical Society*, 388(2):625–637, 07 2008. ISSN 0035-8711. doi: 10.1111/j.1365-2966.2008.13459.x. URL https://doi.org/10.1111/j.1365-2966.2008.13459.x.

A. Shulevski, R. Morganti, J. J. Harwood, P. D. Barthel, M. Jamrozy, M. Brienza, G. Brunetti, H. J. A. Röttgering, M. Murgia, G. J. White, J. H. Croston, and M. Brüggen. Radiative age mapping of the remnant radio galaxy B2 0924+30: the LOFAR perspective. *Astronomy and Astrophysics*, 600:A65, Apr. 2017. doi: 10.1051/0004-6361/201630008. URL https://ui.adsabs.harvard.edu/abs/2017A&A...600A..65S. Provided by the SAO/NASA Astrophysics Data System.

V. Springel, S. D. M. White, A. Jenkins, C. S. Frenk, N. Yoshida, L. Gao, J. Navarro, R. Thacker, D. Croton, J. Helly, J. A. Peacock, S. Cole, P. Thomas, H. Couchman, A. Evrard, J. Colberg, and F. Pearce. Simulations of the formation, evolution and clustering of galaxies and quasars. *Nature*, 435(7042):629–636, June 2005. doi: 10.

1038/nature03597. URL https://ui.adsabs.harvard.edu/abs/2005Natur.435..629S. Provided by the SAO/NASA Astrophysics Data System.

M. P. van Haarlem, M. W. Wise, A. W. Gunst, G. Heald, J. P. McKean, J. W. T. Hessels, A. G. de Bruyn, R. Nijboer, J. Swinbank, R. Fallows, M. Brentjens, A. Nelles, R. Beck, H. Falcke, R. Fender, J. Hörandel, L. V. E. Koopmans, G. Mann, G. Miley, H. Röttgering, B. W. Stappers, R. A. M. J. Wijers, S. Zaroubi, M. van den Akker, A. Alexov, J. Anderson, K. Anderson, A. van Ardenne, M. Arts, A. Asgekar, I. M. Avruch, F. Batejat, L. Bähren, M. E. Bell, M. R. Bell, I. van Bemmel, P. Bennema, M. J. Bentum, G. Bernardi, P. Best, L. Bîrzan, A. Bonafede, A. J. Boonstra, R. Braun, J. Bregman, F. Breitling, R. H. van de Brink, J. Broderick, P. C. Broekema, W. N. Brouw, M. Brüggen, H. R. Butcher, W. van Cappellen, B. Ciardi, T. Coenen, J. Conway, A. Coolen, A. Corstanje, S. Damstra, O. Davies, A. T. Deller, R. J. Dettmar, G. van Diepen, K. Dijkstra, P. Donker, A. Doorduin, J. Dromer, M. Drost, A. van Duin, J. Eislöffel, J. van Enst, C. Ferrari, W. Frieswijk, H. Gankema, M. A. Garrett, F. de Gasperin, M. Gerbers, E. de Geus, J. M. Grießmeier, T. Grit, P. Gruppen, J. P. Hamaker, T. Hassall, M. Hoeft, H. A. Holties, A. Horneffer, A. van der Horst, A. van Houwelingen, A. Huijgen, M. Iacobelli, H. Intema, N. Jackson, V. Jelic, A. de Jong, E. Juette, D. Kant, A. Karastergiou, A. Koers, H. Kollen, V. I. Kondratiev, E. Kooistra, Y. Koopman, A. Koster, M. Kuniyoshi, M. Kramer, G. Kuper, P. Lambropoulos, C. Law, J. van Leeuwen, J. Lemaitre, M. Loose, P. Maat, G. Macario, S. Markoff, J. Masters, R. A. McFadden, D. McKay-Bukowski, H. Meijering, H. Meulman, M. Mevius, E. Middelberg, R. Millenaar, J. C. A. Miller-Jones, R. N. Mohan, J. D. Mol, J. Morawietz, R. Morganti, D. D. Mulcahy, E. Mulder, H. Munk, L. Nieuwenhuis, R. van Nieuwpoort, J. E. Noordam, M. Norden, A. Noutsos, A. R. Offringa, H. Olofsson, A. Omar, E. Orrú, R. Overeem, H. Paas, M. Pandey-Pommier, V. N. Pandey, R. Pizzo, A. Polatidis, D. Rafferty, S. Rawlings, W. Reich, J. P. de Reijer, J. Reitsma, G. A. Renting, P. Riemers, E. Rol, J. W. Romein, J. Roosjen, M. Ruiter, A. Scaife, K. van der Schaaf, B. Scheers, P. Schellart, A. Schoenmakers, G. Schoonderbeek, M. Serylak, A. Shulevski, J. Sluman, O. Smirnov, C. Sobey, H. Spreeuw, M. Steinmetz, C. G. M. Sterks, H. J. Stiepel, K. Stuurwold, M. Tagger, Y. Tang, C. Tasse, I. Thomas, S. Thoudam, M. C. Toribio, B. van der Tol, O. Usov, M. van Veelen, A. J. van der Veen, S. ter Veen, J. P. W. Verbiest, R. Vermeulen, N. Vermaas, C. Vocks, C. Vogt, M. de Vos, E. van der Wal, R. van Weeren, H. Weggemans, P. Weltevrede, S. White, S. J. Wijnholds, T. Wilhelmsson, O. Wucknitz, S. Yatawatta, P. Zarka, A. Zensus, and J. van Zwieten. LOFAR: The LOw-Frequency ARray. *Astronomy and Astrophysics*, 556:A2, Aug. 2013. doi: 10.1051/0004-6361/201220873. URL https://ui.adsabs.harvard.edu/abs/2013A&A...556A...2V. Provided by the SAO/NASA Astrophysics Data System.

R. J. van Weeren, F. de Gasperin, H. Akamatsu, M. Brüggen, L. Feretti, H. Kang, A. Stroe, and F. Zandanel. Diffuse Radio Emission from Galaxy Clusters. *Space Science Reviews*, 215(1):16, Feb. 2019. doi: 10.1007/s11214-019-0584-z. URL https://ui.adsabs.harvard.edu/abs/2019SSRv..215...16V. Provided by the SAO/NASA Astrophysics Data System.

K. L. Visnovsky, C. D. Impey, C. B. Foltz, P. C. Hewett, R. J. Weymann, and S. L.

Morris. Radio Properties of Optically Selected Quasars. *Astrophysical Journal*, 391: 560, June 1992. doi: 10.1086/171370. URL https://ui.adsabs.harvard.edu/abs/1992ApJ...391..560V. Provided by the SAO/NASA Astrophysics Data System.

S. Walg, A. Achterberg, S. Markoff, R. Keppens, and O. Porth. Relativistic AGN jets - II. Jet properties and mixing effects for episodic jet activity. *Monthly Notices of the RAS*, 439(4):3969–3985, Apr. 2014. doi: 10.1093/mnras/stu253. URL https://ui.adsabs.harvard.edu/abs/2014MNRAS.439.3969W. Provided by the SAO/NASA Astrophysics Data System.

S. D. M. White and M. J. Rees. Core condensation in heavy halos: a two-stage theory for galaxy formation and clustering. *Monthly Notices of the RAS*, 183:341–358, May 1978. doi: 10.1093/mnras/183.3.341. URL https://ui.adsabs.harvard.edu/abs/1978MNRAS.183..341W. Provided by the SAO/NASA Astrophysics Data System.